

NASA Technical Paper 1215

Effects of Spanwise Nozzle Geometry
and Location on the Longitudinal
Aerodynamic Characteristics
of a Vectored-Engine-Over-Wing
Configuration at Subsonic Speeds

Laurence D. Leavitt and Long P. Yip

CASE FILE
COPY

MAY 1978

NASA

NASA Technical Paper 1215

Effects of Spanwise Nozzle Geometry
and Location on the Longitudinal
Aerodynamic Characteristics
of a Vectored-Engine-Over-Wing
Configuration at Subsonic Speeds

Laurence D. Leavitt and Long P. Yip
Langley Research Center
Hampton, Virginia



National Aeronautics
and Space Administration

**Scientific and Technical
Information Office**

1978

SUMMARY

An investigation has been conducted in the Langley V/STOL tunnel to determine the effects of spanwise blowing on the longitudinal aerodynamic characteristics of a model using a vectored-engine-over-wing powered lift concept. The effects of spanwise nozzle throat area, internal and external nozzle geometry, and vertical and axial location were investigated. These effects were studied at a Mach number of 0.186 over an angle-of-attack range from 14° to 40° . A high-pressure air system was used to provide jet-exhaust simulation. Engine nozzle pressure ratio was varied from 1.0 (jet off) to approximately 3.75.

The results of the investigation indicate that spanwise blowing can provide significant improvements in aerodynamic performance at high angles of attack. These improvements are in addition to the lift increments provided by the vectored-engine-over-wing concept. Spanwise-blowing nozzle throat area, nozzle pressure ratio, and external shape were the primary factors affecting aerodynamic performance. Generally, increases in exit area and nozzle pressure ratio provided significant increases in lift and also improvements in polar shape.

A rectangular flush spanwise nozzle produced the highest performance at lower angles of attack, while a round nozzle protruding into the external flow field provided significant improvements at higher angles of attack. Spanwise nozzle location and internal geometry of the circular spanwise nozzles had little effect on aerodynamic performance of the concept investigated.

INTRODUCTION

Much attention has been given in recent years to the augmentation of lift capabilities of modern fighter-type aircraft for increased performance and maneuverability. Canards, strakes, maneuvering flaps (see refs. 1 to 7), and several powered lift concepts such as internally blown flaps (ref. 8), externally blown flaps (refs. 9 and 10), upper-surface blowing (refs. 11 and 12), vectored thrust (refs. 13 to 16), vectored-engine-over-wing (refs. 17 to 19), and spanwise blowing (refs. 20 to 24) are all methods being studied as ways to obtain additional usable lift for improvement of maneuverability as well as take-off and landing performance.

The present investigation was undertaken to assess the longitudinal aerodynamic characteristics of a configuration which utilizes a close-coupled canard-wing combination, a vectored-engine-over-wing powered lift concept (VEO-wing), and a spanwise blowing concept. The VEO-wing concept utilizes the engine momentum from over-wing-mounted engines to improve the external aerodynamics by blowing over a variable trailing-edge flap. In addition to the lift and drag polar improvements associated with vectoring the engine jet exhaust, spanwise blowing can provide further benefits, especially at high angles of attack (refs. 17 to 19). Spanwise blowing has been shown to help form and stabilize the leading-

edge vortex on low to moderately swept wings at high angles of attack where vortex breakdown usually occurs (refs. 20 to 24). This concept increases the lift-curve slope and extends the stall angle of attack by reducing or eliminating outboard wing panel separation.

The VEO-wing concept (along with the associated spanwise blowing) has been shown as a possible near term concept in that no new engine development is required (refs. 17 and 18). Total engine exhaust is used for thrust vectoring. Engine nozzle exhaust flow (not compressor bleed) is also used for leading-edge vortex augmentation by directing a portion of the engine exhaust flow spanwise over the wing surface. This use of total nozzle exhaust is advantageous in that there are no bleed requirements on the engine. Large losses in gross thrust result from bleeding the compressors of high-performance engines. In addition, many of the other powered lift concepts previously mentioned require extensive ducting in the fuselage and/or wings. This ducting may be counterproductive to good fighter design as ducting increases weight and may increase wing thickness.

Because a great deal of interest has been recently placed on the benefits of spanwise blowing, an investigation was conducted in the Langley V/STOL tunnel at $M = 0.186$ to evaluate the effects of various spanwise-blowing nozzle geometry and location changes on the subsonic aerodynamic characteristics of a VEO-wing model. Spanwise nozzle parameters include nozzle throat area, internal and external shape, and vertical and axial location. Some effects of wing leading-edge flap deflections and canard incidence changes in the presence of spanwise blowing were also investigated. These tests were conducted at an angle-of-attack range from 14° to 40° . A high-pressure air system was used to simulate jet-exhaust flow and to provide engine nozzle pressure ratios from 1.0 (jet off) to approximately 3.75.

SYMBOLS

All aerodynamic coefficients are referenced to the stability axis system and are nondimensionalized with respect to $q_\infty S$ or $q_\infty S \bar{c}$ except at static conditions ($M = 0$) where p_a was substituted for q_∞ . Coefficients denoted as total coefficients include thrust effects. The moment reference center was located at a point 110.025 cm rearward of the fuselage nose and in the chord plane of the wing located at -3.53 cm below the model center line. (See fig. 1(a).) All dimensions presented are in the International System of Units (SI).

C_A total static axial-force coefficient (eq. (1) and fig. 3)

$C_{(D-T)}$ total drag-minus-thrust coefficient, $\frac{D - T}{q_\infty S}$

C_L total lift coefficient (including thrust component)

$C_{L,b}$ total lift coefficient of baseline nozzle configuration (Conf 1)

$C_{L,C_T=0}$ jet-off total lift coefficient

$C_{L,j}$	jet-reaction lift coefficient
$C_{L, sb}$	total lift coefficient of spanwise-blowing configuration
$C_{L, \Gamma}$	jet-induced supercirculation lift coefficient
ΔC_L	incremental lift coefficient, $C_{L, \Gamma} + C_{L, j}$
$\Delta C_{L, a}$	incremental lift coefficient due to spanwise-blowing area, $C_{L, sb} - C_{L, b}$
C_M	total static pitching-moment coefficient (eq. (4) and fig. 3)
C_m	total pitching-moment coefficient
C_N	total static normal-force coefficient (eq. (2) and fig. 3)
C_{SF}	resultant static side-force coefficient, $C_{Y, LH} - C_{Y, RH}$ (eq. (3) and fig. 3)
C_T	thrust coefficient, $\frac{T}{q_\infty S}$
$C_{T, s}$	static ($M = 0$) thrust coefficient, $\frac{T}{p_a S}$
C_y	static side-force coefficient (eq. (3) and fig. 3)
\bar{c}	wing mean geometric chord, 31.25 cm
c_r	reference wing chord, 44.82 cm, located at wing-fuselage intersection, BL 7.938 cm
D	drag force, N
h_n	height of center line of spanwise nozzle exit plane above the model reference center, cm (figs. 1(f) to 1(i))
M	Mach number
p_a	ambient pressure, Pa
$p_{t, j}$	nozzle total pressure, Pa
p_∞	free-stream static pressure, Pa
q_∞	free-stream dynamic pressure, Pa
S	wing reference area including projection of leading- and trailing- edge sweep to model center line, 3251.63 cm ² (fig. 1(a))

T	thrust force, N
x_n	axial location of center line of spanwise nozzle exit plane rearward of the wing-fuselage intersection, FS 108.21 cm
z	moment transfer distance from center line of model to model reference center, -3.53 cm
α	angle of attack, deg
δ_c	canard incidence angle, positive leading edge up, deg
δ_{LE}	wing leading-edge flap deflection angle, positive leading edge down, deg
δ_s	static ($M = 0$) jet turning angle (eq. (6)), deg
δ_{TE}	wing trailing-edge flap deflection angle, positive trailing edge down, deg

Subscripts:

I	inboard flap (fig. 1(b))
LH	left hand
O	outboard flap (fig. 1(b))
RH	right hand

Abbreviations:

BL	buttockline, cm
C-D	converging-diverging
Conf	configuration
Conv	convergent
FS	fuselage station, cm
MRC	model reference center, WL -3.53 cm
WL	waterline

MODEL AND APPARATUS

Sketches showing the VEO-wing model are presented in figure 1, and photographs of the model installed in the Langley V/STOL tunnel are shown in figure 2. The model consists of a canard-wing-body-nozzle configuration which is

representative of a high-performance fighter-type aircraft. Some compromises were made in the external lines of the model. The inlets were faired over since inlet flow could not be accommodated, and space to house the propulsion simulator hardware and sting support system was required.

The wing shown in figure 1(b) had a leading-edge sweep of 40° and a cranked trailing edge. It incorporated a full-span leading-edge flap and inboard and outboard trailing-edge flaps. The inboard trailing-edge flap was located directly behind the engine exhaust nozzle and was used for thrust vectoring. Both the inboard and outboard flaps were deflected together except where noted by the subscripts I and O (inboard and outboard).

The VEO-wing configuration was tested with two canard planforms (fig. 1(c)). Both canards had essentially the same exposed area; however, the leading-edge sweep of the H_3 canard was larger.

Propulsion System

A sketch of the key features of model propulsion system is shown in figure 1(d). These features are similar to those shown in references 17 to 19. An external high-pressure air system provided air for exhaust flow simulation at a controlled temperature of about 388 K. This high-pressure air is brought through the sting support strut into a high-pressure plenum and airline arrangement. The airline was designed to minimize tare forces on the balance caused by the transfer of high-pressure air across the balance to the model plenum. This airline was connected to a high-pressure plenum which split the flow and directed it into two U-shaped air supply pipes. (See fig. 1(d).) Two valves located on the supply pipes allowed the flow rate to be controlled to each nozzle for balancing purposes.

The nonaxisymmetric nozzle shown in figure 1(e) represents half-wedge two-dimensional (2-D) convergent-divergent (C-D) nozzles with an aspect ratio of 4.0, the aspect ratio being defined as the throat width divided by the throat height. The nozzle half-wedges were interchangeable to allow total nozzle throat area (engine-exhaust nozzle throat area plus spanwise-blowing nozzle throat area) to remain nearly constant throughout the test.

Several spanwise nozzle designs were investigated in combination with the engine-exhaust nozzle shown in figure 1(e). All nozzle variables were compared at constant nozzle pressure ratio. The spanwise nozzles were swept 40° to allow the spanwise flow to be essentially parallel to the wing leading edge. The nozzle configuration variations are shown in figures 1(f) to 1(i) and are listed in table I. It should be noted that the spanwise nozzle throat area given in the figures and in table I is the throat area for each side (total spanwise nozzle throat area would be double the value given). Also, it should be noted that the round spanwise nozzle shown in figure 1(g) had a smaller external diameter than the spanwise nozzle shown in figure 1(f).

Wind Tunnel and Support System

This investigation was conducted in the Langley V/STOL wind tunnel, which is a single-return atmospheric wind tunnel with a 4.4-m by 6.6-m rectangular test section. The wind tunnel has a continuously variable airspeed capability up to $M = 0.30$.

The model was supported by a sting as shown in figures 1(d) and 2(a). The tunnel sting support pivots and translates in such a manner that the model remains on or near the test section center line throughout the angle-of-attack range. The test data were not corrected for blockage or flow angularity since these were considered negligible.

Instrumentation

External aerodynamic forces and moments and nozzle thrust forces and moments were measured with a six-component strain-gage balance. Four internal base cavity pressure orifices were located approximately 90° apart in the cylindrical base region at about model fuselage station 175.26 cm. These measurements were used to calculate and remove base pressure tares (referenced to free-stream static pressure) from the balance readings. In addition, one total-pressure probe in each engine exhaust nozzle was connected through a remotely controlled solenoid valve to a lower pressure range, more accurate pressure transducer and was used for measurement of nozzle base cavity pressure during jet-off operating conditions. Nozzle cavity base tares, referenced to free-stream static pressure, were calculated from these measurements and removed from the jet-off balance data.

A venturi flowmeter (external to the test section) was used to measure the total mass-flow rate to the nozzles. Three total-pressure probes, illustrated in figure 1(e), and one thermocouple, measuring static temperature at the wall, were located forward of each engine nozzle throat and were used to measure nozzle internal flow characteristics.

Model angle of attack was measured with an accelerometer located in the nose cavity of the model fuselage. This attitude transmitter recorded changes in model attitude with respect to the horizontal and accounted for any deflection of the sting and balance under aerodynamic loads.

Tests

The wind-tunnel tests were conducted at $M = 0.186$ in the Langley V/STOL tunnel. The free-stream dynamic pressure was 2394 Pa, and the stagnation temperature was approximately 358 K. The average Reynolds number was 1.26×10^6 based on \bar{c} . All configurations were tested with fixed boundary-layer transition strips on the model wings, canards, and nose. These transition strips consisted of No. 80 silicon carbide grit located 2.54 cm aft of wing and canard leading edges and 4.06 cm aft of nose. These transition strips were used to insure a turbulent boundary layer over the nozzles and aft portion of the wing.

Force and moment data were obtained for each configuration at angles of attack from 14° to 40° and a nozzle pressure ratio range from 1.0 to 3.75.

Data Reduction

Data for both the model conditions and the wind-tunnel test conditions were recorded simultaneously on magnetic tape. At each test point multiple data samples were recorded. The samples were averaged, and the averaged values were used for all computations.

Total aerodynamic and nozzle thrust forces and moments were measured by an internal six-component strain-gage balance as shown in figure 1(d). Balance data were corrected for presence of the airline (and the air pressure associated with the airline) across the balance. To obtain corrected thrust-minus-axial force, it was necessary to make momentum tare corrections for forces induced on the model by the nozzle exhaust flow simulation system. The momentum tares are usually associated with transfer of the high-pressure air, required for propulsion simulation, across the balance. Momentum tares were calculated using standard calibration nozzles and the technique described in reference 13.

Static calibrations.— Prior to entry into the wind tunnel, the performance of each nozzle configuration was obtained in a static ($M = 0$) test stand. The variable trailing-edge flap was removed for static calibrations. The high-pressure air system and the hardware associated with it were essentially identical to the system used in the wind tunnel.

During the static calibration test axial-force, normal-force, side-force, and pitching-moment data were obtained for the right-hand nozzle and the left-hand nozzle separately. The total nozzle force and moment coefficients were obtained from the following equations:

$$C_A = C_{A,LH} + C_{A,RH} \quad (1)$$

$$C_N = C_{N,LH} + C_{N,RH} \quad (2)$$

$$C_{SF} = C_{Y,LH} - C_{Y,RH} \quad (3)$$

$$C_M = C_{M,LH} + C_{M,RH} \quad (4)$$

With the main exhaust nozzles blowing and with no spanwise blowing, equations (1), (2), and (4) provide the calibration forces and moments due to thrust. When there is blowing from both the main exhaust and spanwise nozzles, the effects of spanwise blowing have to be accounted for in the calibration in order to obtain the total thrust level of the propulsion system. The effects of the spanwise blowing on the side-force contribution to thrust are found by taking the difference between the left-hand and right-hand spanwise nozzle data in equation (3).

The static thrust coefficient and the static thrust turning angle (thrust vector angle) are then defined as

$$C_{T,s} = \sqrt{C_N^2 + C_A^2 + C_{SF}^2} \quad (5)$$

$$\delta_s = \tan^{-1} \frac{C_N}{C_A} \quad (6)$$

A sample of this type of analysis, which was performed for each configuration, is shown in figure 3 for the 6.49 cm² round, convergent spanwise-blowing nozzle (Conf 10). Data were reduced in a similar manner in reference 19. In this figure the data acquired with both right-hand and left-hand nozzles operating simultaneously are shown for comparison purposes. Static performance characteristics, as defined by equations (5) and (6), are presented in figures 4(a) and 4(b).

The static thrust coefficient $C_{T,s}$ was related to wind-on conditions by

$$C_T = C_{T,s} \left(\frac{P_\infty}{q_\infty} \right)$$

This calculation was required to reflect the difference in local ambient pressure between static ($M = 0$) and wind-on conditions. These data are presented in figure 4(c).

Incremental lift.— As shown in reference 8 the total lift measured by the force balance can be divided into three components: (1) jet-off lift, (2) jet-induced supercirculation lift, and (3) jet-reaction lift. In coefficient form this relation can be stated as

$$C_L = C_{L,C_T=0} + C_{L,\Gamma} + C_{L,j} \quad (7)$$

where $C_{L,C_T=0}$ is the jet-off lift coefficient, $C_{L,\Gamma}$ is the jet-induced supercirculation term, and $C_{L,j}$ is the jet-reaction lift coefficient. The incremental lift coefficient ΔC_L is determined by subtracting the measured jet-off lift coefficient from the measured total lift coefficient,

$$\Delta C_L = C_L - C_{L,C_T=0} \quad (8)$$

RESULTS

The results of this investigation are presented in plotted coefficient form. The configurations tested and their respective figure numbers are listed in table II. These figures, 5 to 18, present basic longitudinal characteristics of the VEO-wing model as a function of nozzle pressure ratio.

Comparison and summary plots are presented as follows:

	Figure
Sample breakdown of effects of trailing-edge flap deflection, nozzle thrust, thrust vectoring, and spanwise blowing on lift coefficient for $\delta_{LE} = \delta_C = 0^\circ$, H ₂ canard	19
Effect of spanwise nozzle area on longitudinal aerodynamic characteristics for $p_{t,j}/p_\infty = 3.25$, $\delta_{TE} = 15^\circ$, $\delta_{LE} = \delta_C = 0^\circ$, H ₂ canard:	
$h_n/c_r = 0.0793$	20 (a)
$h_n/c_r = 0.0935$	20 (b)
Lift increment due to spanwise blowing as a function of spanwise-blowing nozzle throat area for $p_{t,j}/p_\infty = 3.25$, $\delta_{TE} = 15^\circ$, $\delta_{LE} = \delta_C = 0^\circ$, H ₂ canard	21
Effect of spanwise nozzle external shape on longitudinal aerodynamic characteristics for $p_{t,j}/p_\infty = 3.25$, $\delta_{LE} = \delta_C = 0^\circ$, H ₂ canard:	
$\delta_{TE} = 15^\circ$	22 (a)
$\delta_{TE} = 0^\circ$	22 (b)
Effect of spanwise nozzle internal shape on longitudinal aerodynamic characteristics for $p_{t,j}/p_\infty = 3.25$, $\delta_{TE} = 15^\circ$, $\delta_{LE} = \delta_C = 0^\circ$, H ₂ canard	23
Effect of spanwise nozzle axial location on longitudinal aerodynamic characteristics for $p_{t,j}/p_\infty = 3.25$, $\delta_{TE} = 15^\circ$, $\delta_{LE} = \delta_C = 0^\circ$, H ₂ canard:	
3.25 cm ² round, convergent	24 (a)
3.22 cm ² round, C-D	24 (b)
6.49 cm ² round, convergent	24 (c)
Effect of spanwise nozzle vertical location on longitudinal aerodynamic characteristics for $p_{t,j}/p_\infty = 3.25$, $\delta_{TE} = 15^\circ$, $\delta_{LE} = \delta_C = 0^\circ$, H ₂ canard	25
Effect of leading-edge flap deflection on longitudinal aerodynamic characteristics in the presence of spanwise-blowing nozzle for Conf 14 (6.94 cm ² rectangular flush, convergent, $x_n/c_r = 0.493$, $h_n/c_r = 0.068$), $p_{t,j}/p_\infty = 3.25$, $\delta_{TE} = 15^\circ$, $\delta_C = 0^\circ$, H ₂ canard	26
Effect of canard incidence on longitudinal aerodynamic characteristics in the presence of spanwise-blowing nozzle for Conf 14 (6.94 cm ² rectangular flush, convergent, $x_n/c_r = 0.493$, $h_n/c_r = 0.068$), $p_{t,j}/p_\infty = 3.62$, $\delta_{TE} = 15^\circ$, $\delta_{LE} = 20^\circ$, H ₂ canard	27
Effect of spanwise nozzle throat area on incremental lift for $\alpha = 14^\circ$ and $\alpha = 36^\circ$, $\delta_{TE} = 15^\circ$, $\delta_{LE} = \delta_C = 0^\circ$, H ₂ canard	28

Effect of spanwise nozzle geometry on incremental lift for $\alpha = 14^\circ$ and $\alpha = 36^\circ$, $\delta_{TE} = 15^\circ$, $\delta_{LE} = \delta_C = 0^\circ$, H ₂ canard	29
Effect of spanwise nozzle axial location on incremental lift for $\alpha = 14^\circ$ and $\alpha = 36^\circ$, $\delta_{TE} = 15^\circ$, $\delta_{LE} = \delta_C = 0^\circ$, H ₂ canard	30

DISCUSSION

Basic Longitudinal Characteristics

The basic longitudinal aerodynamic data for all configurations tested are presented in figures 5 to 18 for several nozzle pressure ratios. Plotted in each figure are angle of attack, drag-minus-thrust coefficient, and pitching-moment coefficient as a function of total lift coefficient. The basic coefficient data (without thrust removed) are presented because they are representative of the specific excess power for each configuration. Specific excess power is used as a measure of aircraft maneuvring performance and is defined by the following equation:

$$\text{Specific excess power} = \left(\frac{T - D}{\text{Weight}} \right) \text{Velocity} \quad (9)$$

It should be noted that for a given weight and flight condition specific excess power varies only with thrust and drag. It should also be noted that drag-minus-thrust coefficients presented in figures 5 to 18 are defined as positive in the drag direction. Thus, negative values of $C_{(D-T)}$ indicate an excess thrust, $C_{(D-T)} = 0$ indicates thrust equals drag, and positive values of $C_{(D-T)}$ indicate a drag level higher than the thrust level. Of course, positive values of excess power (negative $C_{(D-T)}$) can be converted into an acceleration or an increased rate of climb.

In general, the basic longitudinal data show an increase in lift coefficient and the angle of attack for wing stall as nozzle pressure ratio is increased. The total model drag-minus-thrust coefficient decreases with increasing nozzle pressure ratio (primarily as a result of increased thrust) and, since the thrust-induced lift effects occur aft of the configuration reference center-of-gravity location, the pitching-moment coefficient becomes more negative (larger nose-down moments). Because of the effects of jet exhaust on the lift characteristics, the pitching-moment curve is extended and pitch-up is generally delayed to higher lifts. The lift-curve slope generally increased and the pitching-moment-curve slope decreased with increasing nozzle pressure ratio.

Since the VEO-wing configuration employs several high lift concepts, it is helpful to examine the individual effects of each concept on the total lift characteristics. The individual effects of trailing-edge flap deflection, nozzle thrust, thrust vectoring, and spanwise blowing are presented in figure 19. The aerodynamic effects on lift generated by deflection of the trailing-edge flaps were obtained by comparison of the jet-off flap-deflection data. The

increment obtained by increasing trailing-edge flap deflection from 0° to 15° is illustrated on the left side of figure 19. As shown, the trailing-edge flaps lose their effectiveness at high angles of attack. This loss of effectiveness is probably due to flow separation on the wing and flaps.

The effects of nozzle thrust are illustrated on the left side of figure 19 as the difference between the jet-on lift curve and the jet-off lift curve. The jet effect shown is a very large one. The nozzle pressure ratio is large, and at high angles of attack the thrust component in the lift direction is substantial. In addition, a certain amount of thrust vectoring is being achieved, even for the $\delta_{TE} = 0^\circ$ case, as the nozzle and slope of the trailing-edge flap surface combine to turn the flow. This vectoring increases the thrust component in the lift direction.

The effects of deflecting the trailing-edge flaps with the jet on are illustrated on the right side of figure 19 for a given nozzle pressure ratio. The increment in lift between the $\delta_{TE} = 15^\circ$ and the $\delta_{TE} = 0^\circ$ data includes the thrust vectoring effect as well as the aerodynamic flap effect. For reference, the dashed line shows the aerodynamic flap effect for the jet-off condition which is presented on the left side of the figure. It should be noted that the effect of flap deflection is more pronounced at the lower angles of attack tested, probably as a result of attached flow over the wing. Supercirculation effects have been shown to be more significant in these attached flow regions (ref. 16).

Finally, the increment due to spanwise blowing is obtained from the difference between the jet-on spanwise-blowing curve and the jet-on baseline nozzle (no spanwise blowing) curve. This increase in lift is probably a result of the formation and stabilization of the leading-edge vortex by spanwise blowing (refs. 20 to 24). A major point here is that these increases in lift are in addition to those already obtained from thrust vectoring. It should be noted also that spanwise blowing is obviously more effective at the higher angles of attack where large amounts of flow separation are likely to occur.

Comparisons of Spanwise Nozzle Variations

The comparison plots shown in figures 20 to 27 present longitudinal data. All comparison data shown are for a constant nominal nozzle pressure ratio of approximately 3.25, unless otherwise noted.

Spanwise blowing.- When comparing the baseline configuration (no spanwise blowing) to the spanwise-blowing cases (see figs. 20(a) and 20(b)), it is apparent that spanwise blowing provides large increases in C_L for a given nozzle pressure ratio, improvements in drag due to lift characteristics (polar shape), and generally larger nose-down pitching moments. Spanwise blowing also tended to increase the lift-curve slope and to decrease the negative pitching-moment curve slope slightly. These additional improvements occur because the spanwise blowing is aiding in the formation and stabilization of the lift-producing leading-edge vortex. Once this vortex has been stabilized, further increases in nozzle pressure ratio seem to increase the effective camber of the wing.

Spanwise nozzle throat area.— The effects of spanwise nozzle throat area are shown in figures 20(a) and 20(b) for the round convergent nozzles. In figure 20(a) the 1.60 cm² (approximately 7 percent of total engine nozzle throat area) spanwise nozzle is seen to provide a significant increase in lift as well as a significant improvement in polar shape over the baseline nozzle with no spanwise blowing. The 3.22 cm² (approximately 14 percent of total engine nozzle throat area) spanwise nozzle produces an even larger increment in lift although the increase is not linearly proportional to the increase in throat area. The polar shape is also improved by increasing spanwise nozzle throat area, especially at the moderate to high angles of attack tested (20° to 40°).

Figure 20(b) provides a comparison between the 3.25 cm² and the 6.49 cm² (approximately 28 percent of total engine nozzle throat area) spanwise nozzles ($h_n/c_r = 0.0935$) and the baseline nozzle. Significant increases in lift coefficient are obtained by use of spanwise blowing, similar to the results shown in figure 20(a). As discussed previously, however, the gains in lift are not linearly proportional to the increase in spanwise nozzle throat area. As a result, polar improvements for the 6.49 cm² spanwise nozzle are delayed to the higher angles of attack (30° to 40°), and the 3.25 cm² spanwise nozzle provides polar improvement at moderate angles of attack.

The increases in C_L with increases in spanwise nozzle throat area, shown in figure 20, are consistent with results obtained in previous studies of the VEO-wing concept (refs. 17 and 18). These trends are summarized in figure 21, where the lift increment due to spanwise blowing is plotted as a function of spanwise nozzle throat area for a nozzle pressure ratio of 3.25. The data are shown for angles of attack of 20° and 36°, but the observations are true throughout the angle-of-attack range tested. The results show that the rate of increase in incremental lift per unit of spanwise nozzle throat area decreases with increasing spanwise nozzle throat area. The relative increase in magnitude of incremental lift as angle of attack increases should also be noted. This observation suggests an increased requirement for the formation and stabilization of the leading-edge vortex at high angles of attack.

Spanwise nozzle geometry.— The effects of spanwise nozzle external geometry are illustrated in figure 22(a). Three spanwise nozzle external shapes (round, rectangular, and rectangular flush) are compared with the baseline configuration (no spanwise nozzle) as a reference. In all cases spanwise blowing provided significant improvements over the baseline nozzle without spanwise blowing. Although relatively small changes in lift coefficient are shown for varying external nozzle geometry, several trends may be noted. At the lower angles of attack tested, the rectangular flush spanwise nozzle provides the largest lift improvements and best polar shape. At higher angles of attack, however, the round spanwise nozzle produces the highest lift coefficient and best polar shape. One reason for this performance crossover may be suggested. At low angles of attack the round spanwise nozzle, which protrudes into the wing flow field, may be disrupting the flow field on the inboard portion of the wing, thus reducing the lift benefits. At high angles of attack the exhaust from the round nozzle is probably penetrating the wing flow field farther outboard into possible separated regions, thus producing increases in lift that are larger than those provided by the rectangular flush nozzle.

Figure 22(b) shows a comparison between the 6.49 cm² round spanwise nozzle and the 6.94 cm² rectangular flush spanwise nozzle for $\delta_{TE} = 0^\circ$. Although the magnitudes are somewhat different, the trends are the same as discussed for $\delta_{TE} = 15^\circ$ data.

A comparison of internal nozzle shape (nozzle type) is presented in figure 23. A round spanwise nozzle was tested with a convergent internal geometry and a converging-diverging (C-D) internal geometry. The results indicate that nozzle internal shape and hence spanwise nozzle exhaust exit velocity have little or no effect on performance at $M = 0.186$.

Spanwise nozzle axial and vertical locations.- The effects of spanwise nozzle axial location are presented in figure 24. Figure 24(a) presents the effects of three axial locations, $x_n/c_r = 0.416$, $x_n/c_r = 0.527$, and $x_n/c_r = 0.622$, on the aerodynamic performance of the 3.25 cm² round, convergent spanwise nozzle, and figure 24(b) shows the effects of the same three axial locations on the performance of the 3.22 cm² round, convergent-divergent spanwise nozzle. In both cases axial location of the spanwise nozzle has little effect on the longitudinal characteristics. A slight trend of increasing lift with forward movement of the spanwise nozzle may be noted except at the highest angles of attack investigated. There is essentially no effect of spanwise nozzle axial location on polar shape or pitching moment.

Figure 24(c) presents the effects of the three axial positions with the larger 6.49 cm² round, convergent spanwise nozzles. At low and moderate angles of attack the forward spanwise nozzle position produces the highest lift coefficients. At high angles of attack both the mid position and the forward position spanwise nozzles are about equal in lift augmentation. The aft spanwise nozzle position produced the lowest lift augmentation throughout the angle-of-attack range tested. At moderate lift coefficients, the forward spanwise nozzle position provides polar improvements over the mid and aft spanwise nozzle locations. At high lift coefficients, there is little difference between forward and mid positions on polar shape.

These results indicate that spanwise nozzle throat area is an important factor affecting the sensitivity of spanwise-blowing performance to other configuration changes. As the spanwise nozzle throat area increases, the effects due to other configuration modifications appear to become more pronounced.

The effect of spanwise nozzle vertical location is illustrated in figure 25 for the 3.25 cm² round, convergent spanwise nozzle. It is apparent from this figure that vertical location had little or no effect on the aerodynamic performance characteristics. It must be noted, however, that the spanwise nozzle vertical position change was very small. Also, had the 6.49 cm² spanwise nozzle been used for the vertical location study, the effects might have been more pronounced.

Leading-edge flap effects.- As shown in figure 26, a leading-edge flap is an effective device for increasing lift and improving polar shape at angles of attack above 22° by delaying leading-edge separation. The leading-edge flap provided significant improvements in lift and polar shape in addition to those already provided by spanwise blowing and thrust vectoring. The improved stability due to the leading-edge flap deflection should also be noted.

Canard incidence effects.- At high angles of attack, a close-coupled canard can have a beneficial effect on configuration lift and polar shape (refs. 1 to 4). Figure 27 presents the effect of canard incidence on the aerodynamic characteristics of the VEO-wing concept. A canard incidence of -10° (canard leading edge down) provides small improvements in lift and significant improvements in polar shape throughout the angle-of-attack range tested; however, it is expected that these benefits would vanish for the trimmed configuration.

Incremental lift coefficient.- Another method of viewing spanwise-blowing nozzle design parameters is through the use of incremental lift ΔC_L , as discussed in the data-reduction section. Comparison plots illustrating the effects of spanwise nozzle throat area, external geometry, and axial location are presented in figures 28 to 30. Incremental lift coefficients are presented for angles of attack of 14° and 36° and are plotted as a function of engine nozzle pressure ratio. In general, all incremental lift coefficients increase with increasing nozzle pressure ratio.

The effects of spanwise nozzle throat area are presented in figure 28. At $\alpha = 14^\circ$ the increases in incremental lift obtained with no spanwise blowing (baseline configuration) are of the same order as those obtained with spanwise blowing. At $\alpha = 36^\circ$, however, it is apparent that incremental lift increases as spanwise nozzle throat area increases throughout the nozzle pressure ratio range tested.

The effects of spanwise nozzle external geometry are presented in figure 29. At $\alpha = 14^\circ$ the rectangular-flush nozzle provided the largest incremental lift improvements (throughout the nozzle pressure ratio range tested) with the round spanwise nozzle providing the fewest gains. At $\alpha = 36^\circ$ these results are reversed. Some possible reasons for this performance crossover were previously discussed.

The effects of spanwise nozzle axial location are shown in figure 30. As previous observations suggest, the effects of axial location on incremental lift are small.

CONCLUSIONS

An investigation has been conducted in the Langley V/STOL tunnel to determine the effects of spanwise nozzle throat area, internal and external geometry, and location on the longitudinal aerodynamic characteristics of a powered lift model using vectored thrust and spanwise-blowing concepts. Effects of nozzle pressure ratio, wing leading- and trailing-edge flaps, and canard incidence were also investigated. Wind-tunnel data were obtained at $M = 0.186$ for a range of model angle of attack from 14° to 40° and engine nozzle pressure ratios from 1.0 (jet off) to approximately 3.75. Results from this study indicate the following:

1. Spanwise blowing significantly improved the longitudinal aerodynamic characteristics of a canard-wing-body configuration beyond those improvements associated with vectoring the main exhaust flow over the wing trailing-edge flap.

2. Increasing spanwise nozzle throat area and nozzle pressure ratio increased lift in all cases.

3. The effects of spanwise nozzle external geometry on aerodynamic performance were a function of angle of attack and were generally small when compared to the effects of spanwise nozzle throat area. The rectangular flush spanwise nozzle provided greatest benefits at the lower angles of attack, while the circular nozzle shape improved performance at the higher angles of attack.

4. Axial location of the spanwise nozzle had little effect on aerodynamic performance for the smaller throat area spanwise nozzles. For the 6.49 cm^2 spanwise nozzles, however, moving the spanwise nozzle forward tended to improve performance.

5. Vertical location of the spanwise nozzle had very little effect on aerodynamic performance for the configuration tested.

6. Both wing leading-edge flap deflections and canard incidence provided significant improvements in the presence of spanwise blowing at high angles of attack; however, it is felt that most benefits from the canard would be forfeited in order to trim the configuration.

7. Spanwise nozzle throat area (spanwise nozzle mass flow) appeared to be an important factor affecting the sensitivity of spanwise-blowing performance to configuration changes.

Langley Research Center
National Aeronautics and Space Administration
Hampton, VA 23665
April 14, 1978

REFERENCES

1. Gloss, Blair B.; and McKinney, Linwood W.: Canard-Wing Lift Interference Related to Maneuvering Aircraft at Subsonic Speeds. NASA TM X-2897, 1973.
2. Henderson, William P.: The Effect of Canard and Vertical Tails on the Aerodynamic Characteristics of a Model With a 59° Sweptback Wing at a Mach Number of 0.30. NASA TM X-3088, 1974.
3. Gloss, Blair B.: Effect of Wing Planform and Canard Location and Geometry on the Longitudinal Aerodynamic Characteristics of a Close-Coupled Canard Wing Model at Subsonic Speeds. NASA TN D-7910, 1975.
4. Re, Richard J.; and Capone, Francis J.: An Investigation of a Close-Coupled Canard as a Direct Side-Force Generator on a Fighter Model at Mach Numbers From 0.40 to 0.90. NASA TN D-8510, 1977.
5. Capone, Francis J.: Effect of Various Wing High-Lift Devices on the Longitudinal Aerodynamic Characteristics of a Swept-Wing Fighter Model at Transonic Speeds. NASA TM X-3204, 1975.
6. Ray, Edward J.; McKinney, Linwood W.; and Carmichael, Julian G.: Maneuver and Buffet Characteristics of Fighter Aircraft. NASA TN D-7131, 1973.
7. Henderson, William P.; and Huffman, Jarrett K.: Effect of Wing Design on the Longitudinal Aerodynamic Characteristics of a Wing-Body Model at Subsonic Speeds. NASA TN D-7099, 1972.
8. Lowry, John G.; Riebe, John M.; and Campbell, John P.: The Jet-Augmented Flap. Preprint No. 715, S.M.F. Fund Paper, Inst. Aeronaut. Sci., Jan. 1957.
9. Campbell, John P.: Overview of Powered-Lift Technology. Powered-Lift Aerodynamics and Acoustics, NASA SP-406, 1976, pp. 1-27.
10. Osborn, R. F.; and Oates, G. S.: Wind Tunnel Investigation of Three Powered-Lift STOL Concepts. V/STOL Aerodynamics, AGARD-CP-143, Apr. 1974, pp. 4-1 - 4-12.
11. Phelps, Arthur E., III; Johnson, Joseph L., Jr.; and Margason, Richard J.: Summary of Low-Speed Aerodynamic Characteristics of Upper-Surface-Blown Jet-Flap Configurations. Powered-Lift Aerodynamics and Acoustics, NASA SP-406, 1976, pp. 63-87.
12. Johnson, Joseph L., Jr.; and Phelps, Arthur E., III: Low-Speed Aerodynamics of the Upper-Surface Blown Jet Flap. [Preprint] 740470, Soc. Automot. Eng., Apr.-May 1974.
13. Capone, Francis J.: The Effects on Propulsion-Induced Aerodynamic Forces of Vectoring a Partial-Span Rectangular Jet at Mach Numbers From 0.40 to 1.20. NASA TN D-8039, 1975.

14. Corson, Blake W., Jr.; Capone, Francis J.; and Putnam, Lawrence E.: Lift Induced on a Swept Wing by a Two-Dimensional Partial-Span Deflected Jet at Mach Numbers From 0.20 to 1.30. NASA TM X-2309, 1971.
15. Pennington, Jack E.: Simulation Study of Effects of Thrust Vectoring and Induced Lift Due to Thrust Vectoring on Combat Effectiveness of a Fighter Aircraft. NASA TM X-3202, 1975.
16. Capone, Francis J.: A Summary of Experimental Research on Propulsive-Lift Concepts in the Langley 16-Foot Transonic Tunnel. AIAA Paper No. 75-1315, Sept.-Oct. 1975.
17. Woodrey, R. W.; Whitten, P. D.; Smith, C. W.; and Bradley, R. G.: An Experimental Investigation of a Vectored-Engine-Over-Wing Powered-Lift Concept. Volume I - Low Speed and Transonic Tests. AFFDL-TR-76-92, Vol. I, U.S. Air Force, Sept. 1976.
18. Bradley, R. G.; Jeffries, R. R.; and Capone, F. J.: A Vectored-Engine-Over-Wing Propulsive-Lift Concept. AIAA Paper No. 76-917, Sept. 1976.
19. Huffman, Jarrett K.; and Fox, Charles H., Jr.: Subsonic Longitudinal Aerodynamic Characteristics of a Vectored-Engine-Over-Wing Configuration Having Spanwise Leading Edge Vortex Enhancement. NASA TM X-73955, 1977.
20. Bradley, R. G.; Whitten, P. D.; and Wray, W. O.: Leading-Edge-Vortex Augmentation in Compressible Flow. AIAA Paper No. 75-124, Jan. 1975.
21. Bradley, R. G.; and Wray, W. O.: A Conceptual Study of Leading-Edge-Vortex Enhancement by Blowing. J. Airc., vol. 11, no. 1, Jan. 1974, pp. 33-38.
22. Campbell, James F.: Effects of Spanwise Blowing on the Pressure Field and Vortex-Lift Characteristics of a 44° Swept Trapezoidal Wing. NASA TN D-7907, 1975.
23. Campbell, James F.: Augmentation of Vortex Lift by Spanwise Blowing. J. Aircr., vol. 13, no. 9, Sept. 1976, pp. 727-732.
24. Erickson, Gary E.; and Campbell, James F.: Improvement of Maneuver Aerodynamics by Spanwise Blowing. NASA TP-1065, 1977.

TABLE I.- CONFIGURATION DESCRIPTIONS

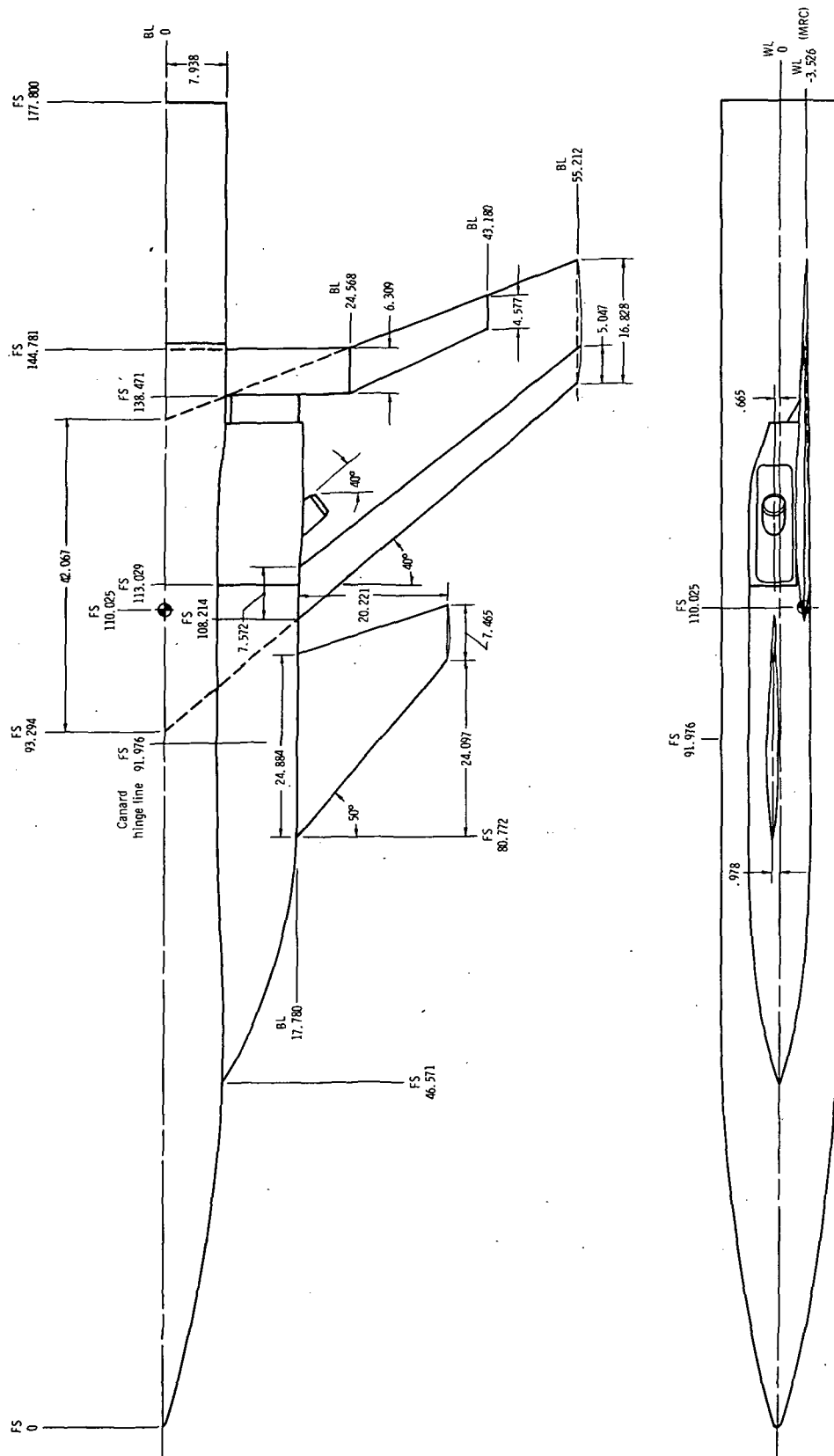
Conf	x_n/c_r	h_n/c_r	Spanwise internal geometry	Spanwise nozzle throat area per side, cm^2	Total main exhaust nozzle throat area, cm^2	Total nozzle throat area, cm^2	Total main exhaust nozzle exit area, cm^2	Wedge angle, deg	Description	Figure
1	-----	-----	-----	0	46.26	46.26	62.30	20	Baseline	1(e)
5	0.527	0.0935	Convergent	3.25	39.81	46.31	60.12	22	Round	1(f)
6	.416	.0935	Convergent	3.25	39.81	46.31	60.12	22	Round	1(f)
7	.622	.0935	Convergent	3.25	39.81	46.31	60.12	22	Round	1(f)
a8	.527	.0793	Convergent	3.22	39.81	46.25	60.12	22	Round	1(g)
a9	.527	.0793	Convergent	1.60	42.94	46.14	61.89	20	Round	1(g)
10	.527	.0935	Convergent	6.49	33.59	46.57	55.85	25	Round	1(f)
11	.416	.0935	Convergent	6.49	33.59	46.57	55.85	25	Round	1(f)
12	.622	.0935	Convergent	6.49	33.59	46.57	55.85	25	Round	1(f)
13	.532	.0680	Convergent	6.74	33.59	47.07	55.85	25	Round	1(f)
14	.493	.0680	Convergent	6.94	33.59	47.47	55.85	25	Rectangular	1(h)
									Rectangular flush	1(i)
15	.527	.0935	C-D	3.22	39.81	46.25	60.06	22	Round	1(f)
16	.416	.0935	C-D	3.22	39.81	46.25	60.06	22	Round	1(f)
17	.622	.0935	C-D	3.22	39.81	46.25	60.06	22	Round	1(f)

^aSmall external diameter.

TABLE II.- INDEX TO BASIC DATA

Conf	δ_{TE} , deg		δ_{LE} , deg	δ_C , deg	Canard planform	Spanwise nozzle throat area, cm ²	x_n/c_r	h_n/c_r	Description	Figure
	O	I								
1	0	0	0	0	H2	0	---	---	---	5 (a)
1	15	15	0	0	H2	0	---	---	---	5 (b)
5	15	15	0	0	H2	3.25	0.527	0.0935	Round/Conv	6
6	15	15	0	0	H2	3.25	.416	.0935	Round/Conv	7
7	15	15	0	0	H2	3.25	.622	.0935	Round/Conv	8
a8	15	15	0	0	H2	3.22	.527	.0793	Round/Conv	9
a9	15	15	0	0	H2	1.60	.527	.0793	Round/Conv	10
10	15	15	0	0	H2	6.49	.527	.0935	Round/Conv	11 (a)
10	0	0	0	0	H2	6.49	.527	.0935	Round/Conv	11 (b)
10	30	30	20	-20	H3	6.49	.527	.0935	Round/Conv	11 (c)
10	30	30	20	20	H3	6.49	.527	.0935	Round/Conv	11 (d)
11	15	15	0	0	H2	6.49	.416	.0935	Round/Conv	12
12	15	15	0	0	H2	6.49	.622	.0935	Round/Conv	13
13	15	15	0	0	H2	6.74	.532	.0680	Rectangular/Conv	14
14	15	15	0	0	H2	6.94	.493	.0680	Rectangular flush/Conv	15 (a)
14	0	0	0	0	H2	6.94	.493	.0680	Rectangular flush/Conv	15 (b)
14	15	15	20	0	H2	6.94	.493	.0680	Rectangular flush/Conv	15 (c)
14	15	15	20	-10	H2	6.94	.493	.0680	Rectangular flush/Conv	15 (d)
14	15	30	0	0	H2	6.94	.493	.0680	Rectangular flush/Conv	15 (e)
14	30	30	0	0	H2	6.94	.493	.0680	Rectangular flush/Conv	15 (f)
15	15	15	0	0	H2	3.22	.527	.0935	Round/C-D	16
16	15	15	0	0	H2	3.22	.416	.0935	Round/C-D	17
17	15	15	0	0	H2	3.22	.622	.0935	Round/C-D	18

^aSmall external diameter. See figure 1(g).



(a) Basic model with H₂ canard.

Figure 1.- Drawing of model components. (All dimensions in cm unless noted.)

Wing Geometry

Mean geometric chord 31.250

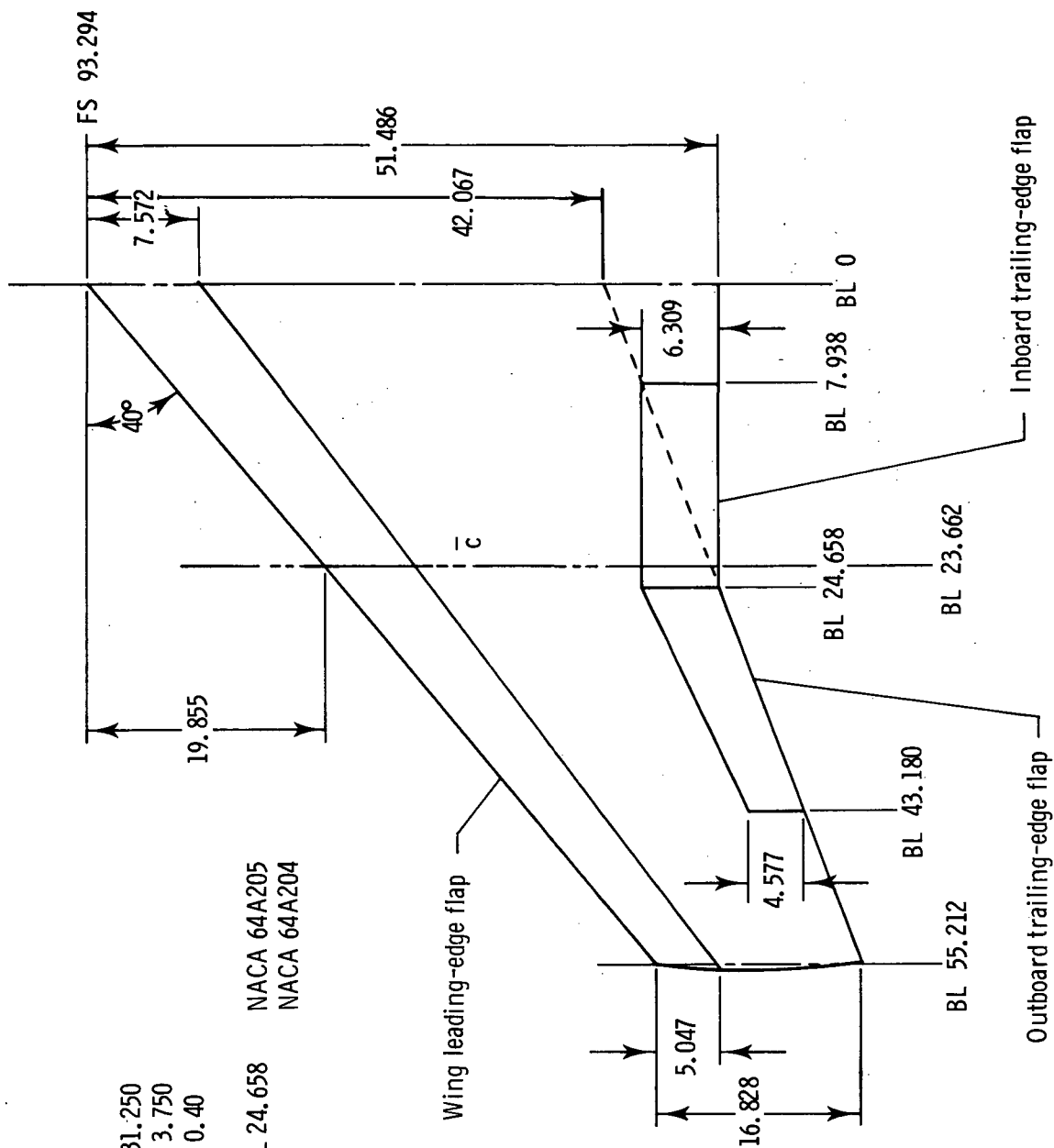
Aspect ratio 3.750

Taper ratio 0.40

Airfoil Sections:

Root (BL 17.780) to BL 24.658 NACA 64A205

Tip (BL 55.212) NACA 64A204

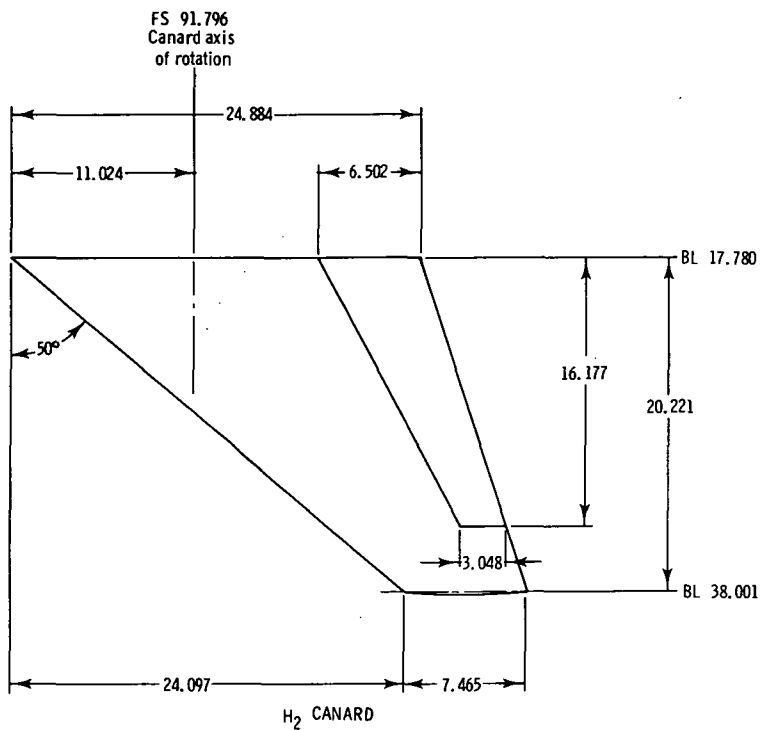


(b) Wing details.

Figure 1.- Continued.

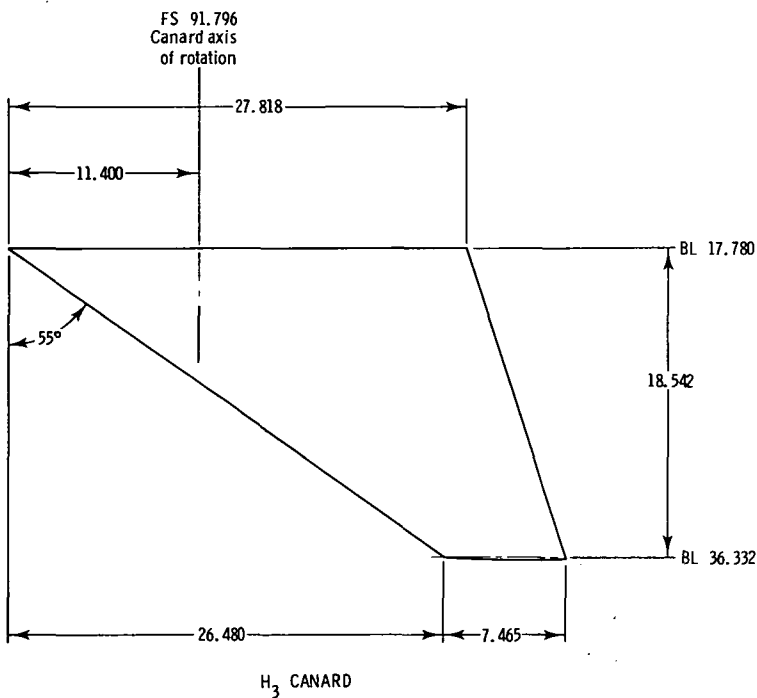
H₂ Canard Geometry

Mean geometric chord 17.738
 Aspect ratio 2.50
 Taper ratio 0.30
 Airfoil section 4% biconvex
 Exposed area, 654.129 cm²



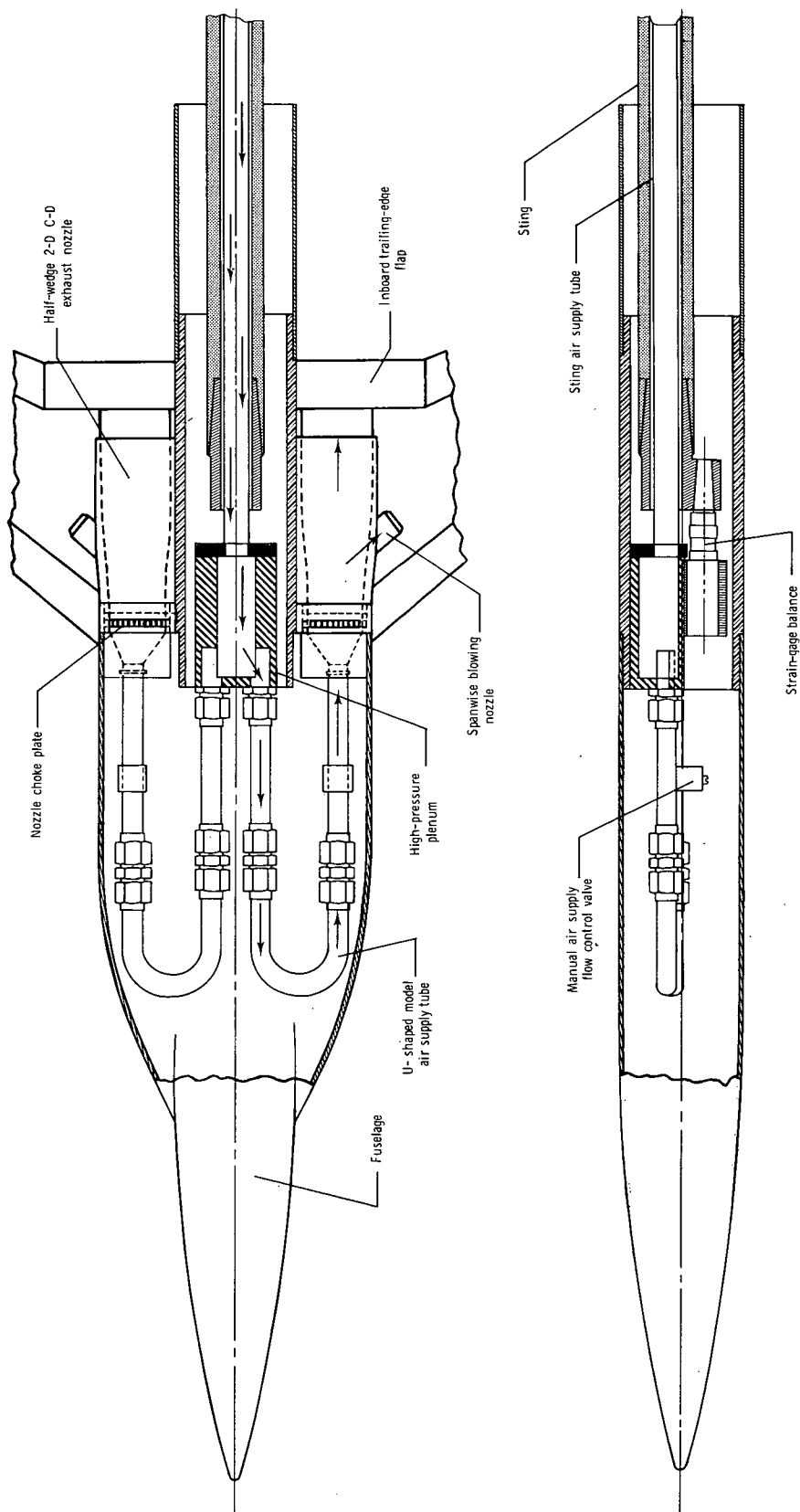
H₃ Canard Geometry

Mean geometric chord 19.598
 Aspect ratio 2.102
 Taper ratio 0.268
 Airfoil section 4% biconvex
 Exposed area, 654.217 cm²



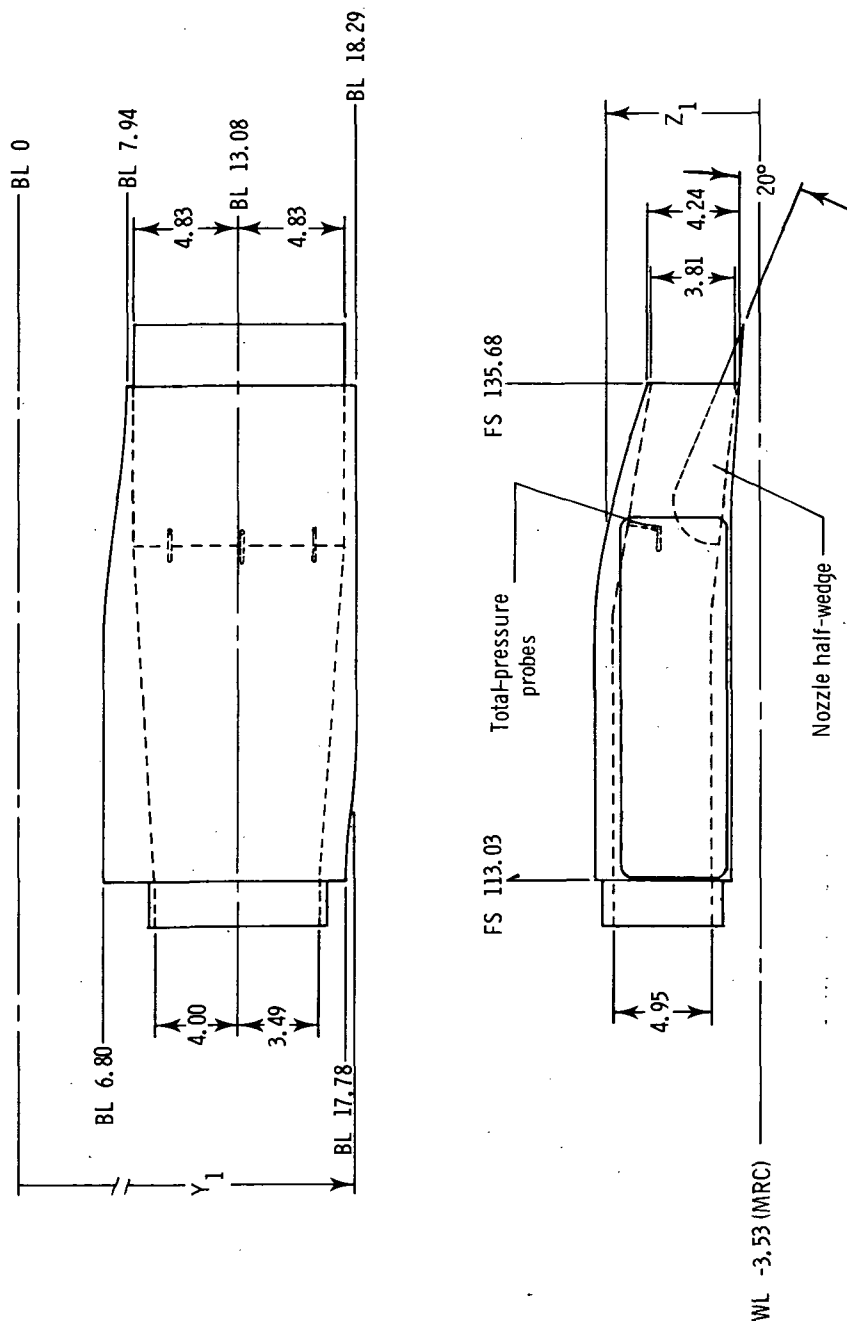
(c) H₂ and H₃ canard details.

Figure 1.- Continued.



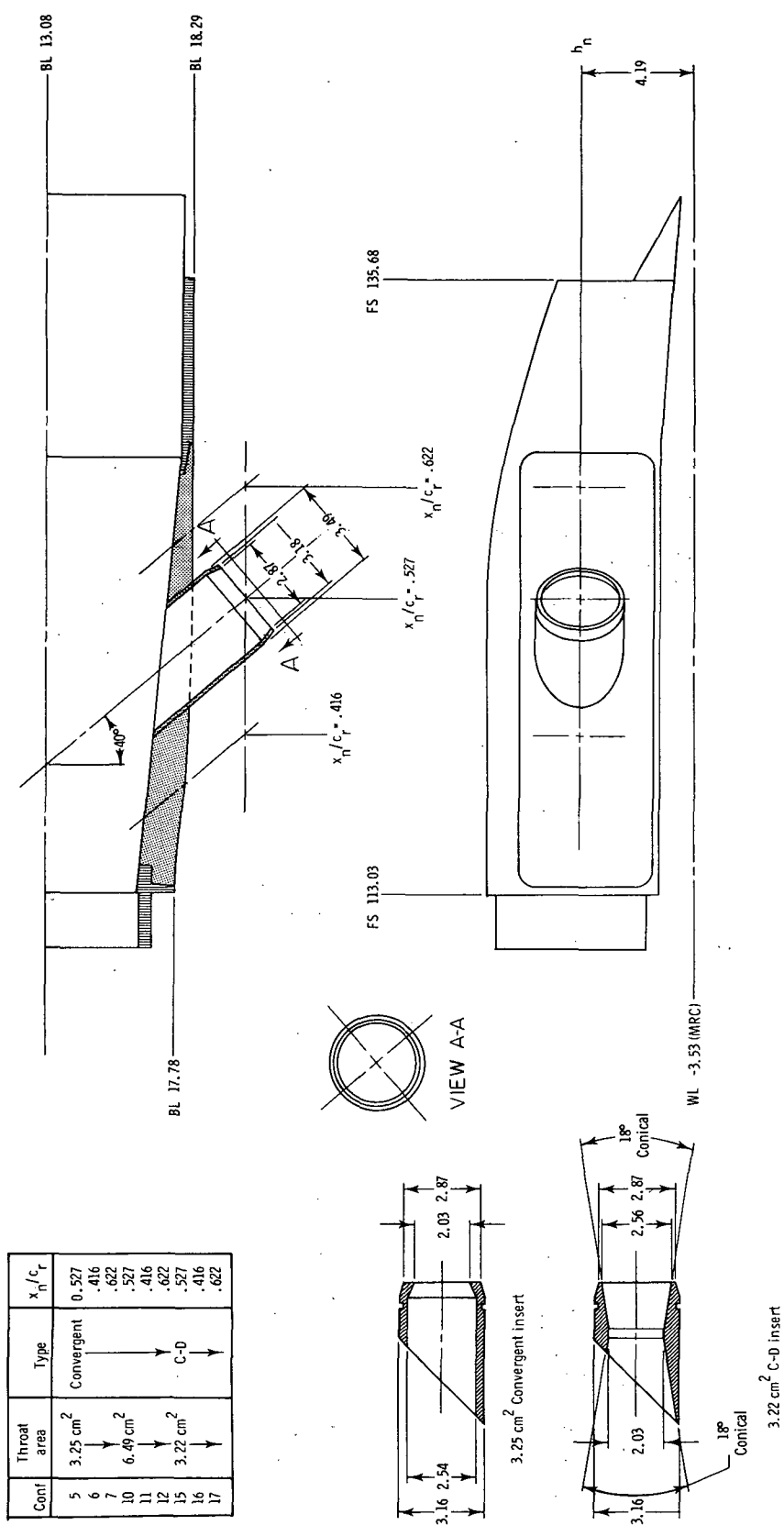
(d) Model air-supply system and balance arrangement.

Figure 1.- Continued.



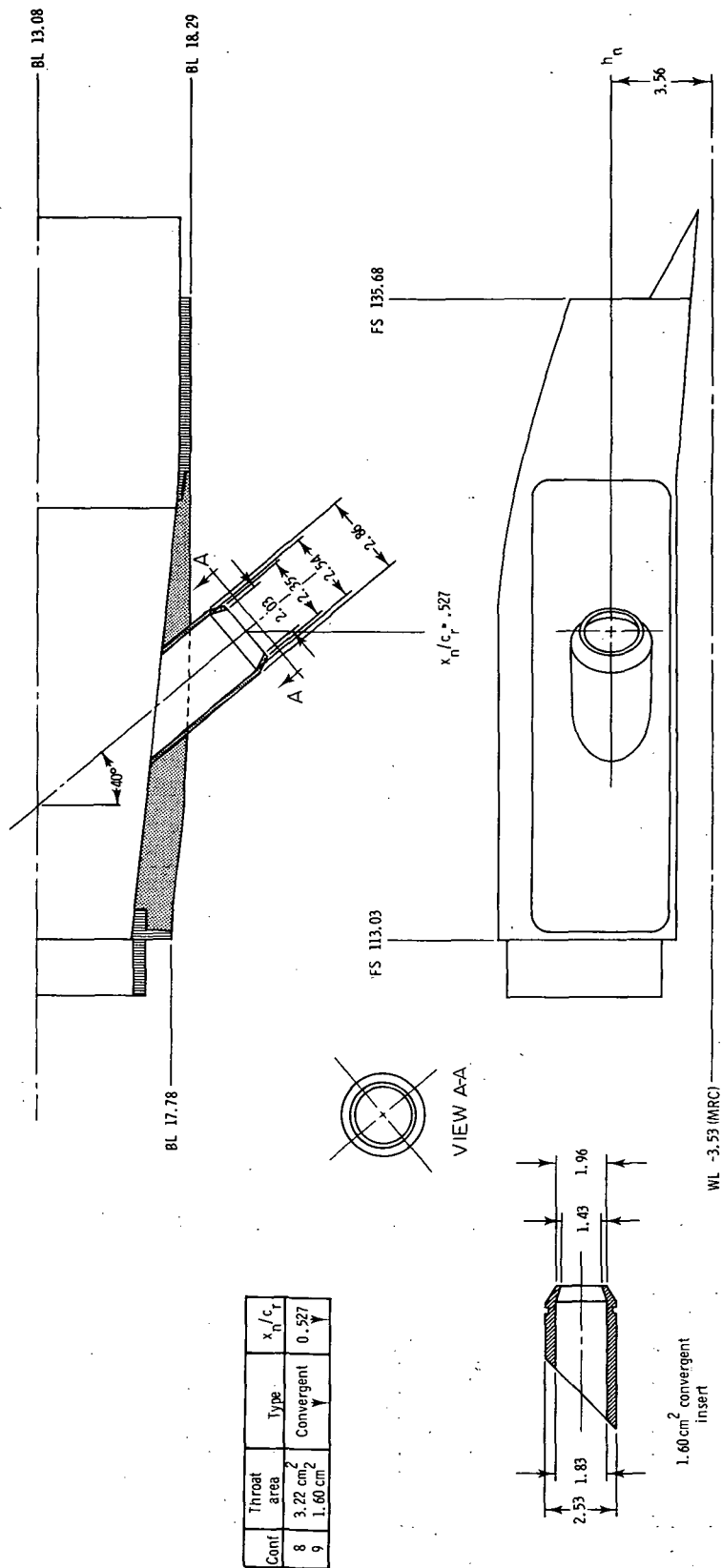
(e) Half-wedge two-dimensional C-D exhaust nozzle, Conf 1 (no spanwise blowing); total exhaust nozzle throat area is 46.26 cm².

Figure 1.- Continued.



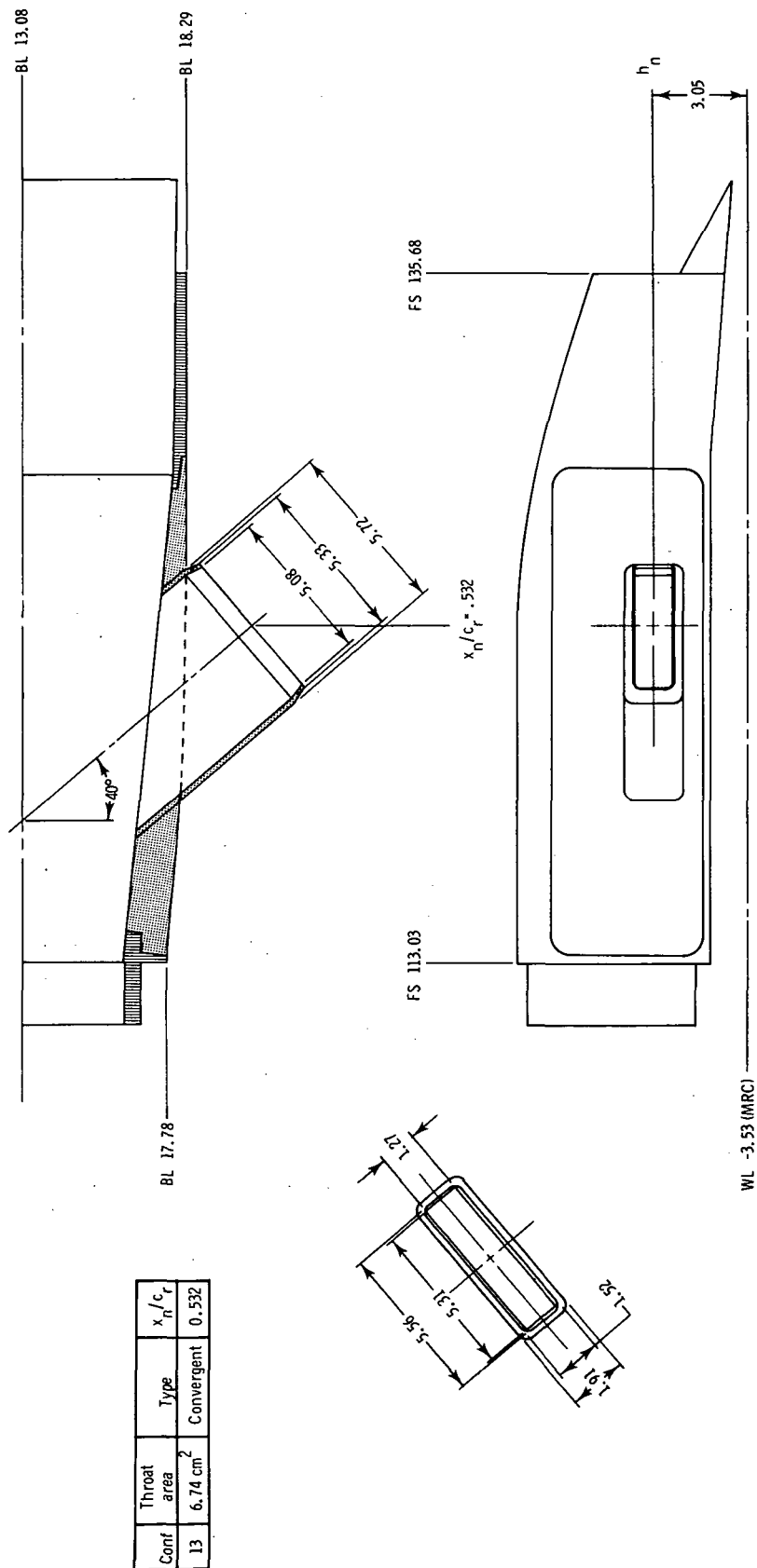
(f) Round spanwise nozzle; $h_n/c_r = 0.0935$.

Figure 1.- Continued.



(g) Round spanwise nozzle; $h_n/c_r = 0.0793$.

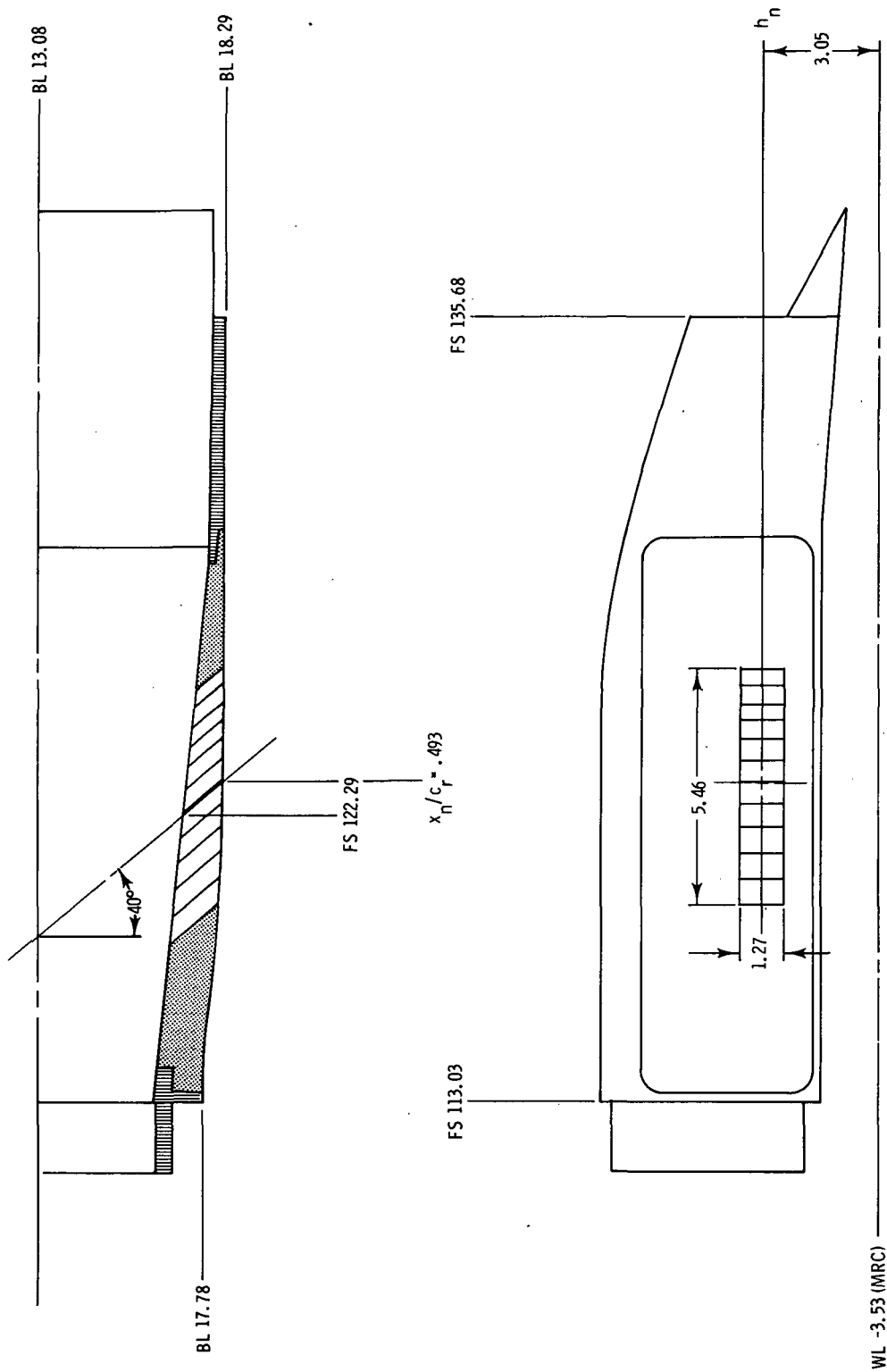
Figure 1.- Continued.



(h) Rectangular spanwise nozzle; $h_n/c_r = 0.068$.

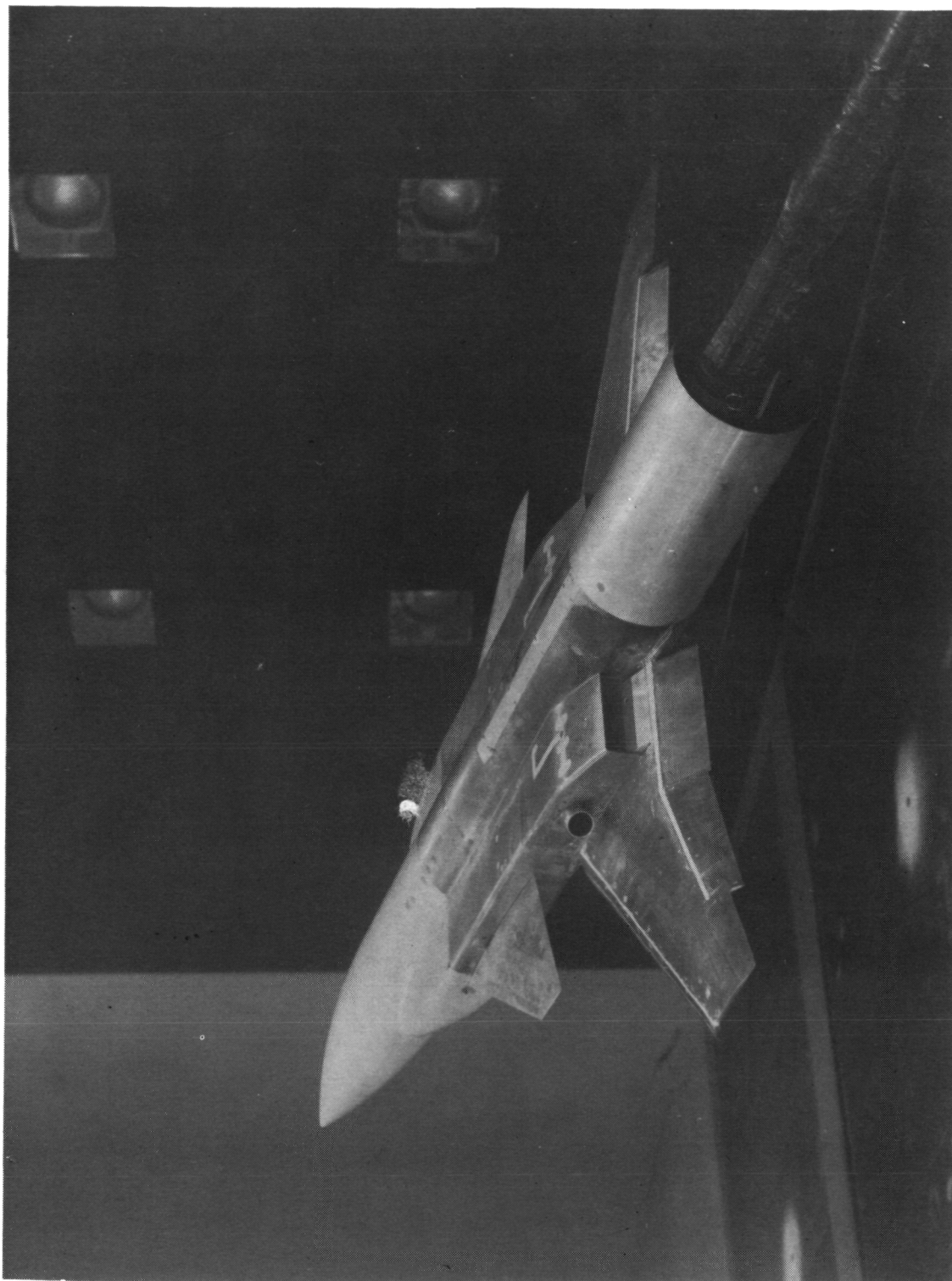
Figure 1.- Continued.

Conf	Throat area	Type	x_n/c_r
14	6.94 cm ²	Convergent	0.493



(i) Rectangular flush spanwise nozzle; $h_n/c_r = 0.068$.

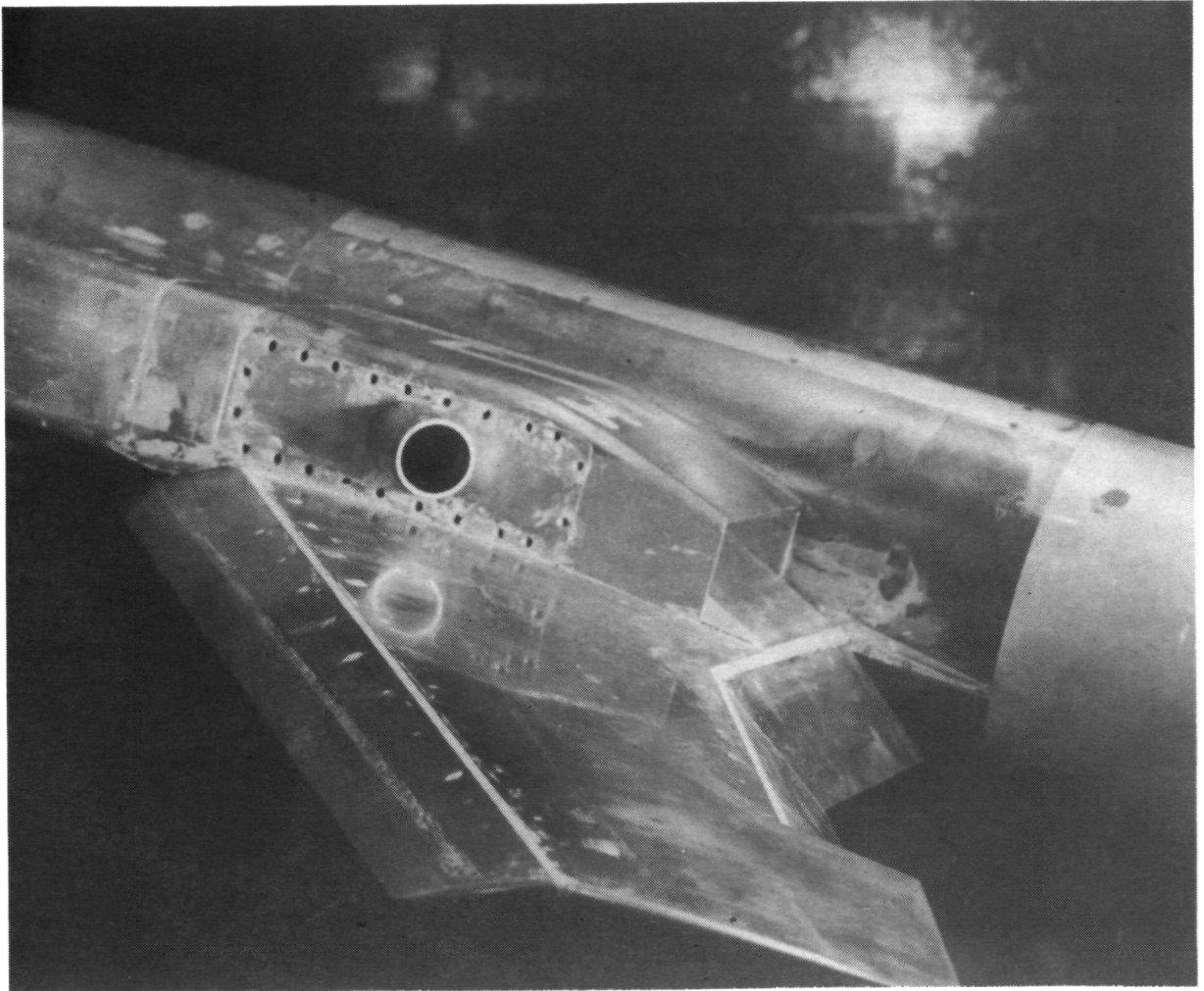
Figure 1.- Concluded.



L-78-46

(a) VEO-wing model installed in Langley V/STOL tunnel test section.

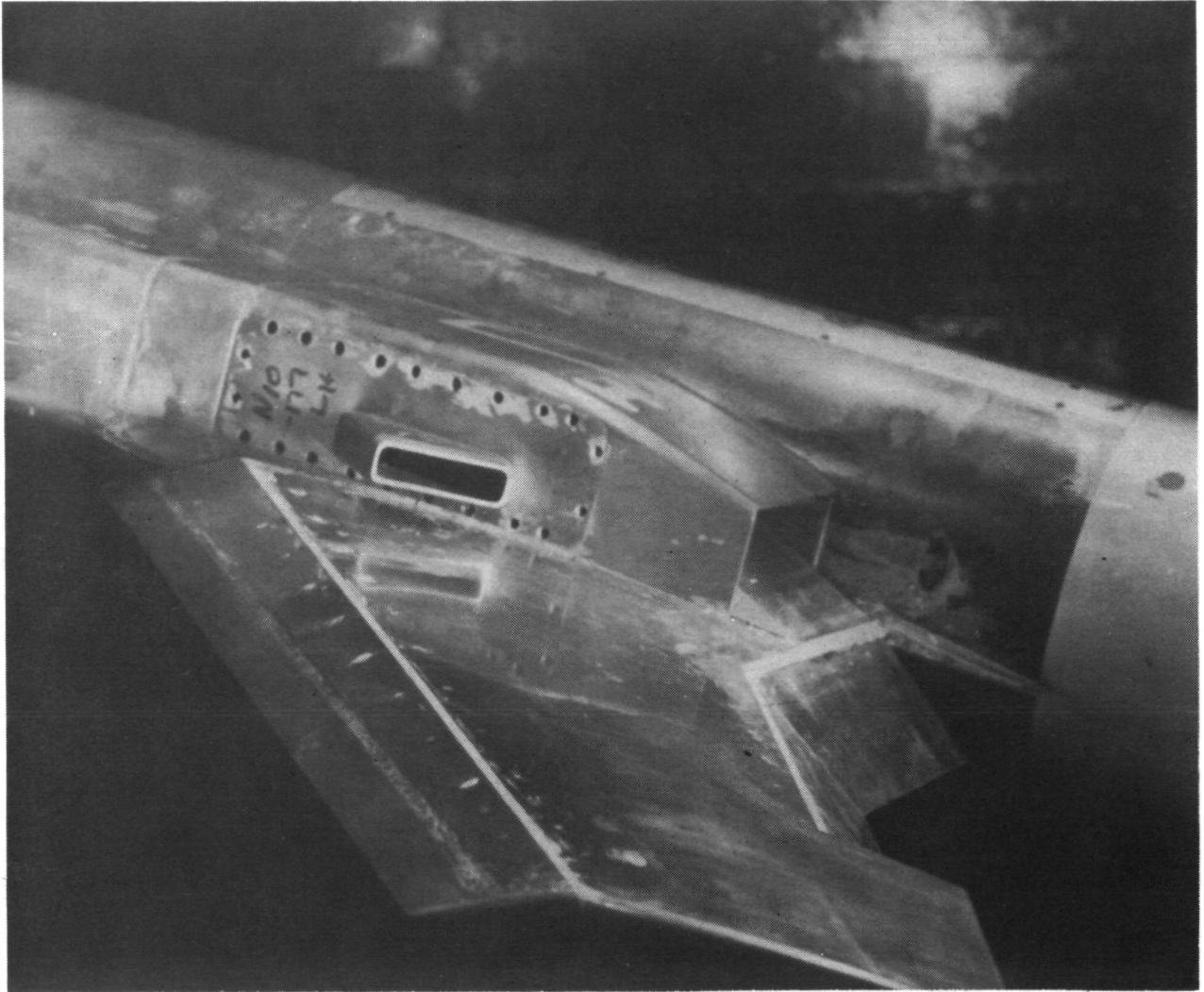
Figure 2.- Photographs of model.



L-78-47

(b) Spanwise nozzle Conf 10; 6.45 cm^2 round, convergent, $x_n/c_r = 0.527$,
 $h_n/c_r = 0.0935$.

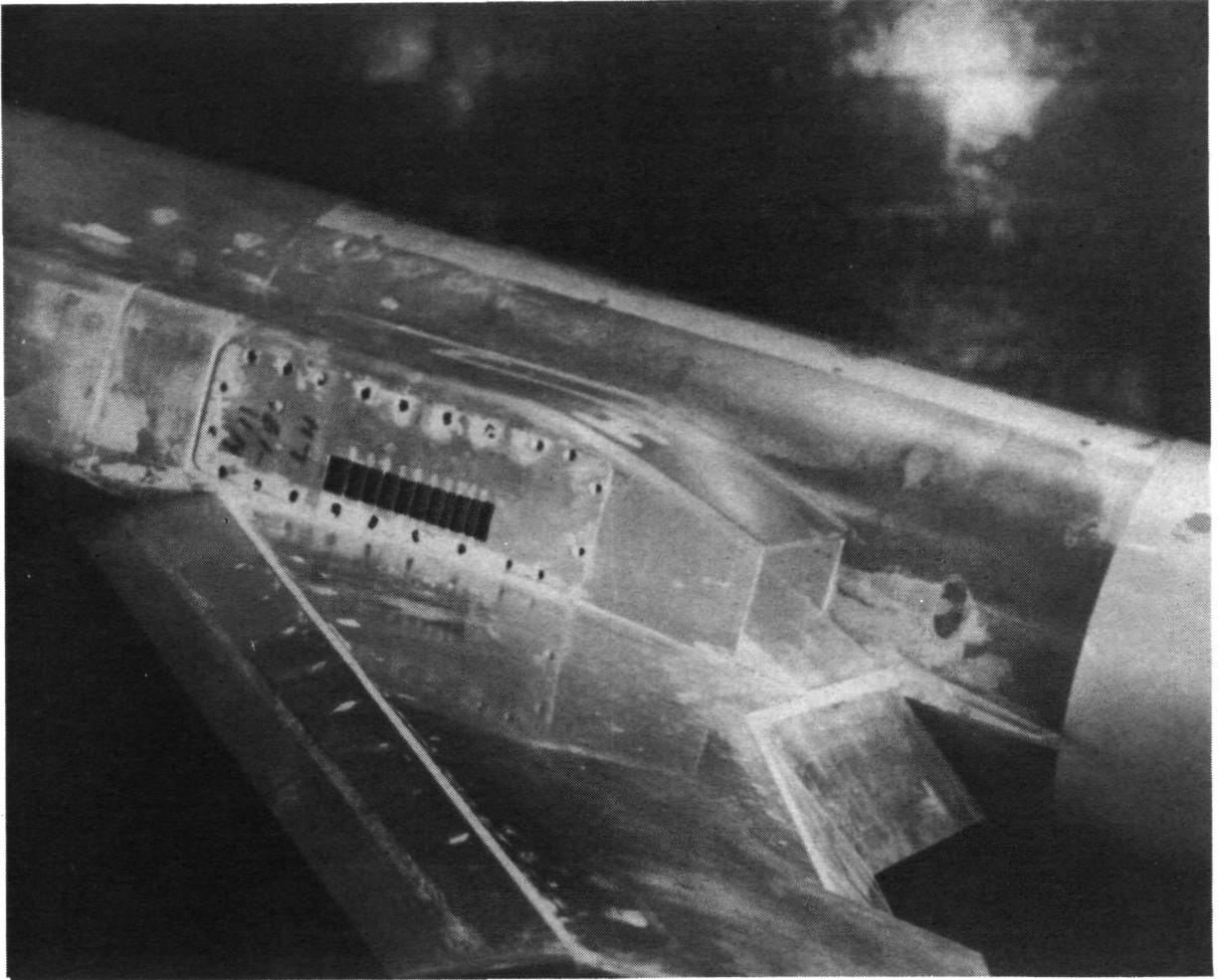
Figure 2.- Continued.



L-78-48

(c) Spanwise nozzle Conf 13; 6.74 cm^2 rectangular, convergent,
 $x_n/c_r = 0.532$, $h_n/c_r = 0.068$.

Figure 2.- Continued.



L-78-49

(d) Spanwise nozzle Conf 14; 6.94 cm^2 rectangular flush, convergent,
 $x_n/c_r = 0.493$, $h_n/c_r = 0.068$.

Figure 2.- Concluded.

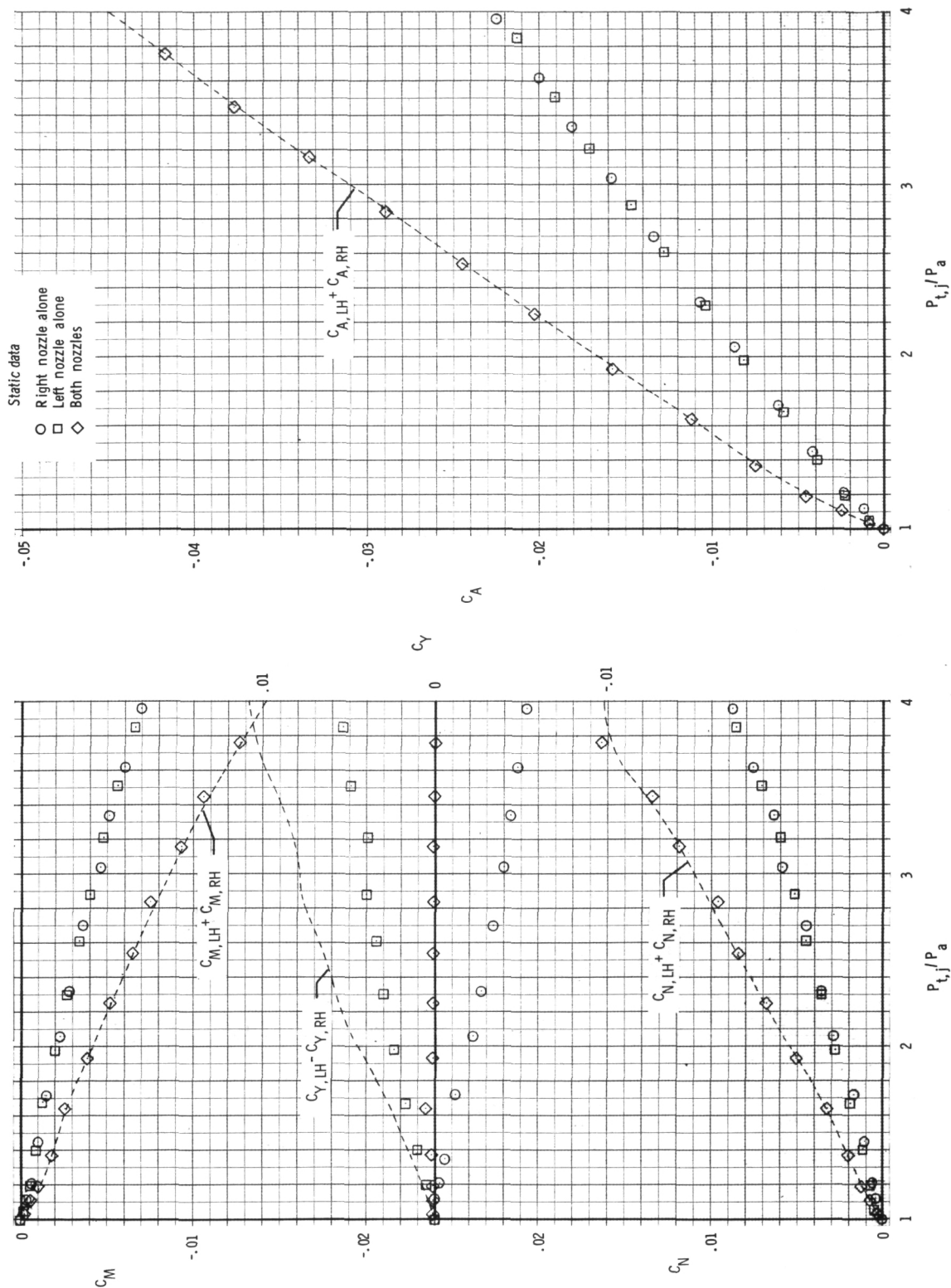
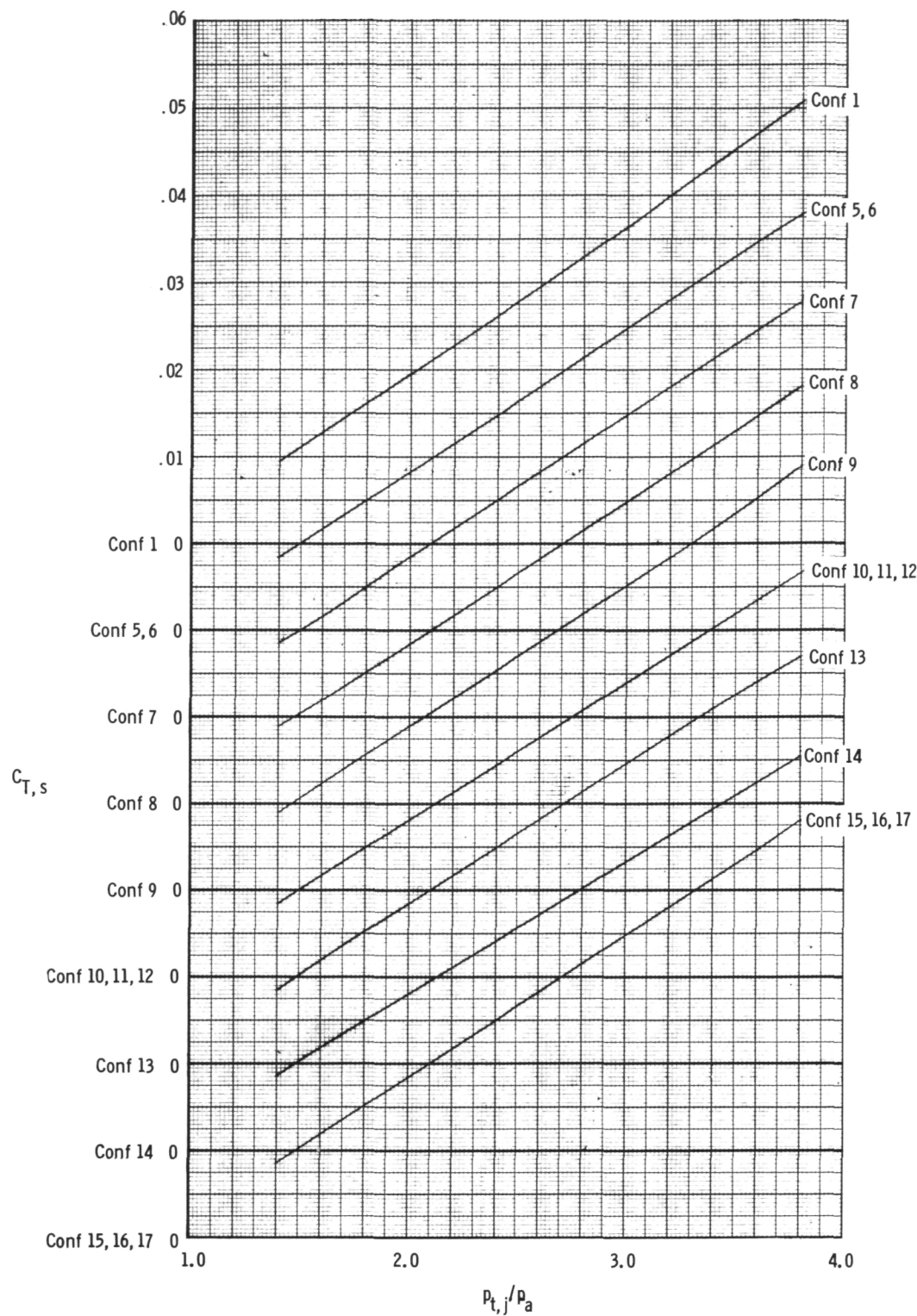
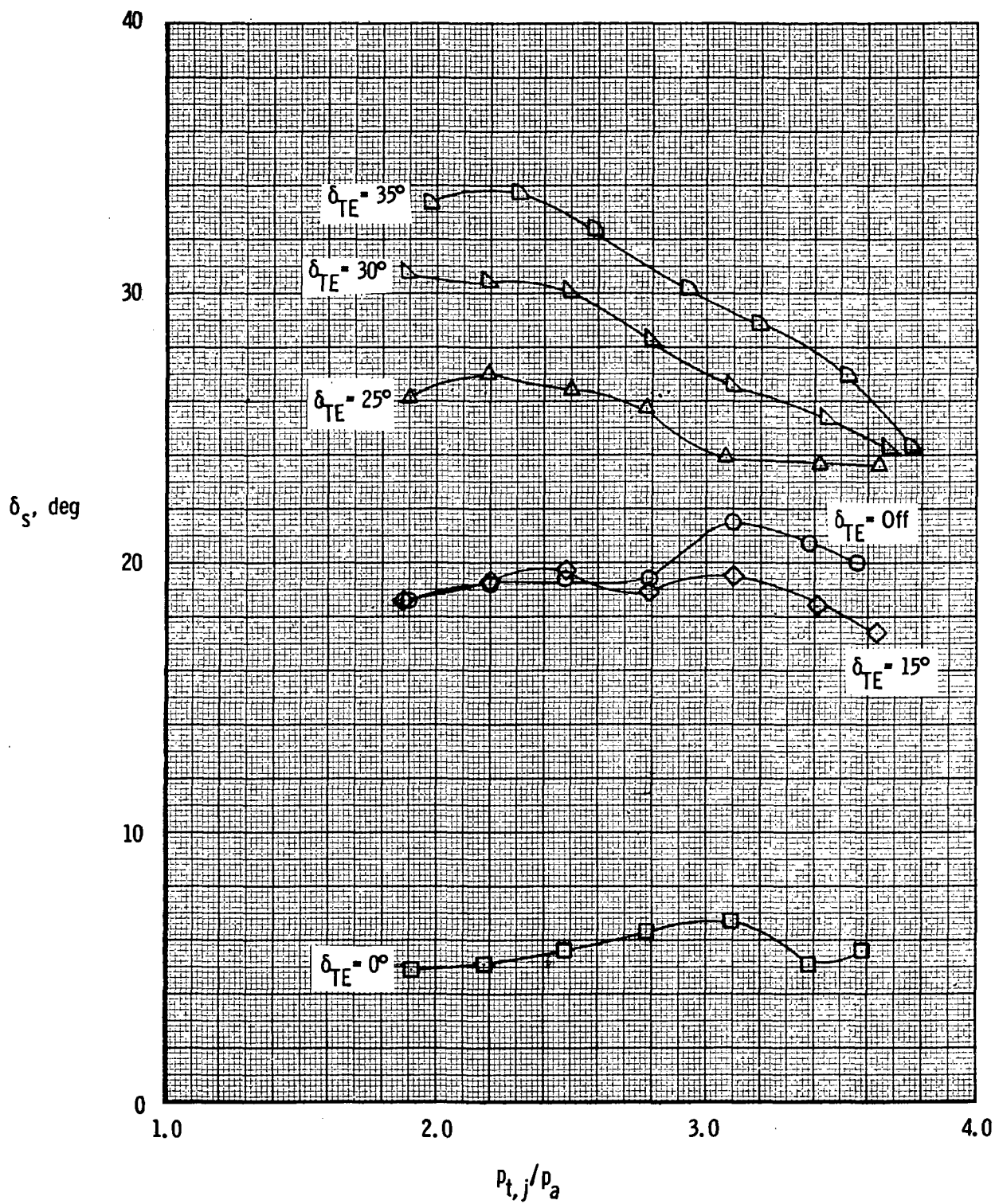


Figure 3.- Force and moment component breakdown of static data for 6.49 cm² round, convergent, $x_N/c_r = 0.527$, $h_N/c_r = 0.0935$, spanwise nozzle (Conf 10).



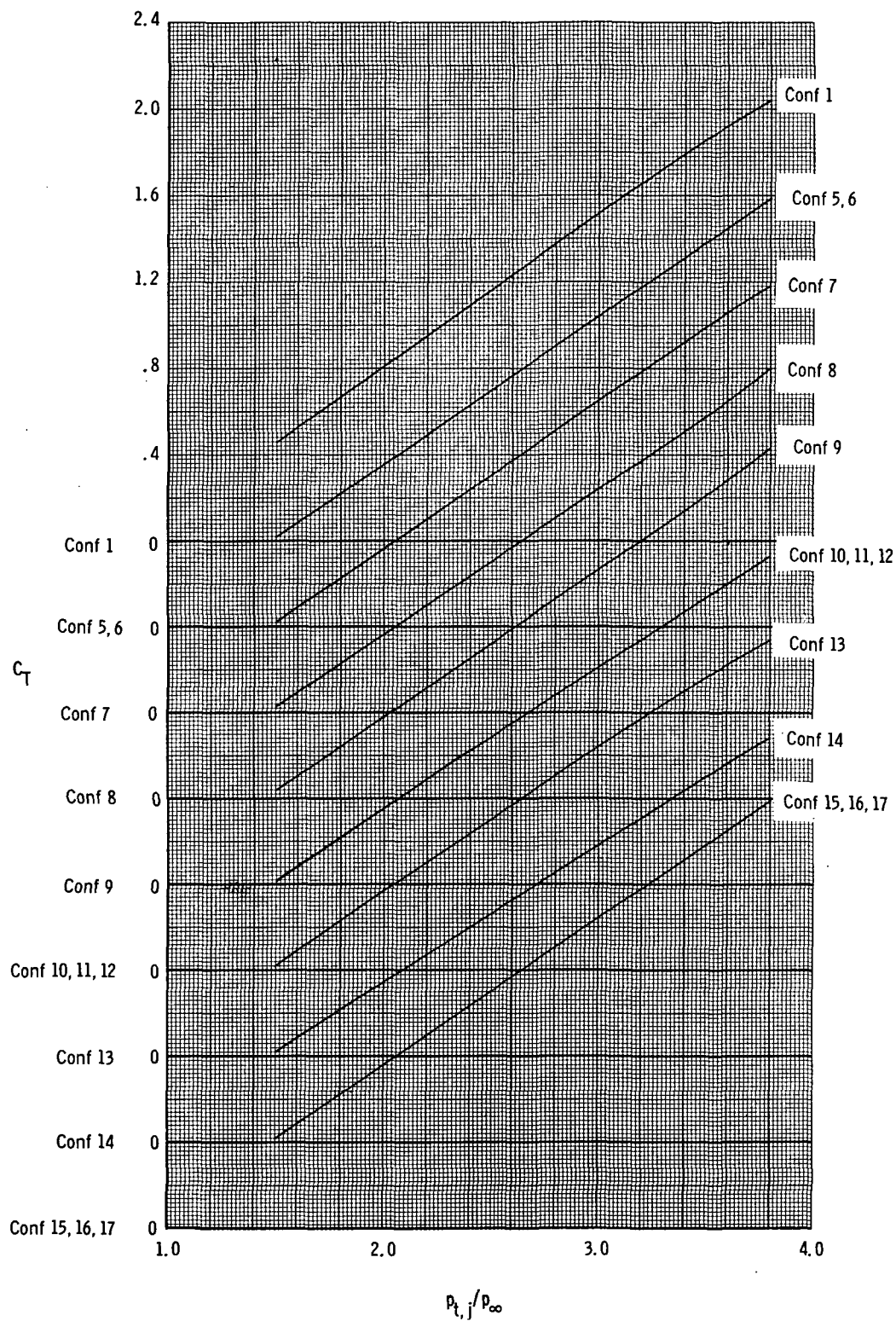
(a) Static thrust coefficient at $M = 0$.

Figure 4.- Thrust characteristics as a function of nozzle pressure ratio, $p_{t,j}/p_\infty$ ($p_{t,j}/p_a$ for $M = 0$).



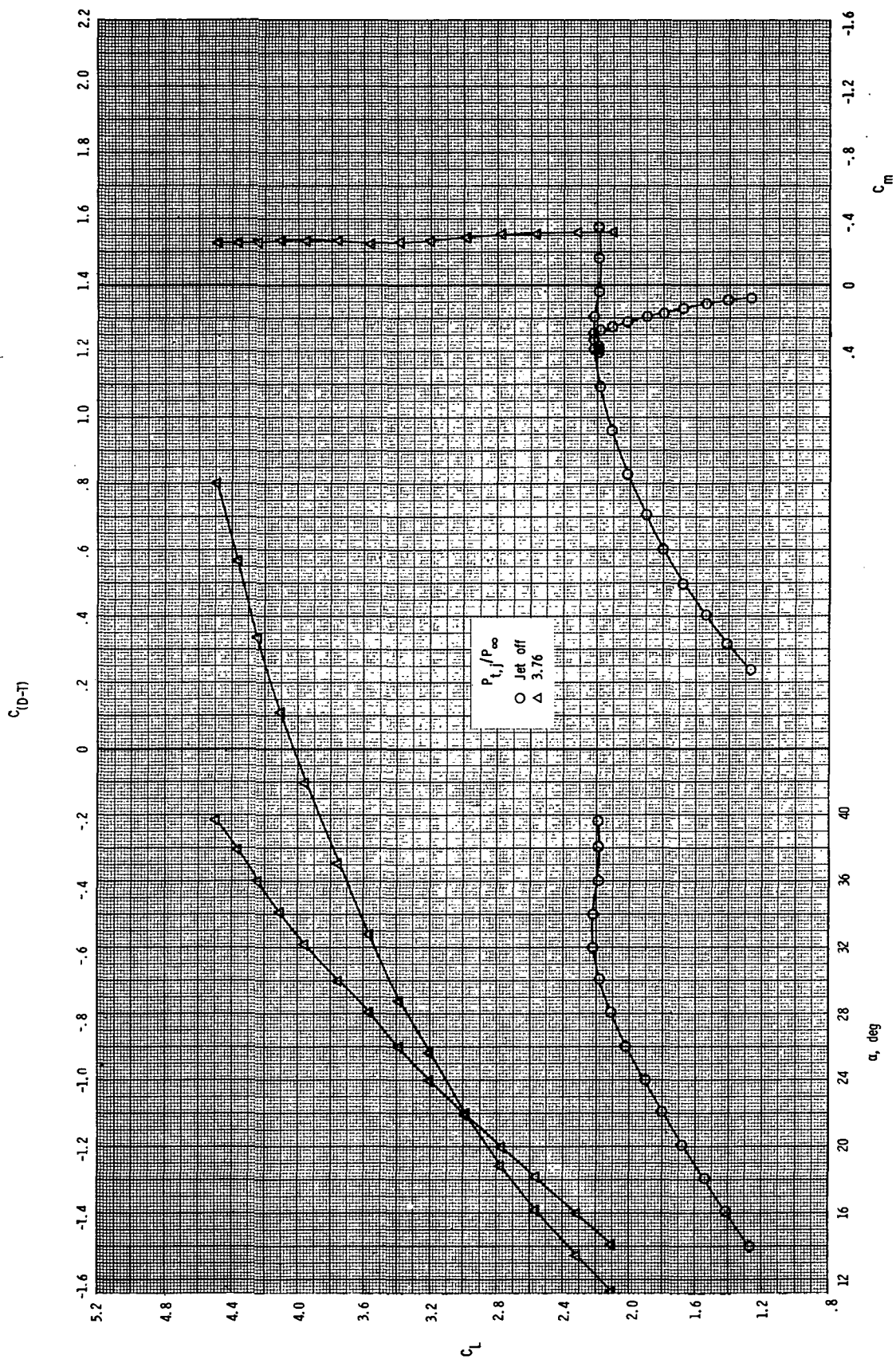
(b) Static turning for baseline nozzle, Conf 1.

Figure 4.- Continued.



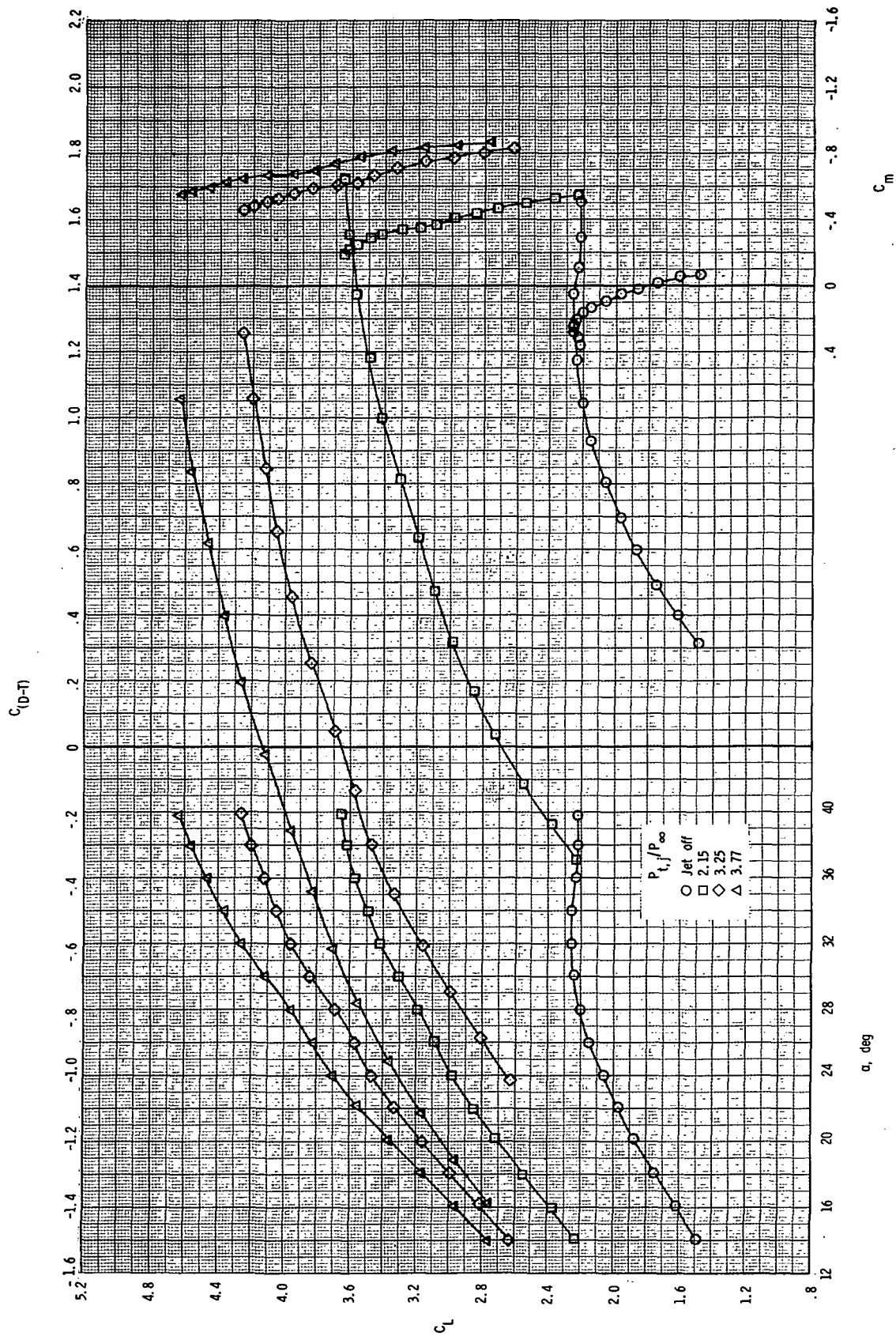
(c) Thrust coefficient at $M = 0.186$. $C_T = C_{T,s}(p_{\infty}/q_{\infty})$.

Figure 4.- Concluded.



(a) $\delta_{TE} = 0^\circ$.

Figure 5.- Basic longitudinal aerodynamic characteristics at $M = 0.186$ for baseline nozzle (no spanwise blowing) Conf 1; $\delta_{LE} = \delta_C = 0$; H_2 canard.



(b) $\delta_{TE} = 15^\circ$.

Figure 5.- Concluded.

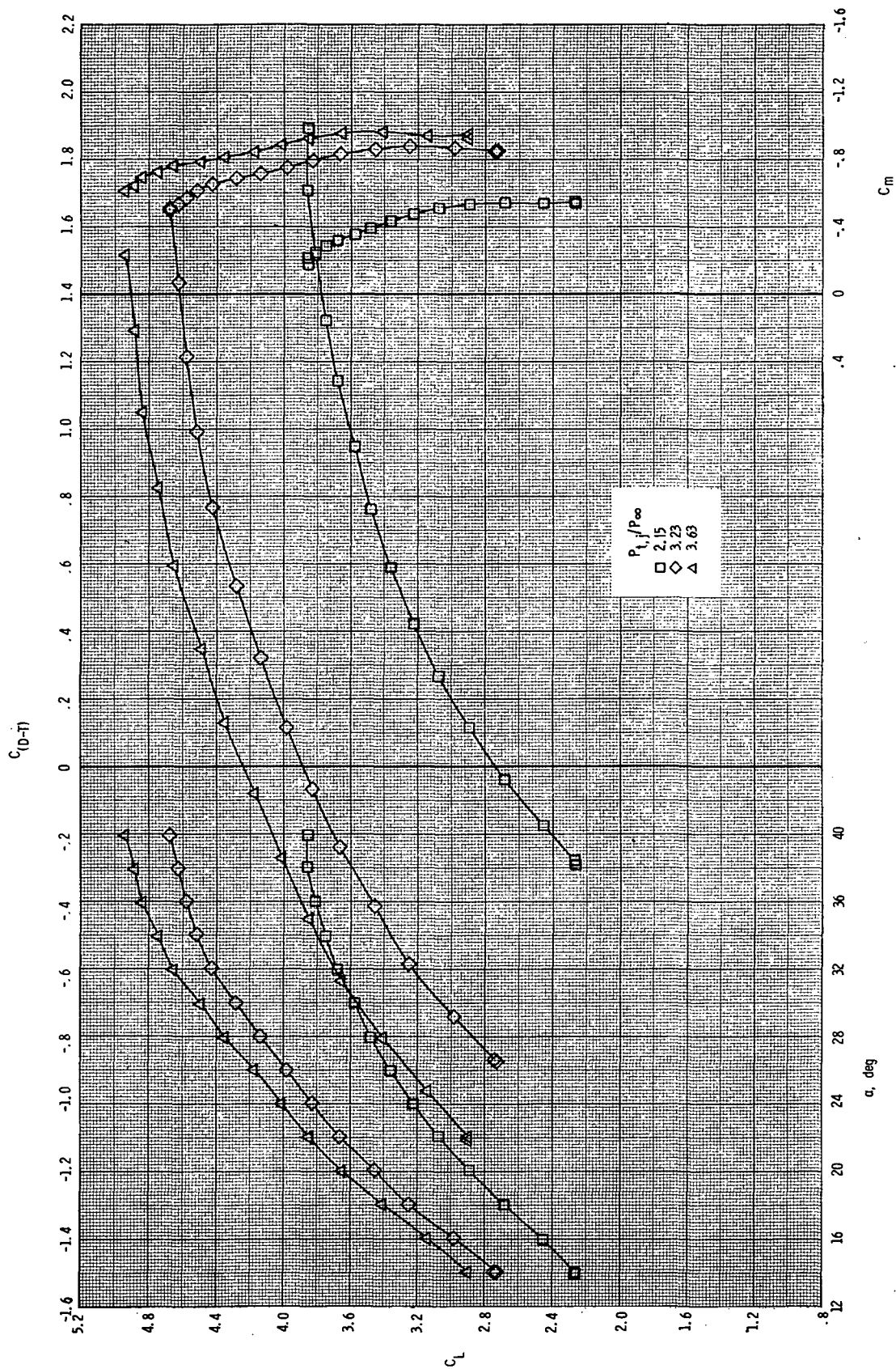


Figure 6.- Basic longitudinal aerodynamic characteristics at $M = 0.186$ for spanwise nozzle Conf 5 (3.25 cm² round, convergent, $x_n/c_r = 0.527$, $h_n/c_r = 0.0935$); $\delta_{TE} = 15^\circ$, $\delta_{LE} = \delta_C = 0^\circ$, H_2 canard.

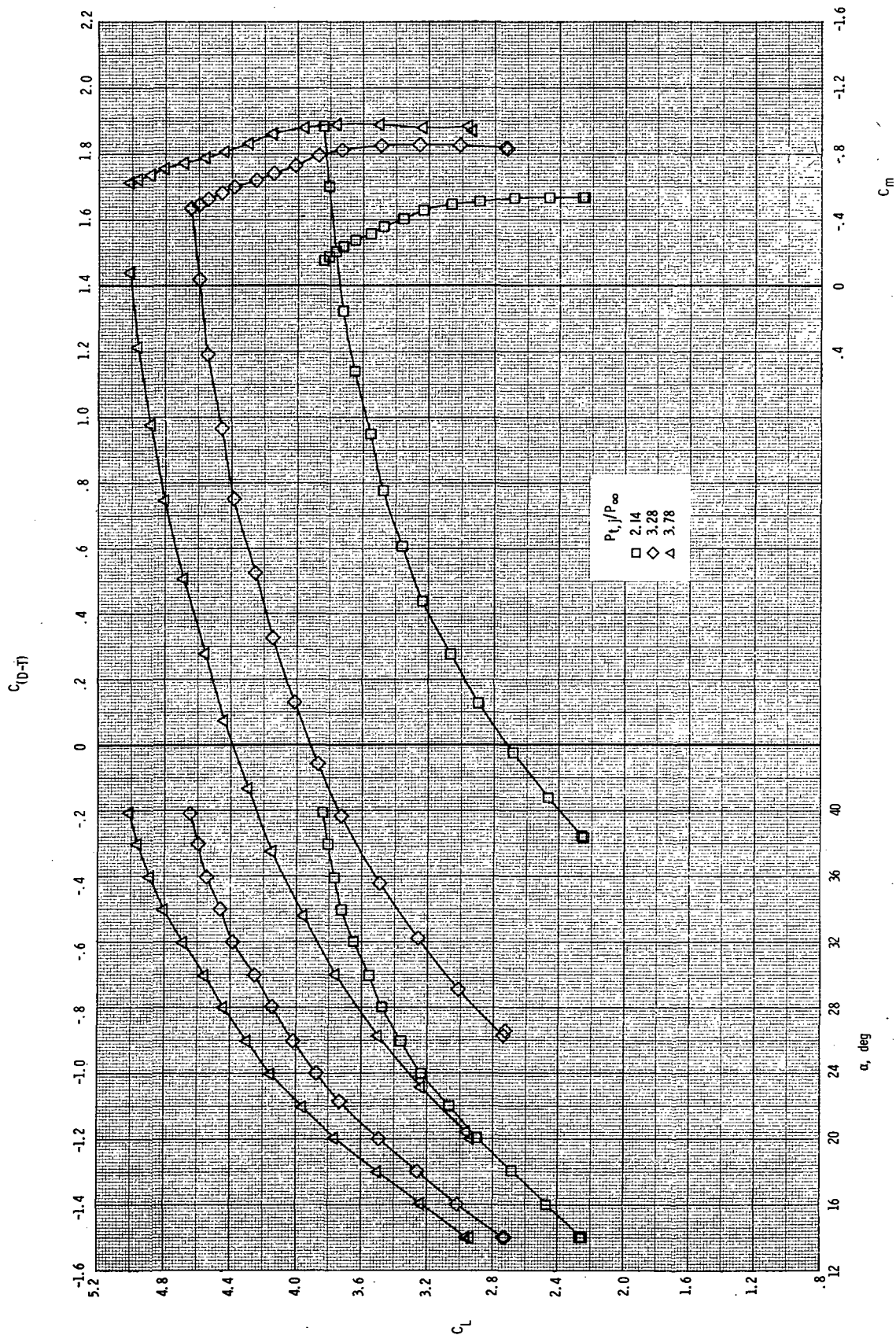


Figure 7.- Basic longitudinal aerodynamic characteristics at $M = 0.186$ for spanwise nozzle Conf 6 (3.25 cm² round, convergent, $x_n/c_r = 0.416$, $h_n/c_r = 0.0935$); $\delta_{TE} = 15^\circ$, $\delta_{LE} = \delta_C = 0^\circ$, H₂ canard.

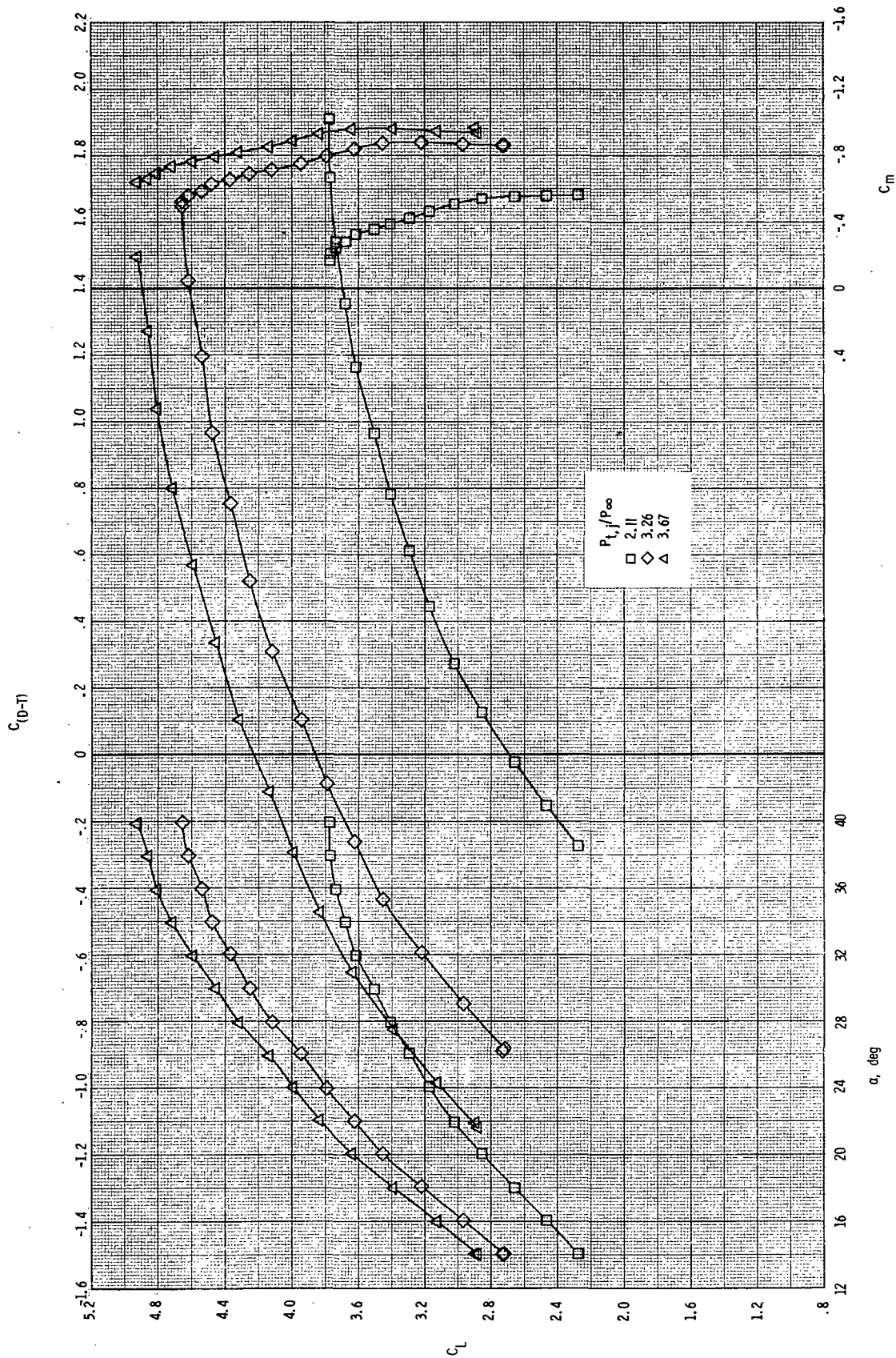


Figure 8.- Basic longitudinal aerodynamic characteristics at $M = 0.186$ for spanwise nozzle Conf 7 (3.25 cm² round, convergent, $x_n/c_r = 0.622$, $h_n/c_r = 0.0935$; $\delta_{TE} = 15^\circ$, $\delta_{LE} = \delta_C = 0^\circ$, H₂ canard.

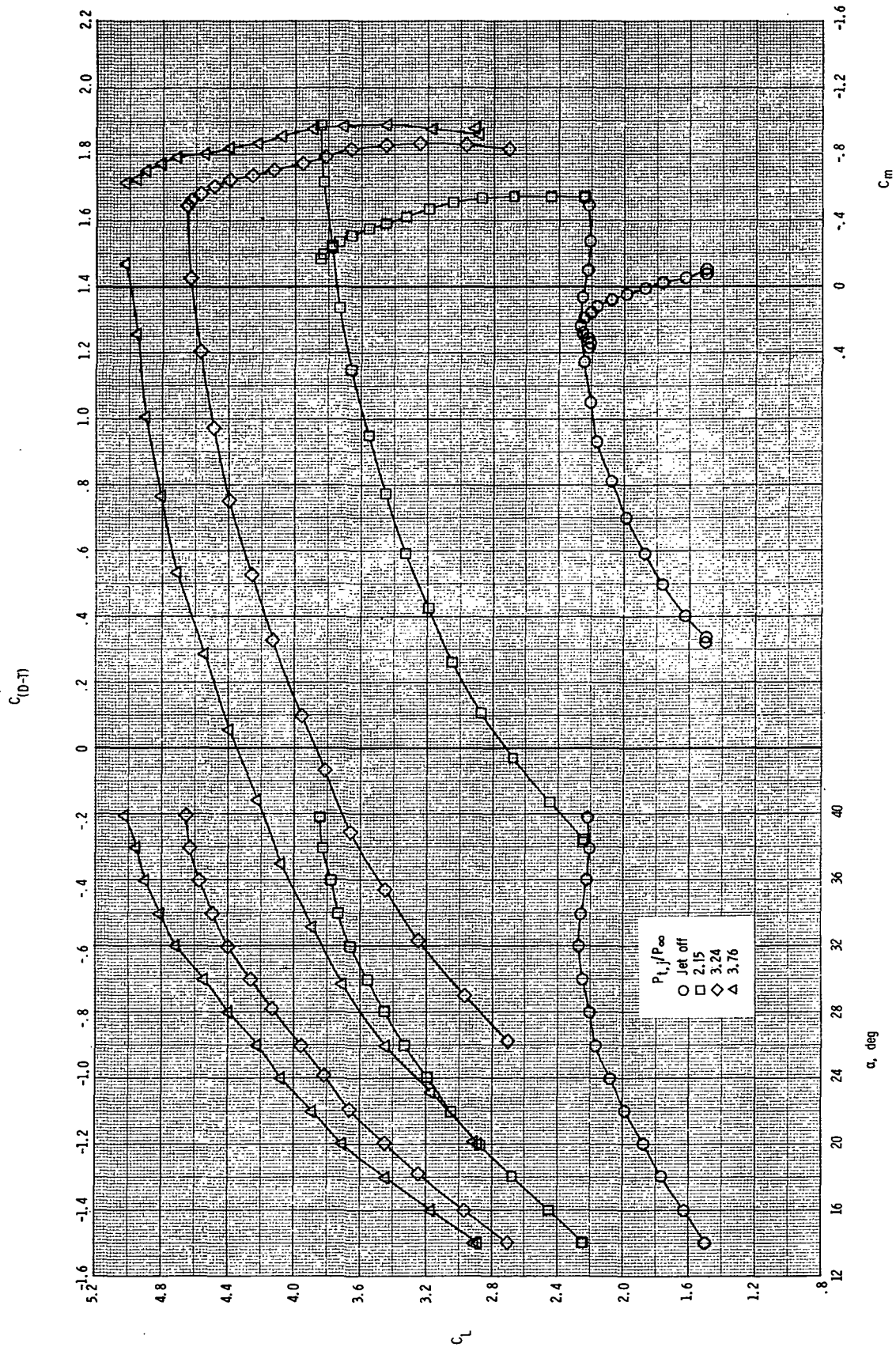


Figure 9.- Basic longitudinal aerodynamic characteristics at $M = 0.186$ for spanwise nozzle Conf 8 (3.22 cm^2 round, convergent, $x_n/c_r = 0.527$, $h_n/c_r = 0.0793$); $\delta_{TE} = 15^\circ$, $\delta_{LE} = \delta_c = 0^\circ$, H_2 canard.

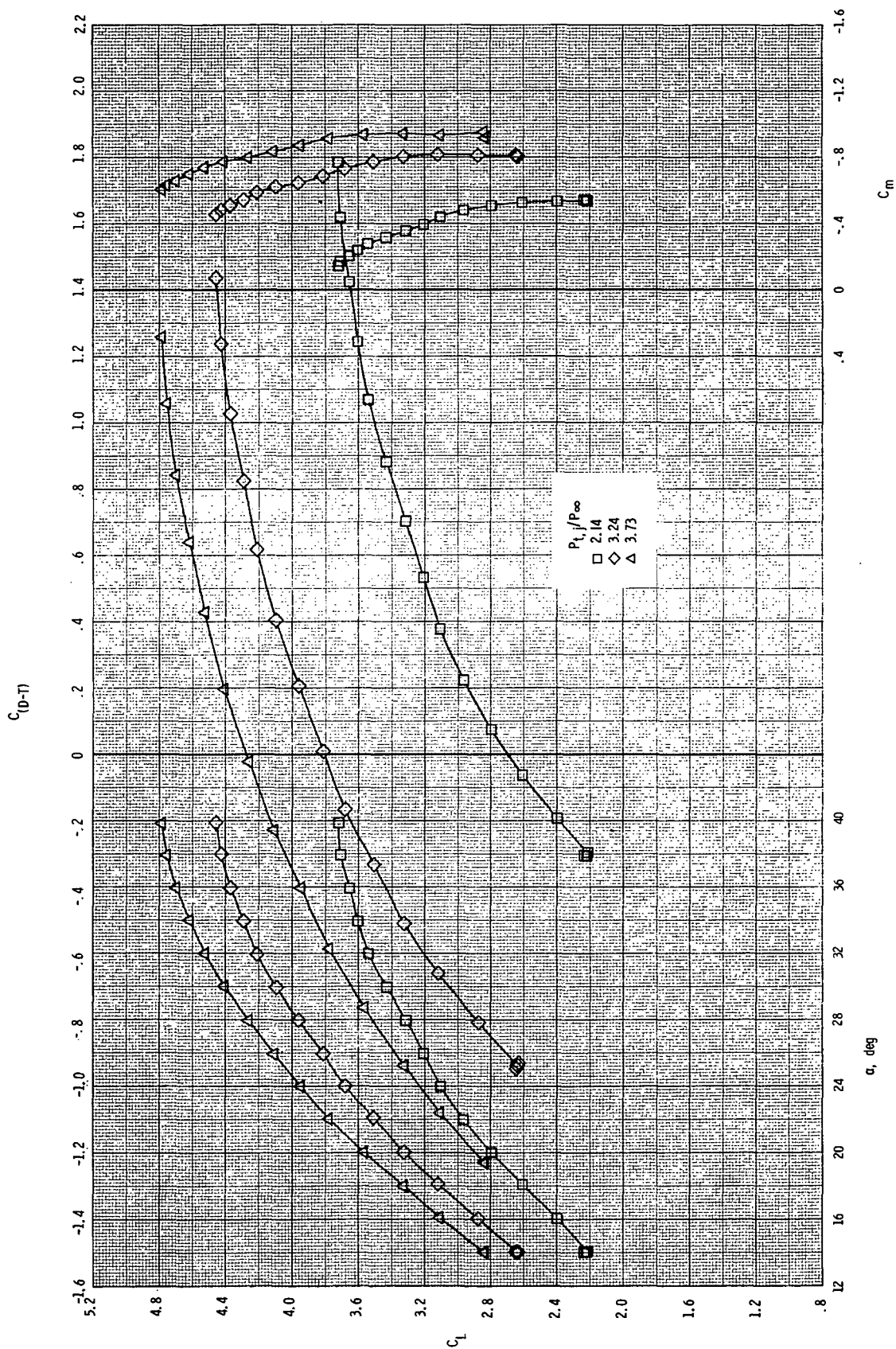
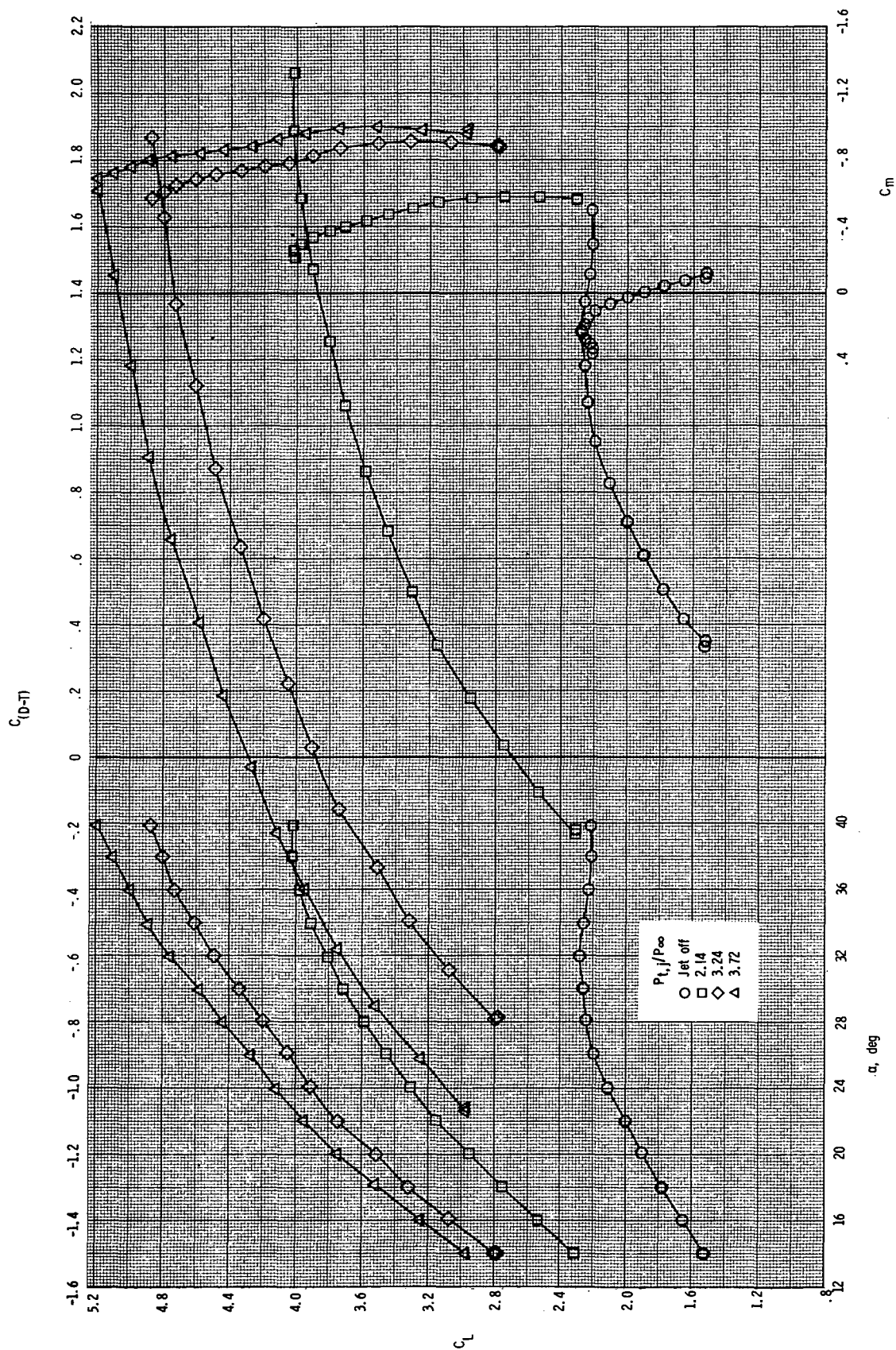
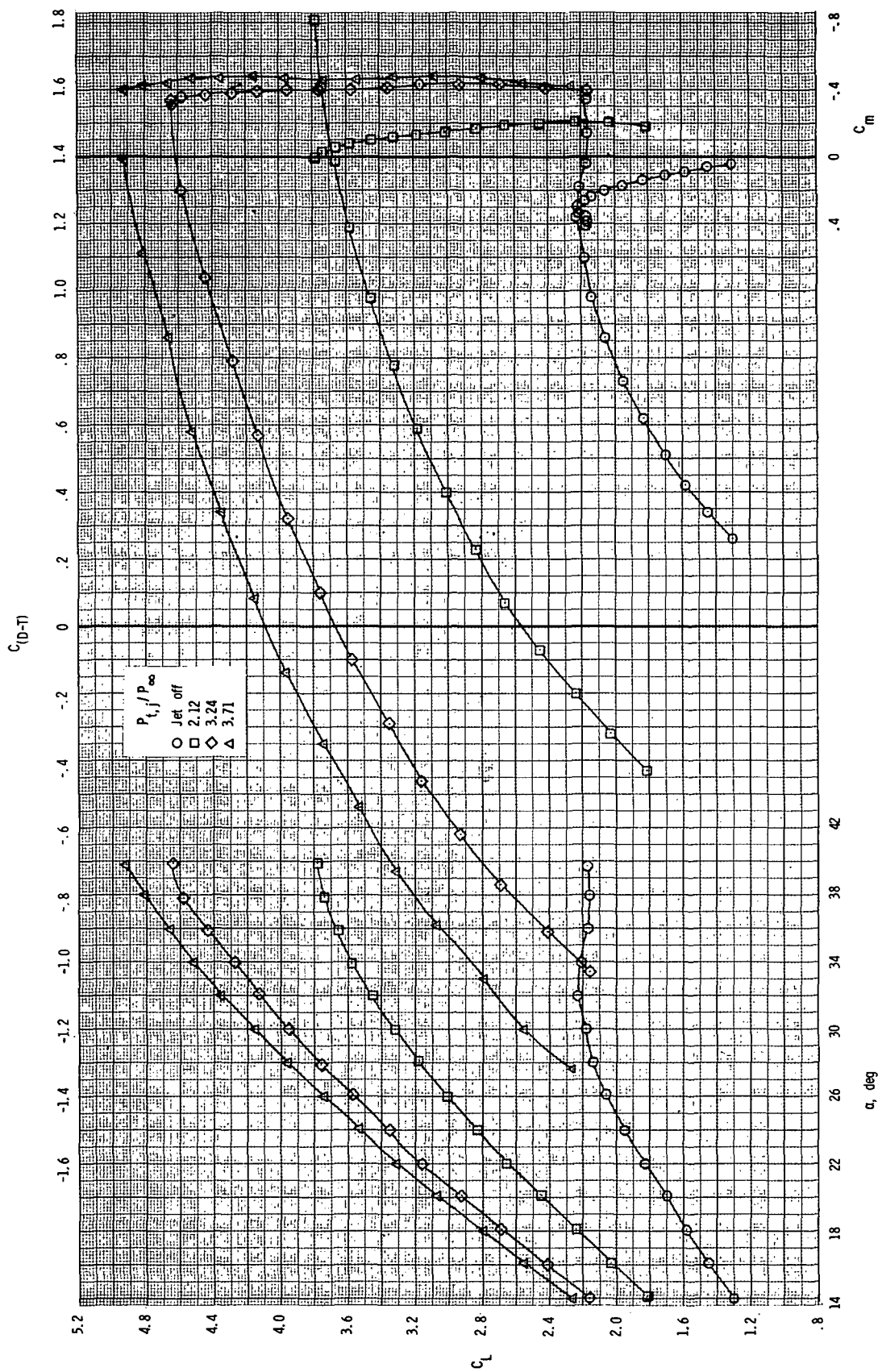


Figure 10.- Basic longitudinal aerodynamic characteristics at $M = 0.186$ for spanwise nozzle Conf 9 (1.60 cm² round, convergent, $x_n/c_r = 0.527$, $h_n/c_r = 0.0793$); $\delta_{TE} = 15^\circ$, $\delta_{LE} = \delta_C = 0^\circ$, H₂ canard.



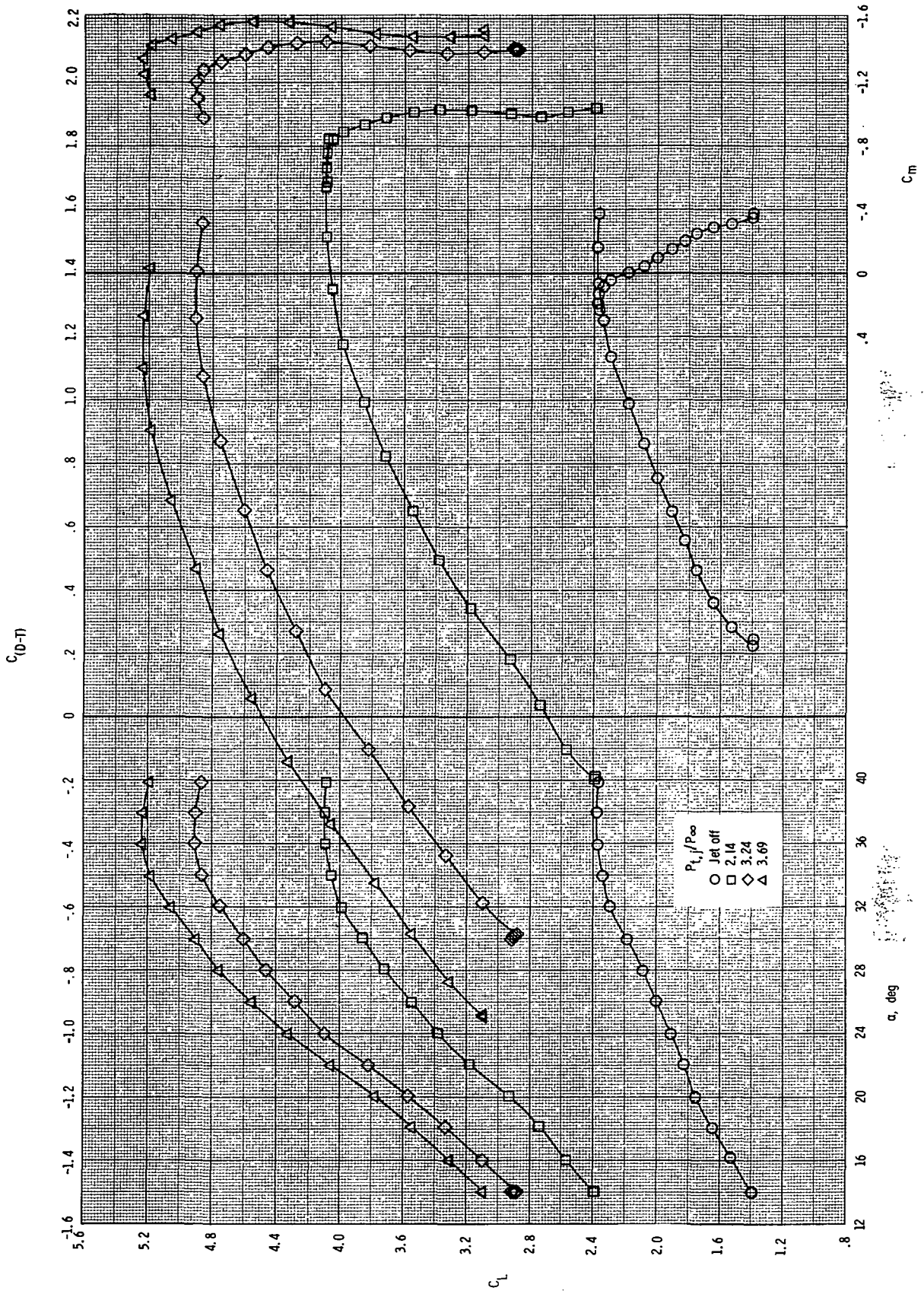
(a) $\delta_{TE} = 15^\circ$, $\delta_{TE} = \delta_C = 0^\circ$, H_2 canard.

Figure 11.- Basic longitudinal aerodynamic characteristics at $M = 0.186$ for spanwise nozzle Conf 10 (6.49 cm² round, convergent, $x_n/c_r = 0.527$, $h_n/c_r = 0.0935$).



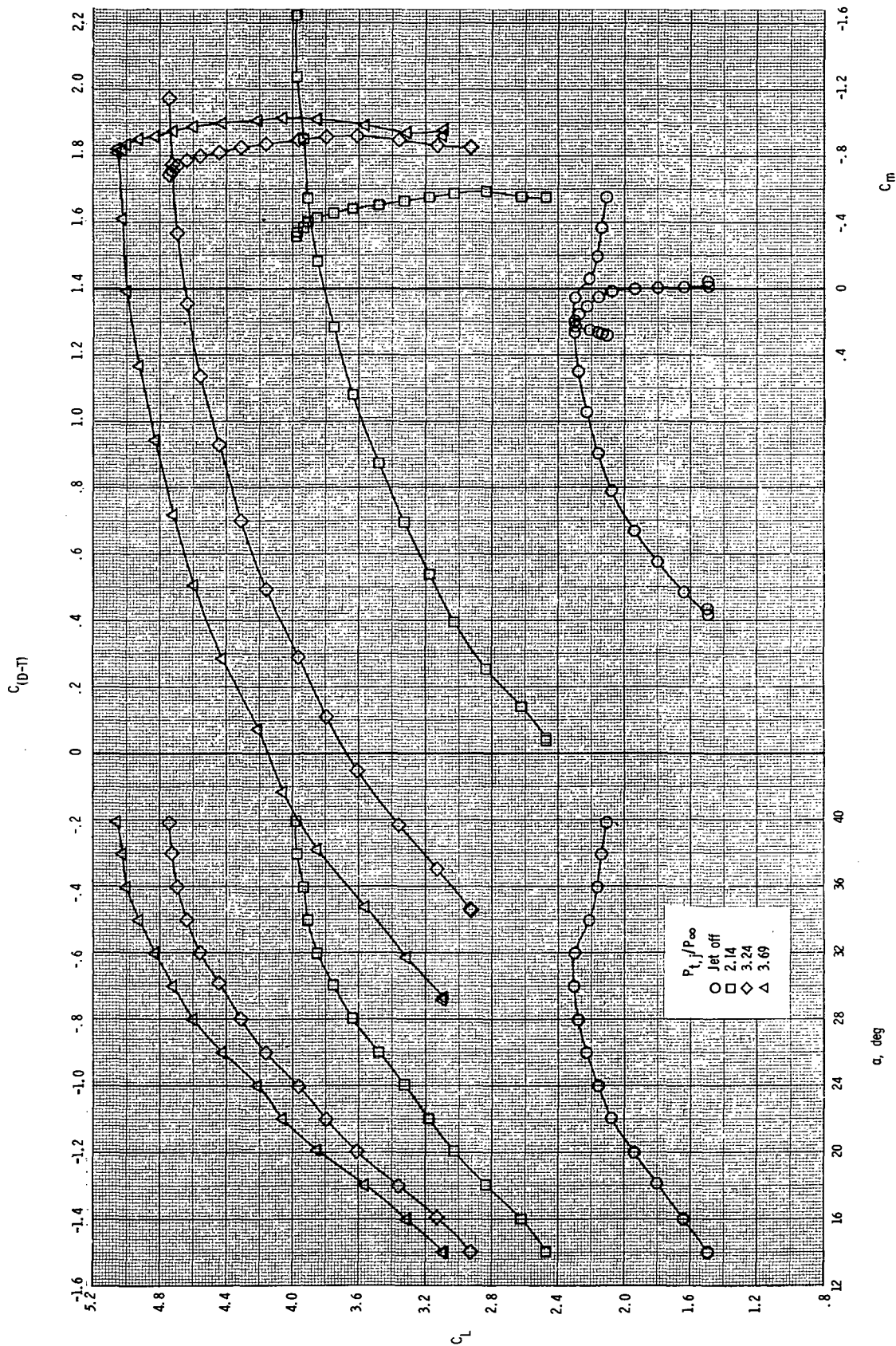
(b) $\delta_{TE} = \delta_{LE} = \delta_C = 0^\circ$, H_2 canard.

Figure 11.- Continued.



(c) $\delta_{TE} = 30^\circ$, $\delta_{LE} = 20^\circ$, $\delta_C = -20^\circ$, H_3 canard.

Figure 11.- Continued.



(d) $\delta_{TE} = 30^\circ$, $\delta_{LE} = 20^\circ$, $\delta_C = 20^\circ$, H₃ canard.

Figure 11.- Concluded.

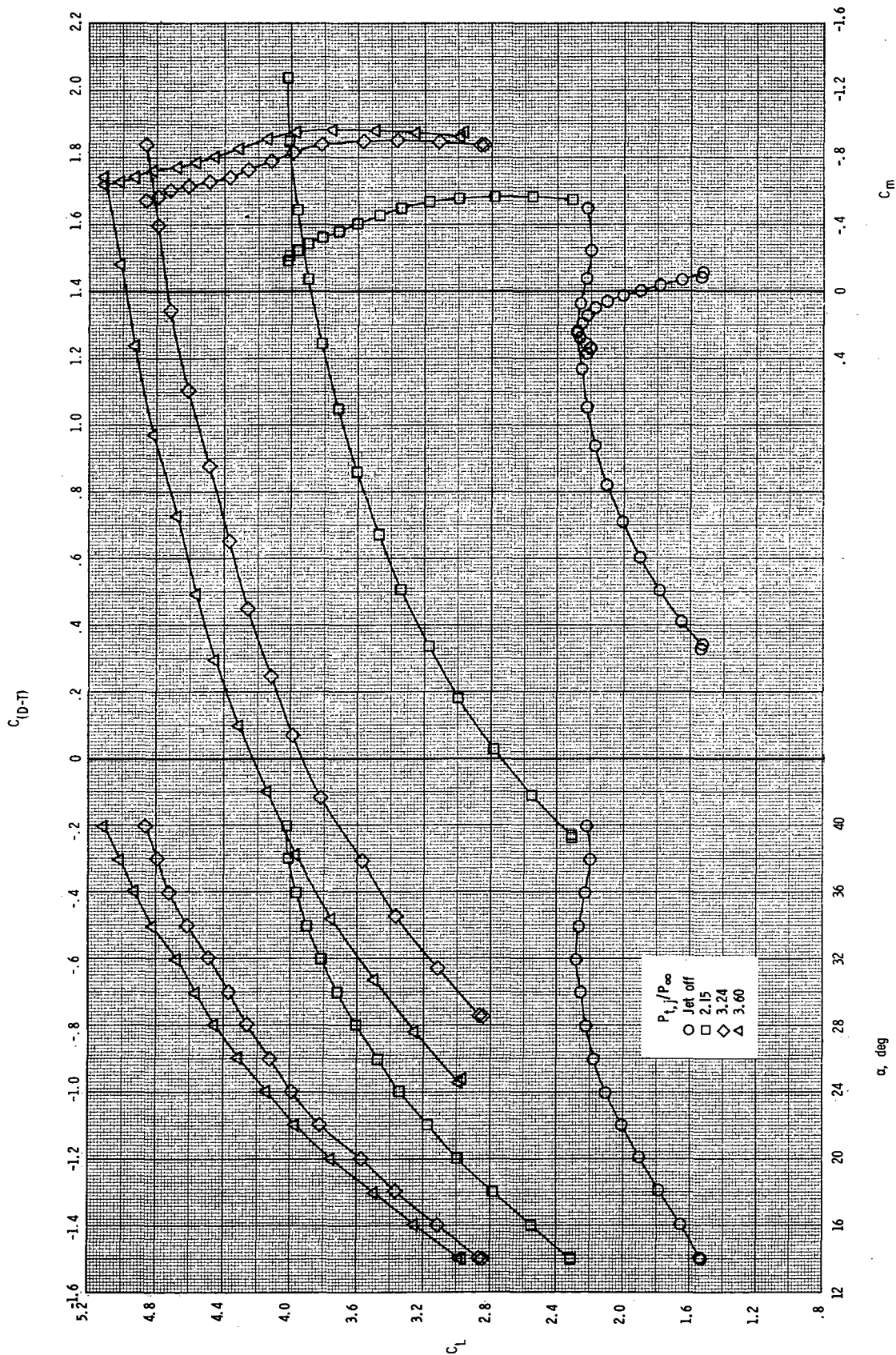


Figure 12.- Basic longitudinal aerodynamic characteristics at $M = 0.186$ for spanwise nozzle Conf 11 (6.49 cm² round, convergent, $x_n/c_r = 0.416$, $h_n/c_r = 0.0935$); $\delta_{TE} = 150^\circ$, $\delta_{LE} = \delta_C = 0^\circ$, H₂ canard.

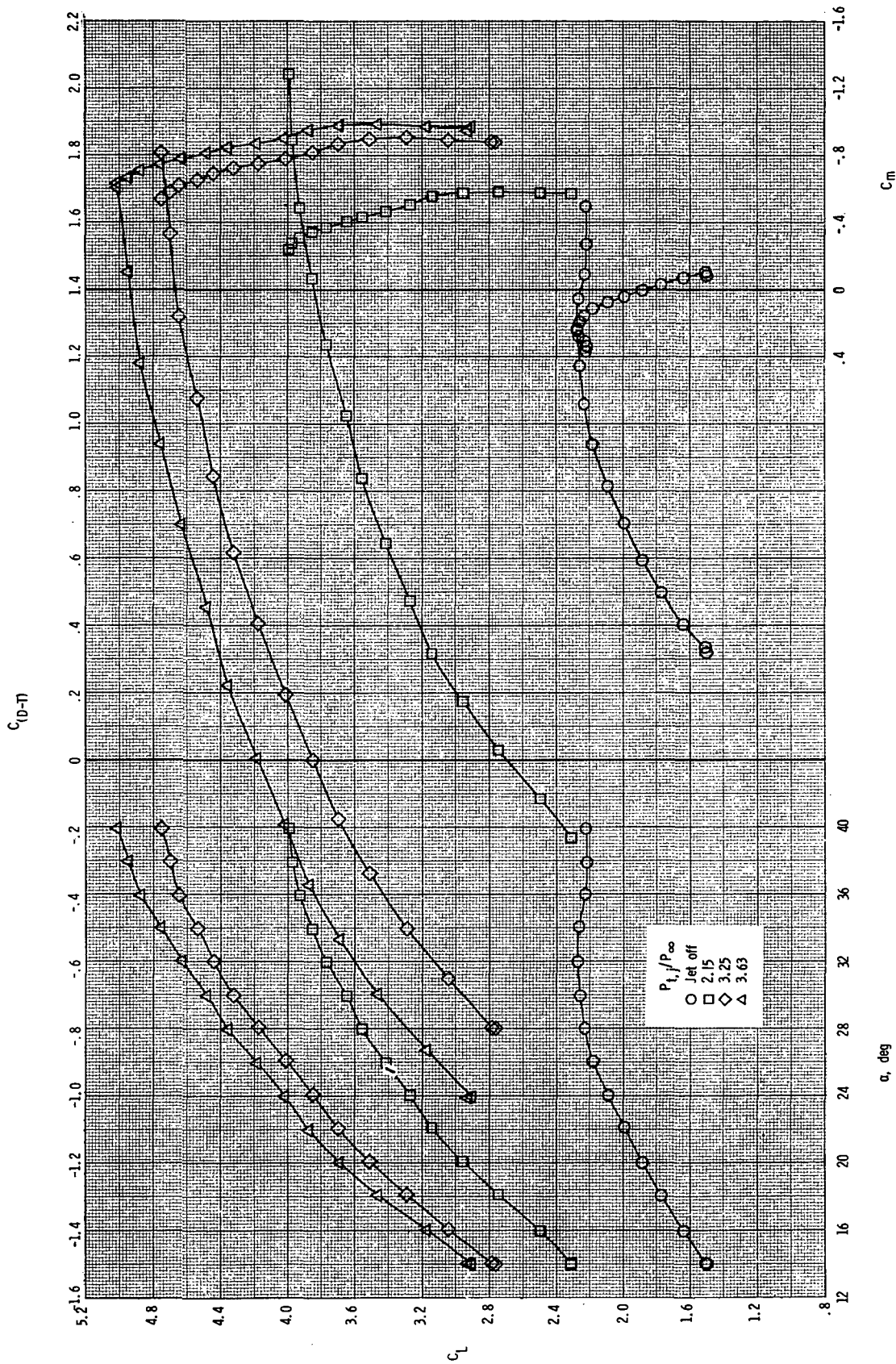


Figure 13.- Basic longitudinal aerodynamic characteristics at $M = 0.186$ for spanwise nozzle Conf 12 (6.49 cm² round, convergent, $x_n/c_r = 0.622$, $h_n/c_r = 0.0935$); $\delta_{TE} = 15^\circ$, $\delta_{LE} = \delta_C = 0^\circ$, H_2 canard.

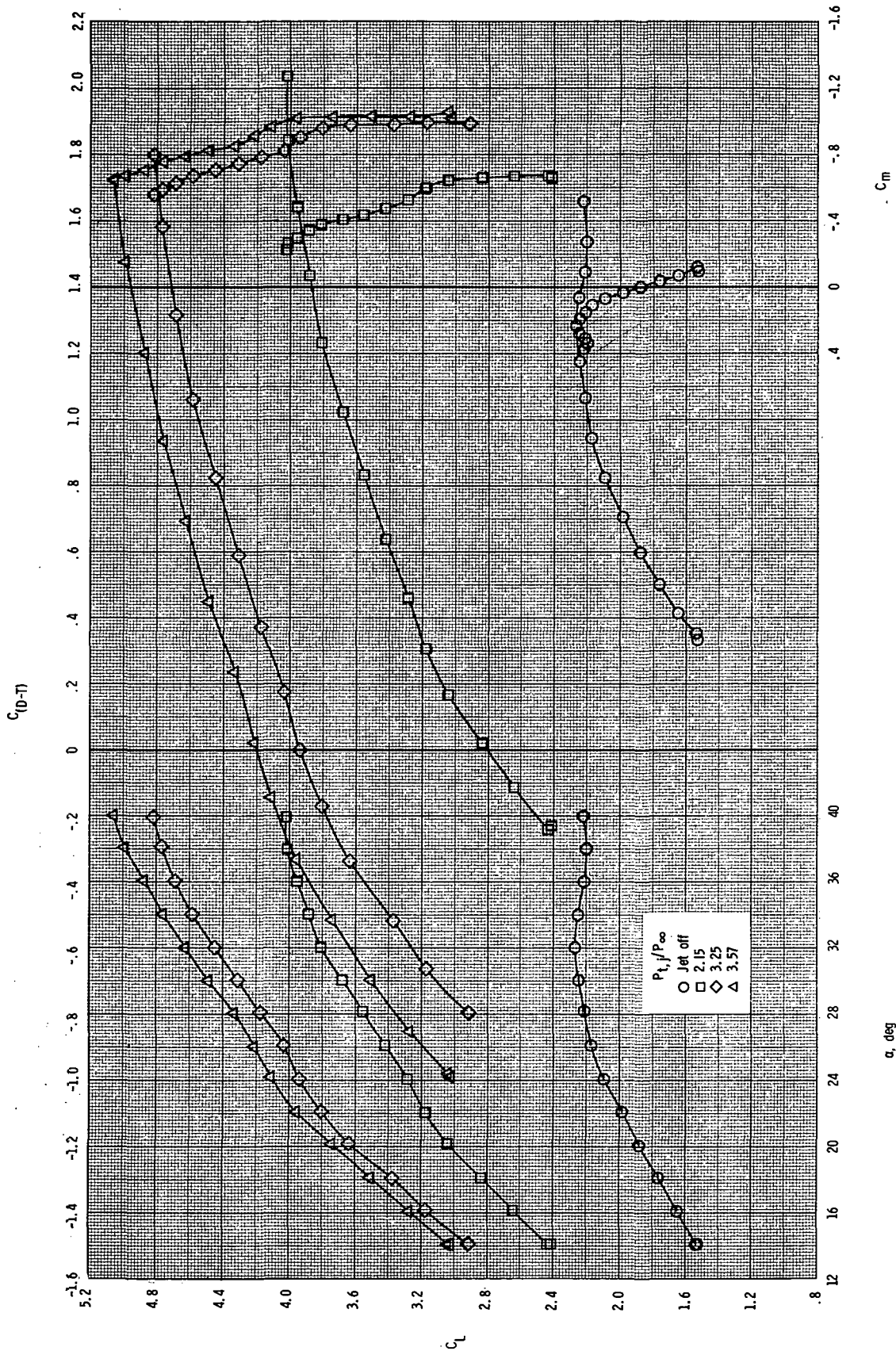
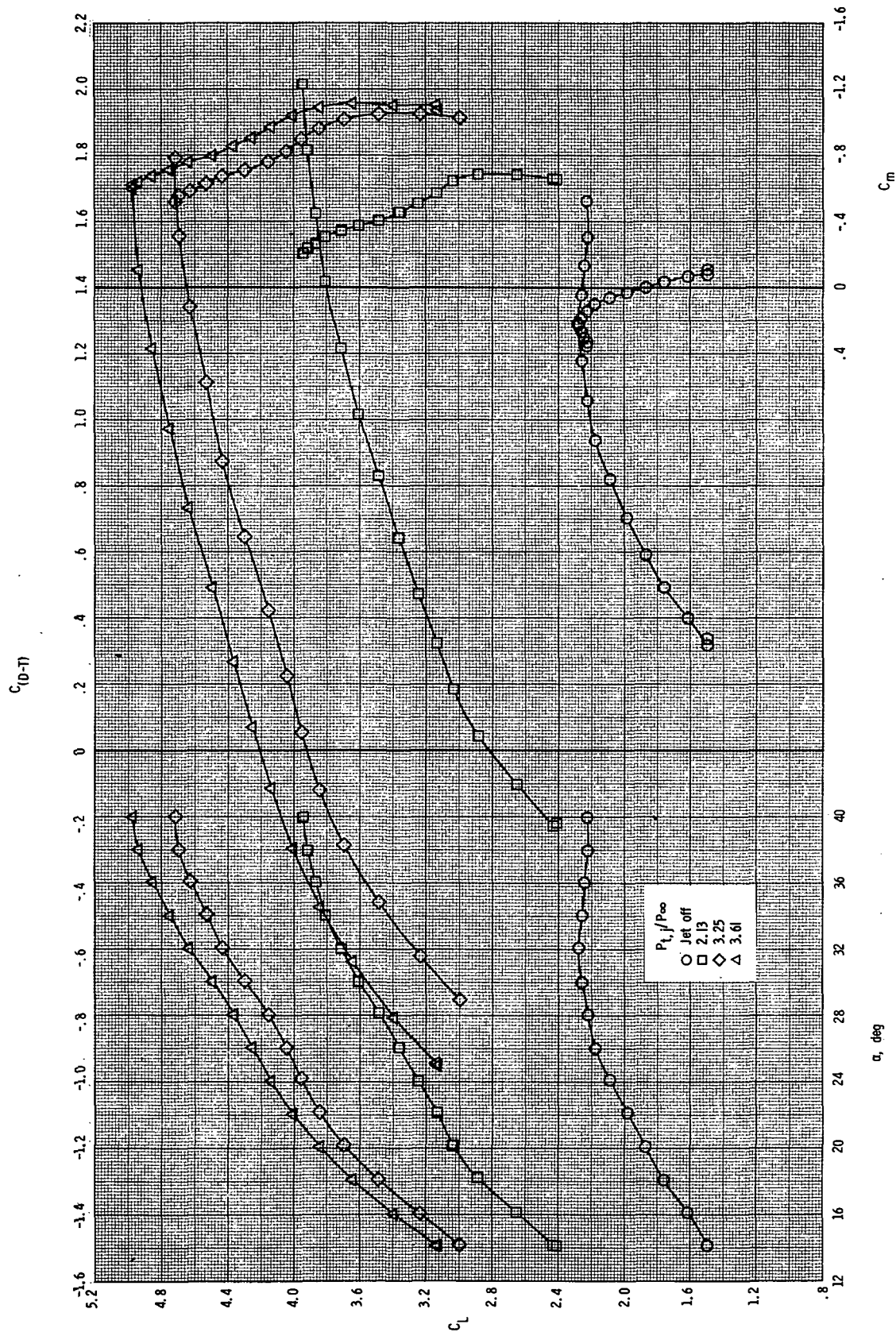
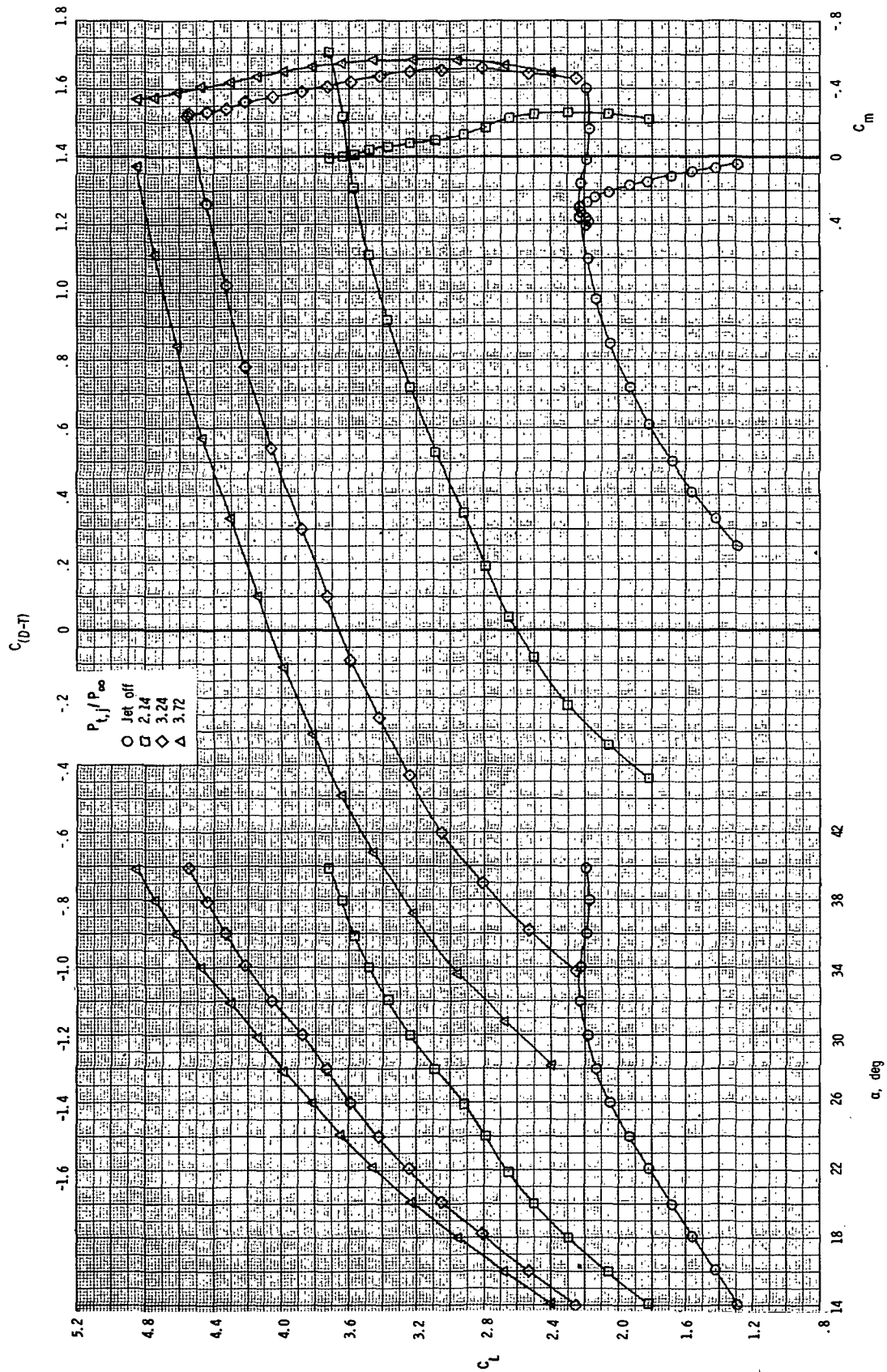


Figure 14.- Basic longitudinal aerodynamic characteristics at $M = 0.186$ for spanwise nozzle Conf 13 (6.74 cm² rectangular, convergent, $x_n/c_r = 0.532$, $h_n/c_r = 0.068$); $\delta_{TE} = 15^\circ$, $\delta_{LE} = \delta_C = 0^\circ$, H_2 canard.



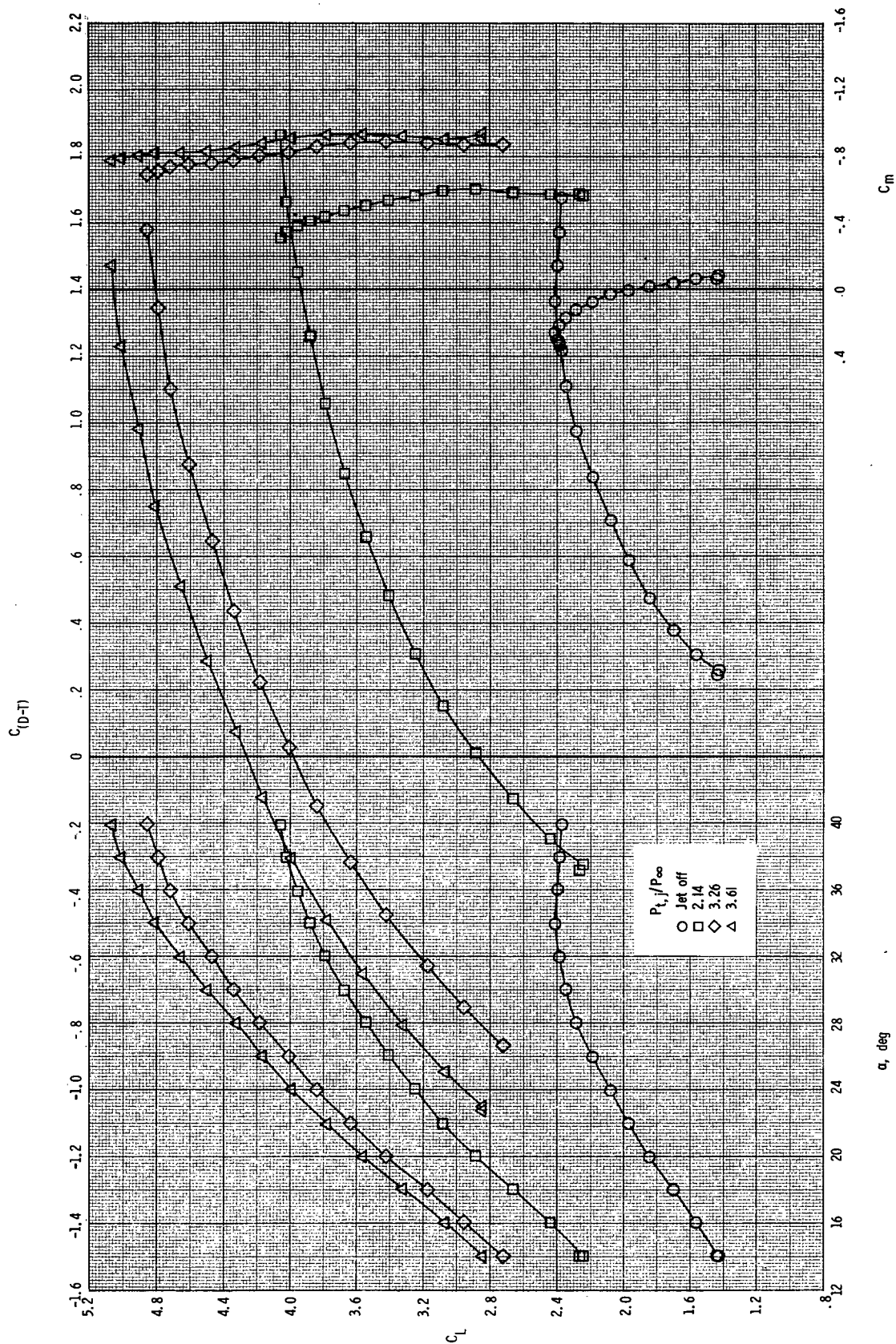
(a) $\delta_{TE} = 15^\circ$, $\delta_{LE} = \delta_C = 0^\circ$, H_2 canard.

Figure 15.- Basic longitudinal aerodynamic characteristics at $M = 0.186$ for spanwise nozzle Conf 14 (6.94 cm² rectangular flush, convergent, $x_n/c_r = 0.493$, $h_n/c_r = 0.068$).



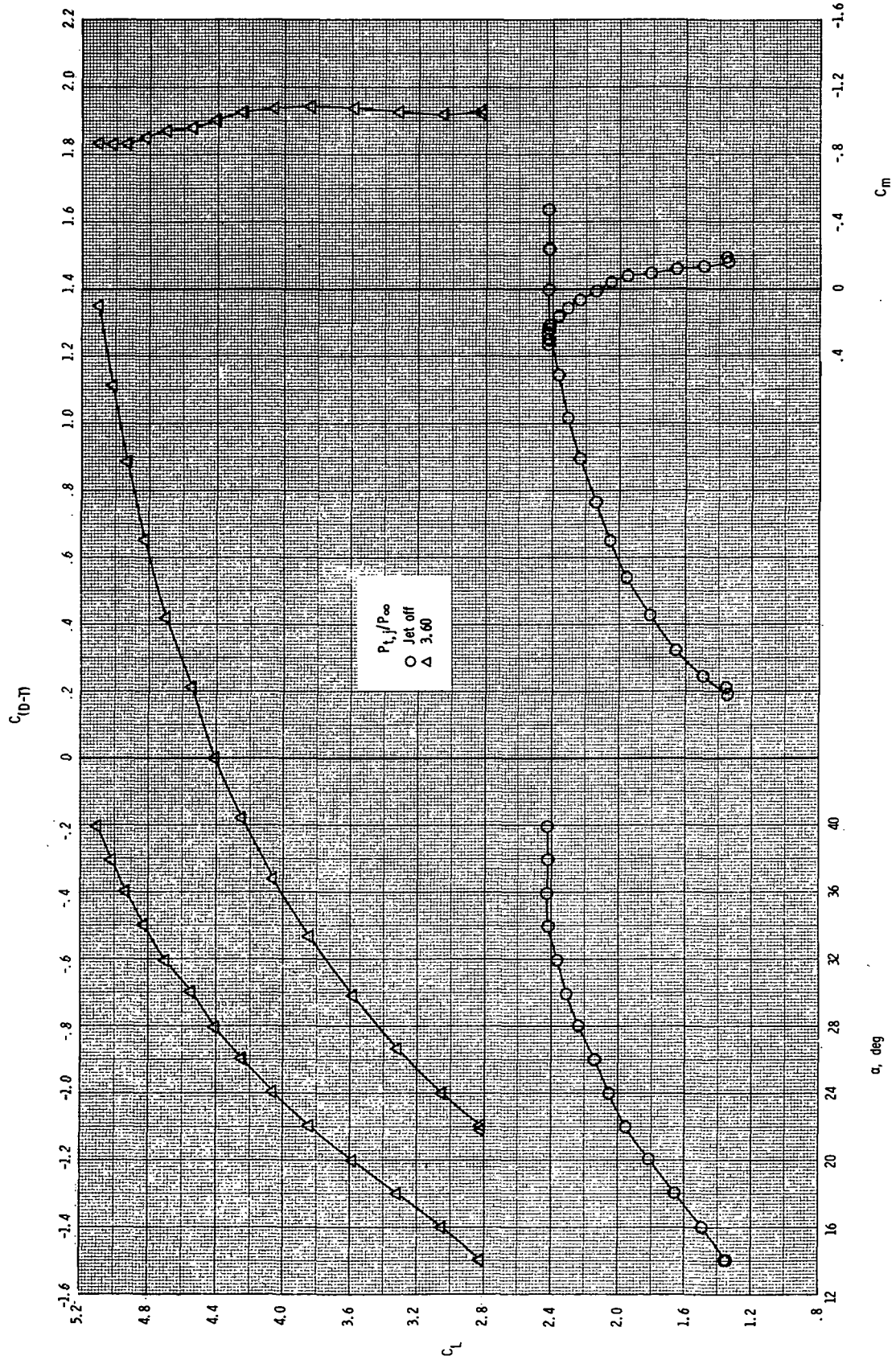
(b) $\delta_{TE} = \delta_{LE} = \delta_C = 0^\circ$, H₂ canard.

Figure 15.- Continued.



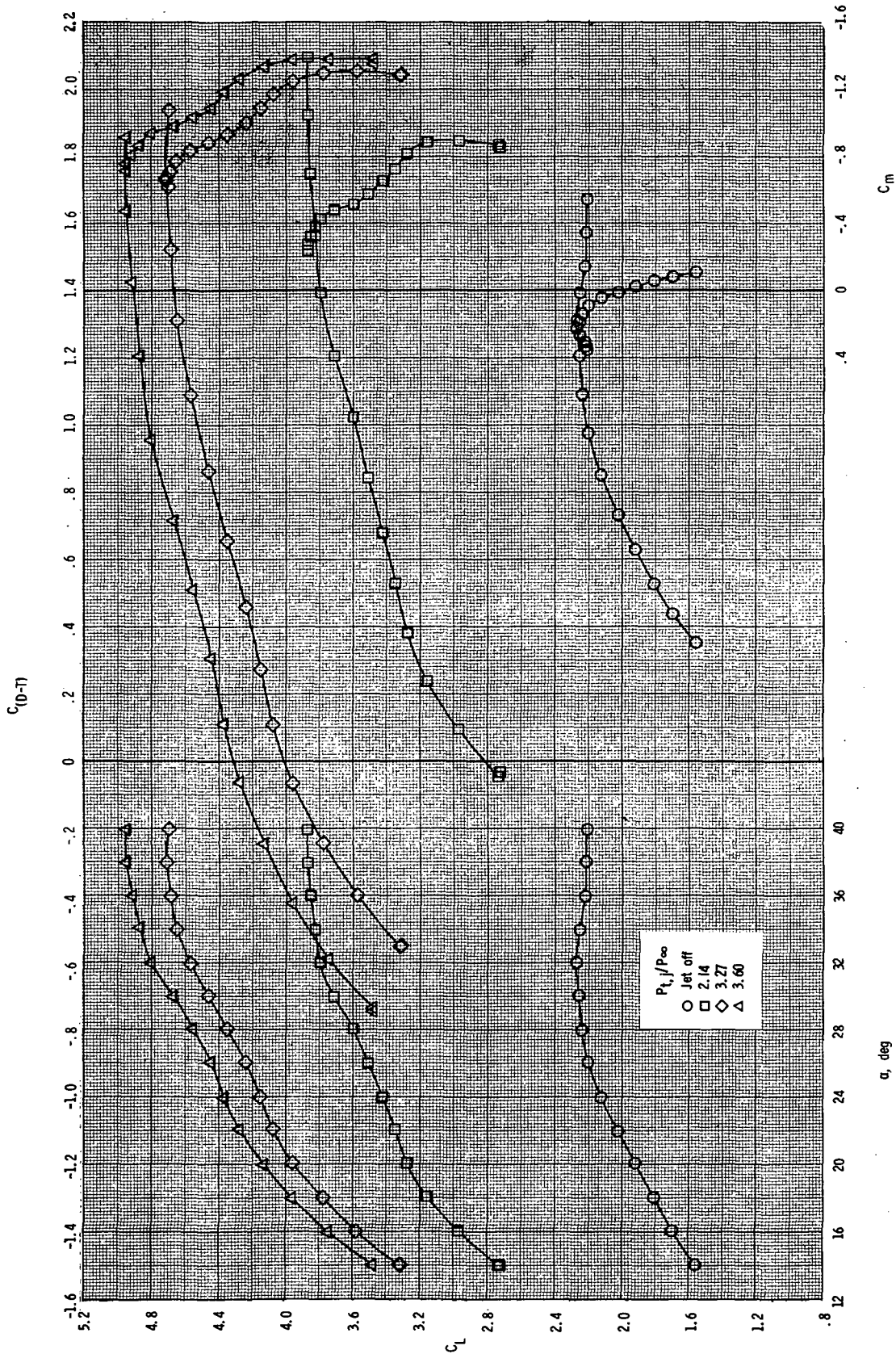
(c) $\delta_{TE} = 15^\circ$, $\delta_{LE} = 20^\circ$, $\delta_C = 0^\circ$, H_2 canard.

Figure 15 - Continued.



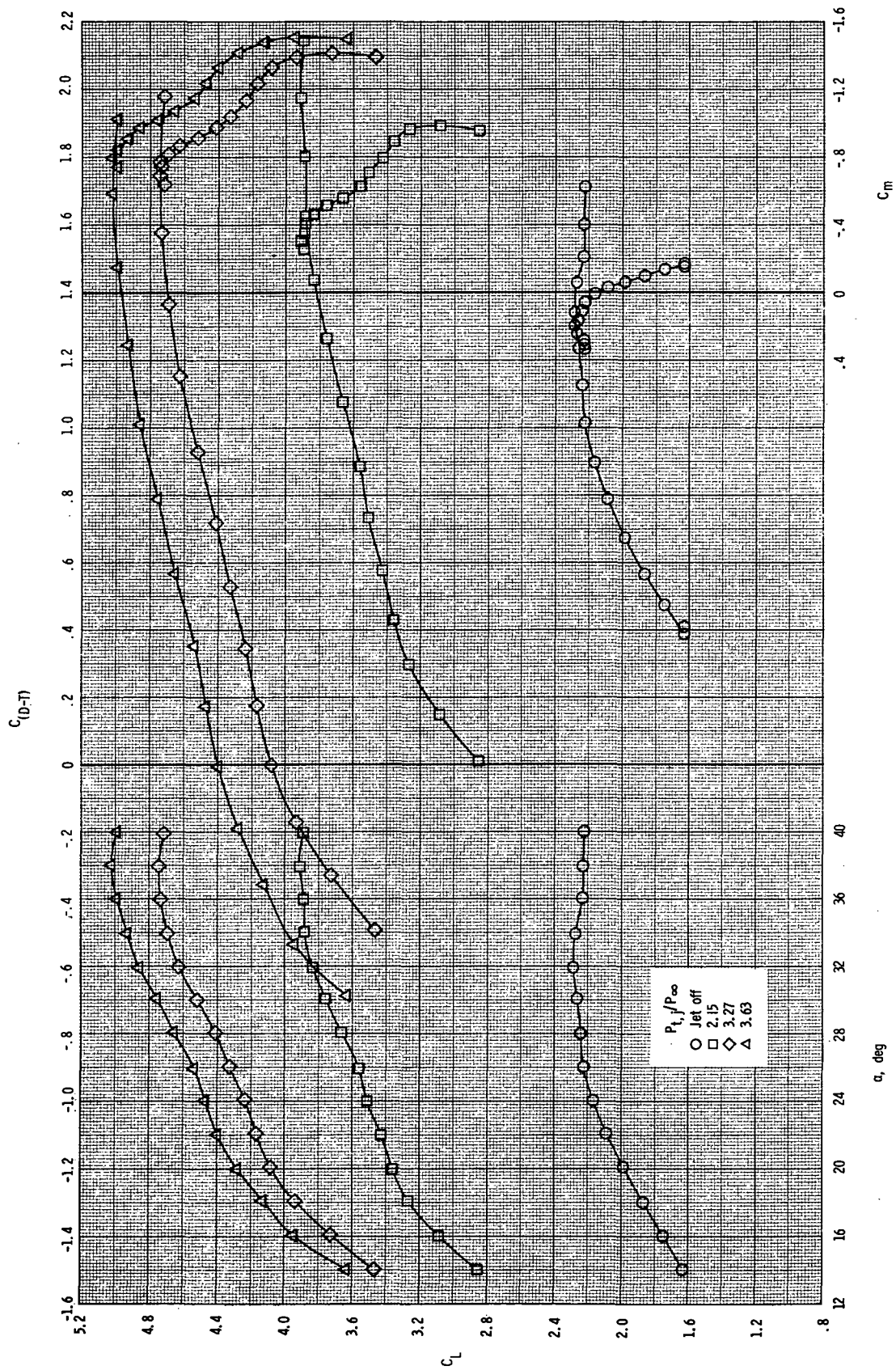
(d) $\delta_{TE} = 15^\circ$, $\delta_{LE} = 20^\circ$, $\delta_C = -10^\circ$, H_2 canard.

Figure 15.- Continued.



(e) $\delta_{TE,0} = 15^\circ$, $\delta_{TE,I} = 30^\circ$, $\delta_{LE} = \delta_C = 0^\circ$, H_2 canard.

Figure 15.- Continued.



(f) $\delta_{TE} = 30^\circ$, $\delta_{LE} = \delta_C = 0^\circ$, H_2 canard.

Figure 15.- Concluded.

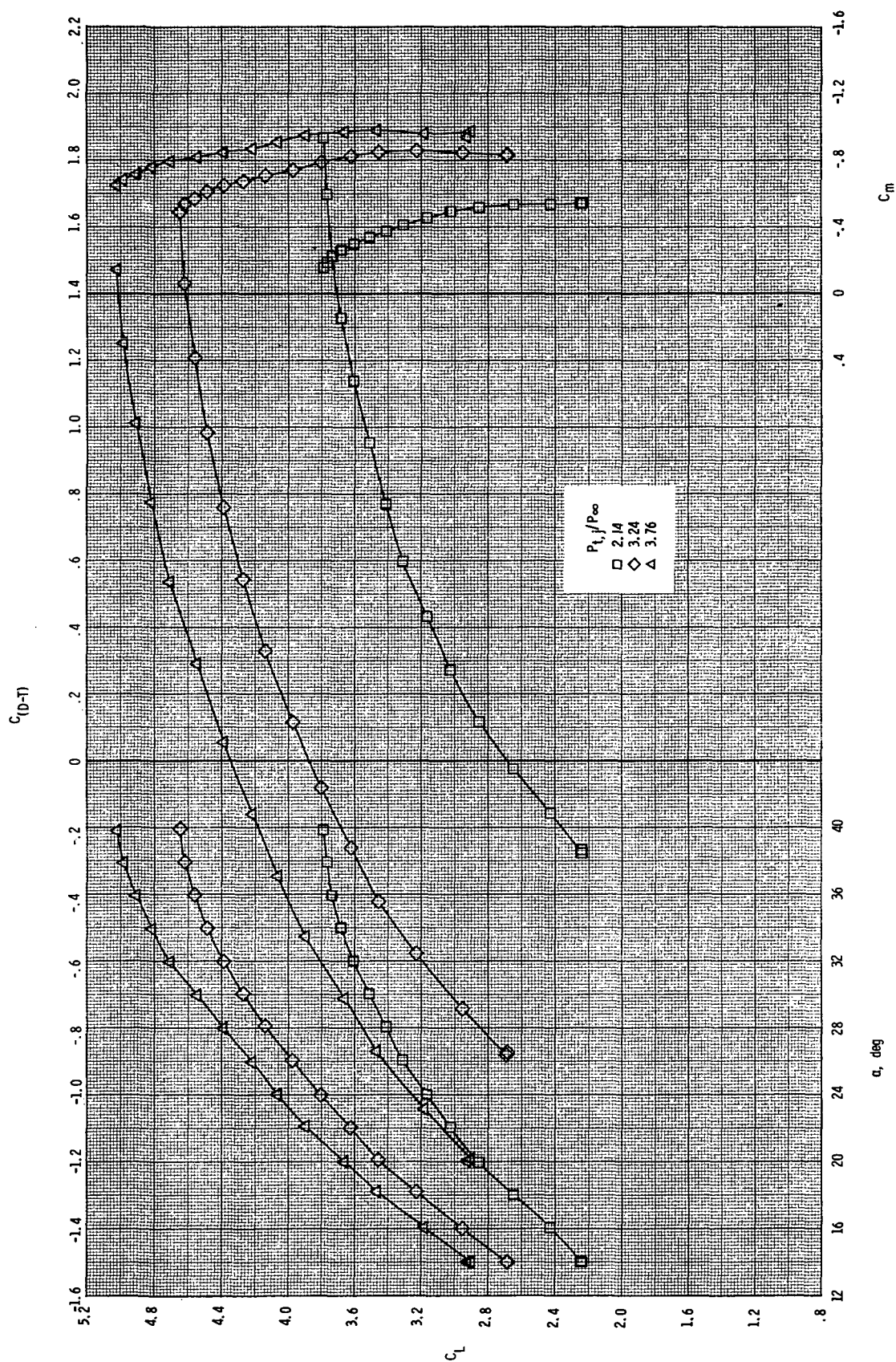


Figure 16.- Basic longitudinal aerodynamic characteristics at $M = 0.186$ for spanwise nozzle Conf 15 (3.22 cm² round, C-D, $x_n/c_r = 0.527$, $h_n/c_r = 0.0935$); $\delta_{TE} = 15^\circ$, $\delta_{LE} = \delta_C = 0^\circ$, H_2 canard.

C_{D-n}

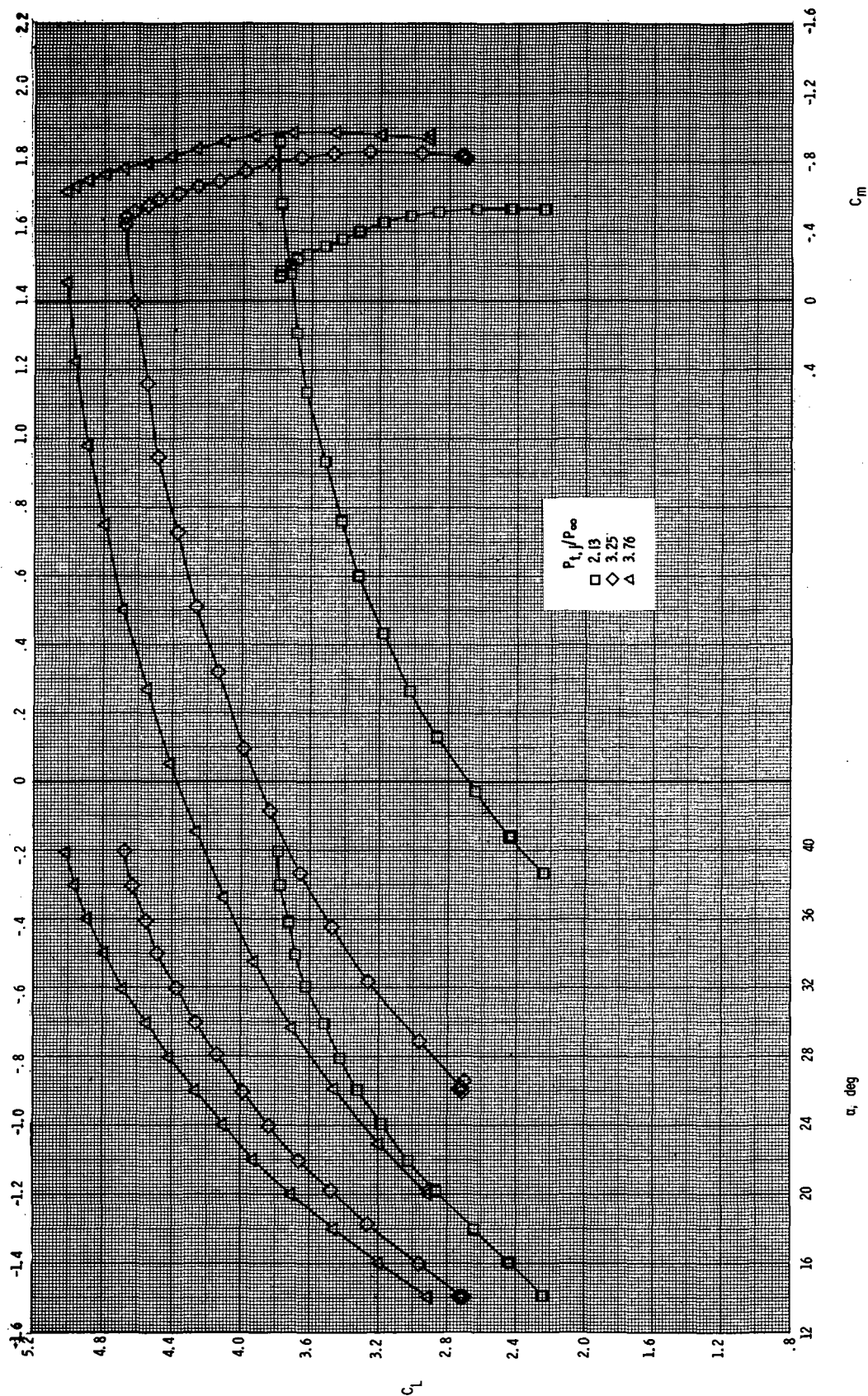


Figure 17.- Basic longitudinal aerodynamic characteristics at $M = 0.186$ for spanwise nozzle Conf 16 (3.22 cm² round, C-D, $x_n/c_r = 0.416$, $h_n/c_r = 0.0935$); $\delta_{TE} = 150^\circ$, $\delta_{LE} = 0^\circ$, H_2 canard.

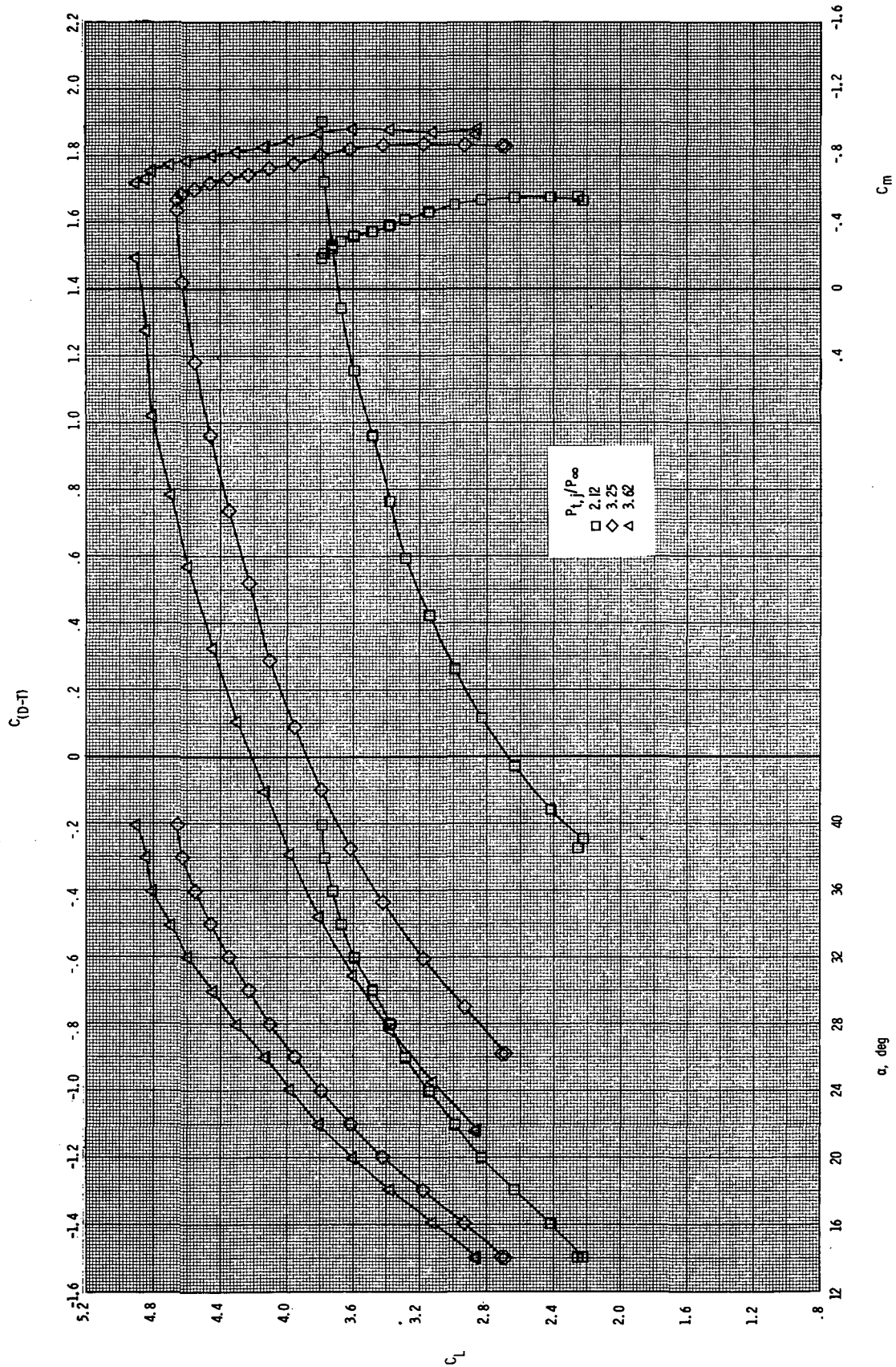


Figure 18.- Basic longitudinal aerodynamic characteristics at $M = 0.186$ for spanwise nozzle Conf 17 (3.22 cm² round, C-D, $x_n/c_r = 0.622$, $h_n/c_r = 0.0935$); $\delta_{TE} = 15^\circ$, $\delta_{LE} = \delta_C = 0^\circ$, H₂ canard.

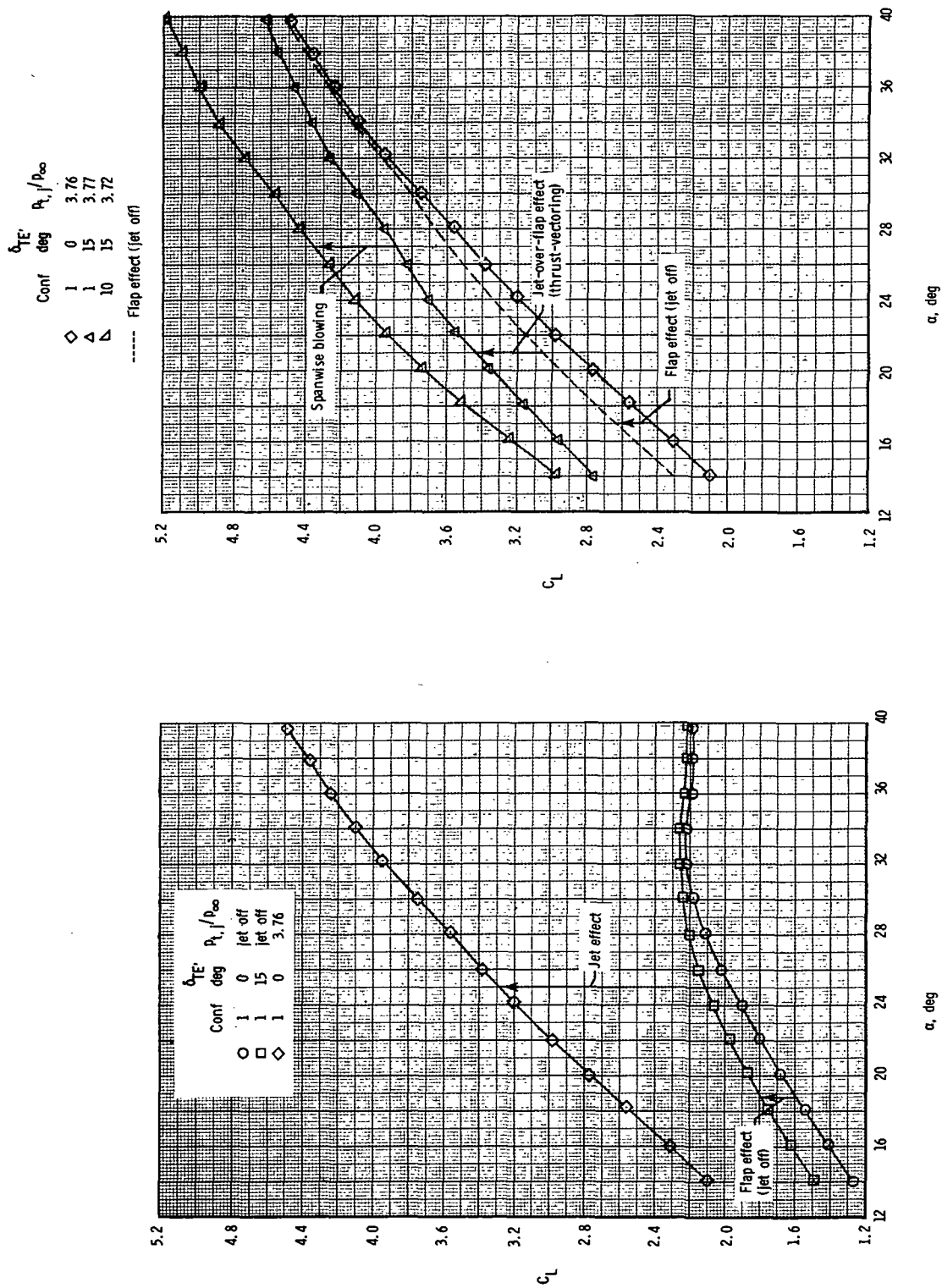
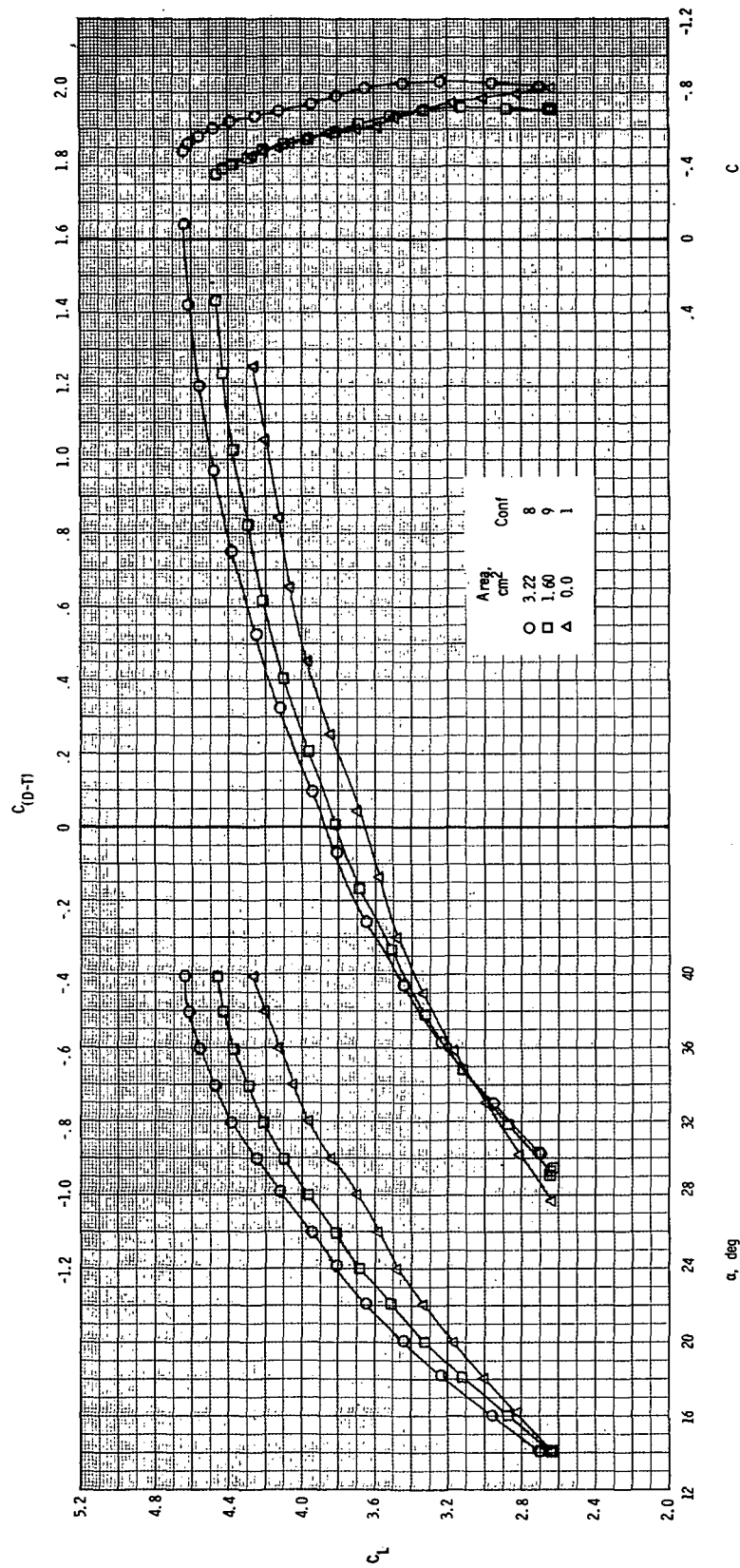
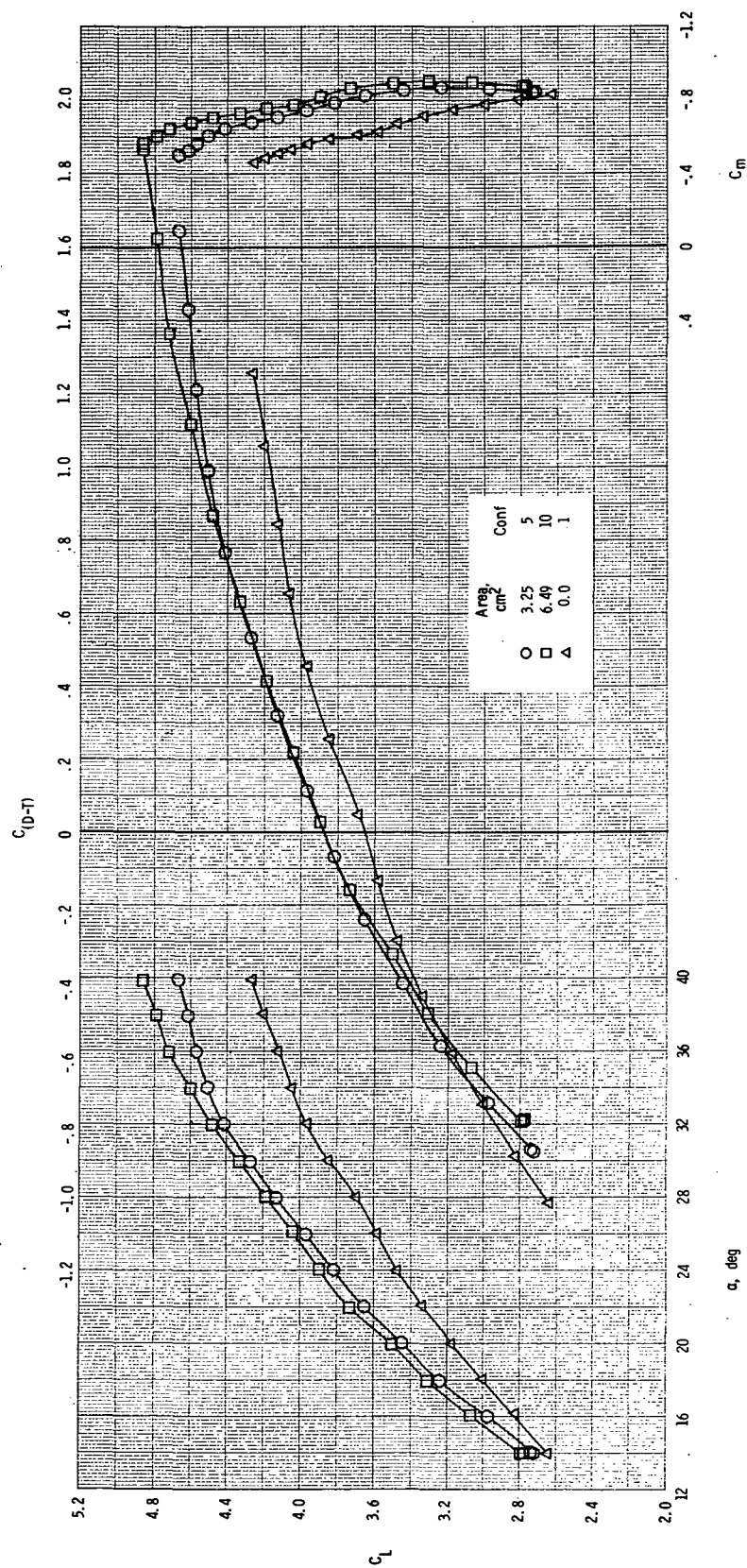


Figure 19.- Sample breakdown of effects of trailing-edge flap deflection, nozzle thrust, thrust vectoring, and spanwise blowing on lift coefficient; $\delta_{LE} = \delta_C = 0^\circ$, H_2 canard.



(a) $h_n/c_r = 0.0793$.

Figure 20.- Effect of spanwise nozzle area on longitudinal aerodynamic characteristics at $M = 0.186$; $P_{t,j}/p_\infty = 3.25$, $\delta_{TE} = 15^\circ$, $\delta_{LE} = \delta_C = 0^\circ$, H_2 canard.



(b) $h_n/c_r = 0.0935$.

Figure 20.- Concluded.

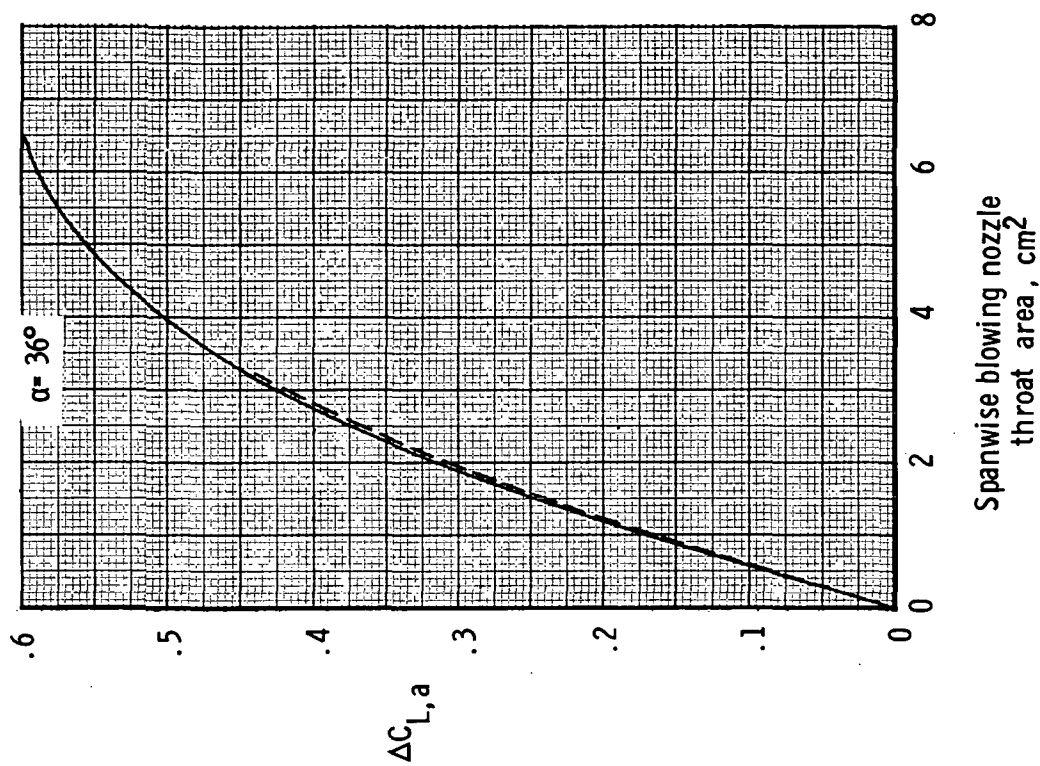
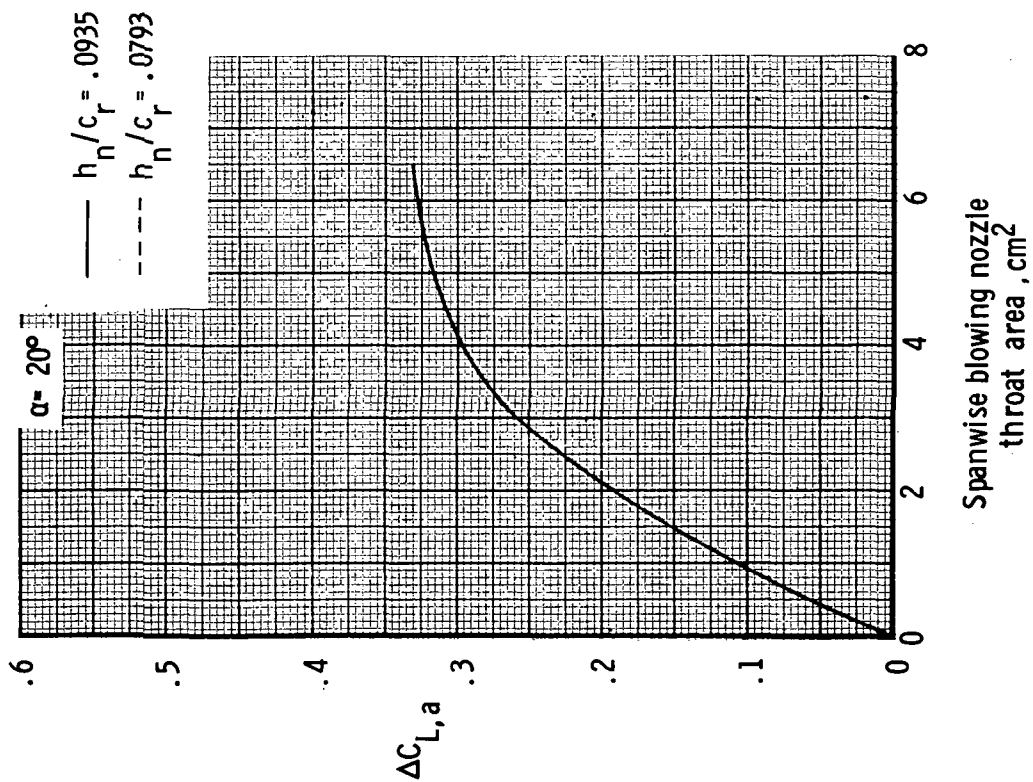
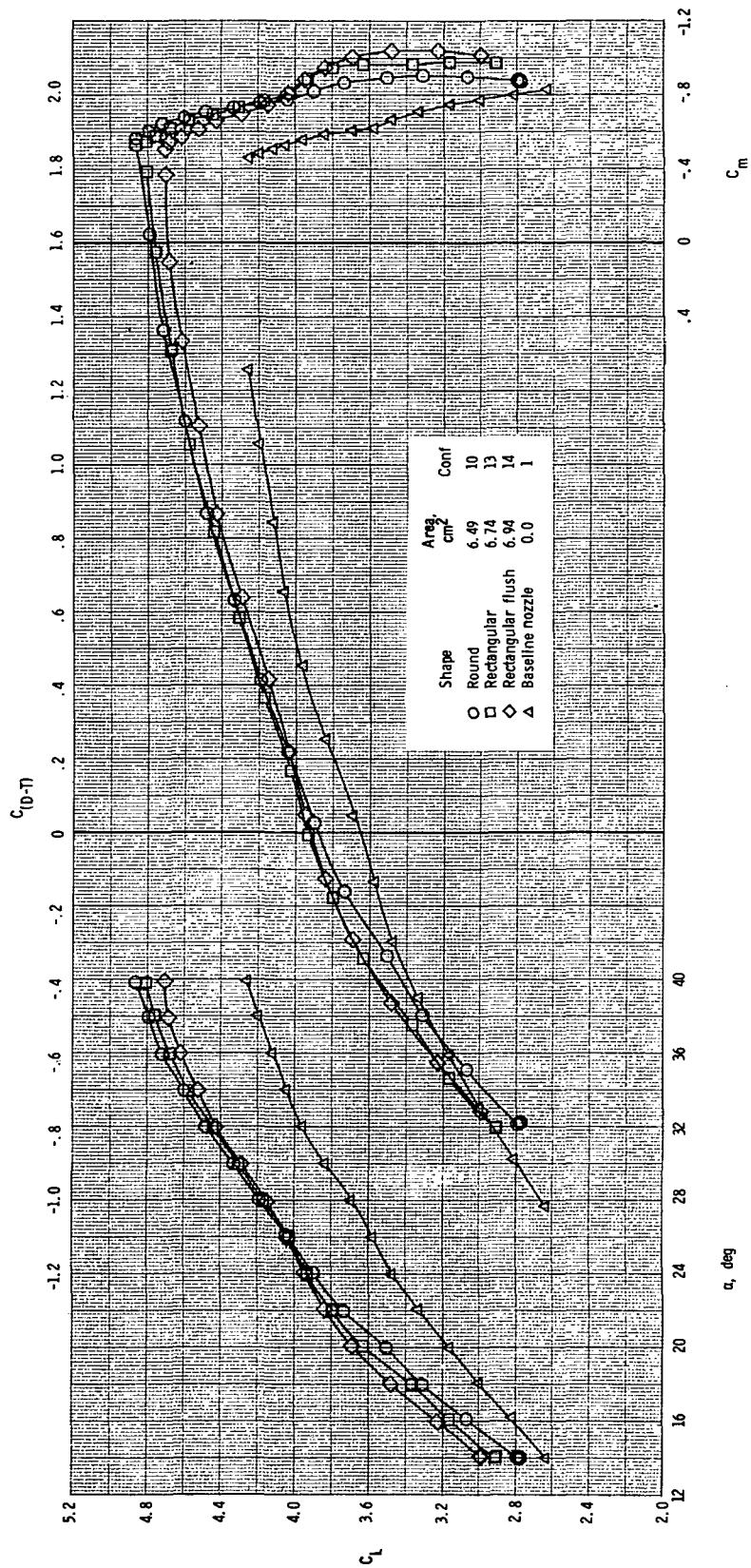
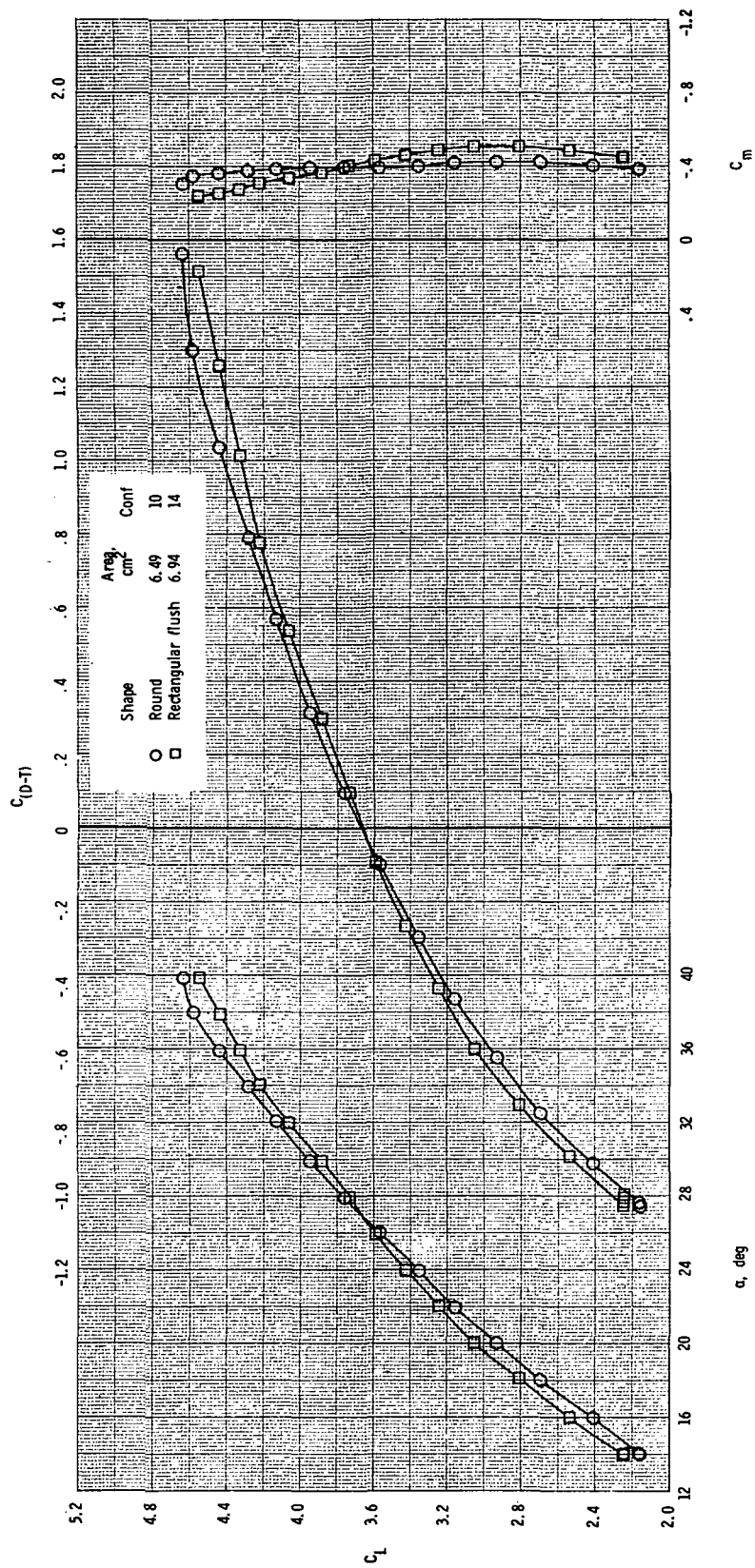


Figure 21.- Lift increment due to spanwise blowing as a function of spanwise blowing nozzle throat area; $P_{t,j}/P_\infty = 3.25$, $\delta_{TE} = 15^\circ$, $\delta_{LE} = \delta_C = 0^\circ$, H_2 canard. $\Delta C_{L,a} = C_{L,sa} - C_{L,b}$.



(a) $\delta_{TE} = 15^\circ$.

Figure 22.- Effect of spanwise nozzle external shape on longitudinal aerodynamic characteristics at $M = 0.186$; $P_{t,j}/P_\infty = 3.25$, $\delta_{LE} = \delta_C = 0^\circ$, H_2 canard.



(b) $\delta_{TE} = 0^\circ$.

Figure 22.- Concluded.

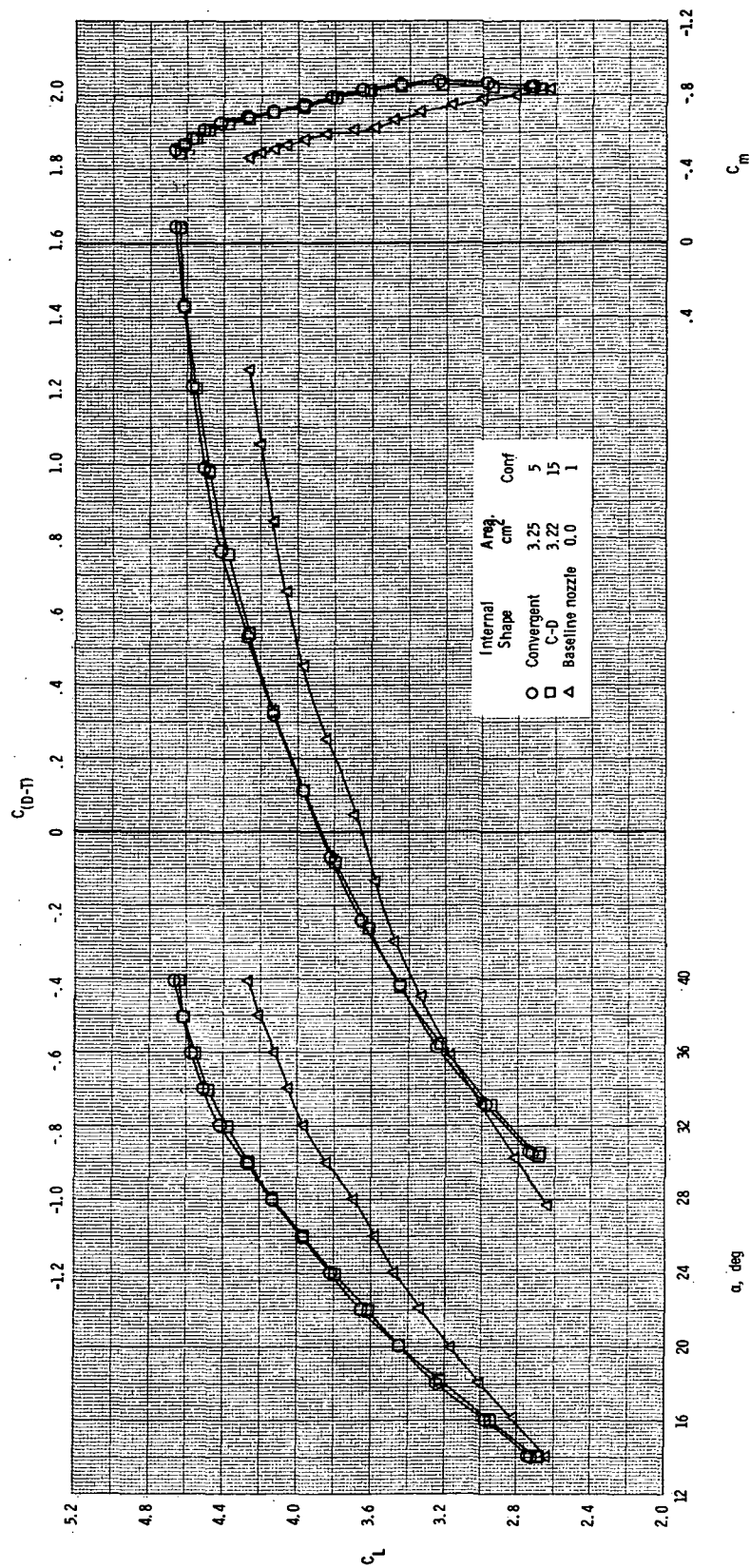
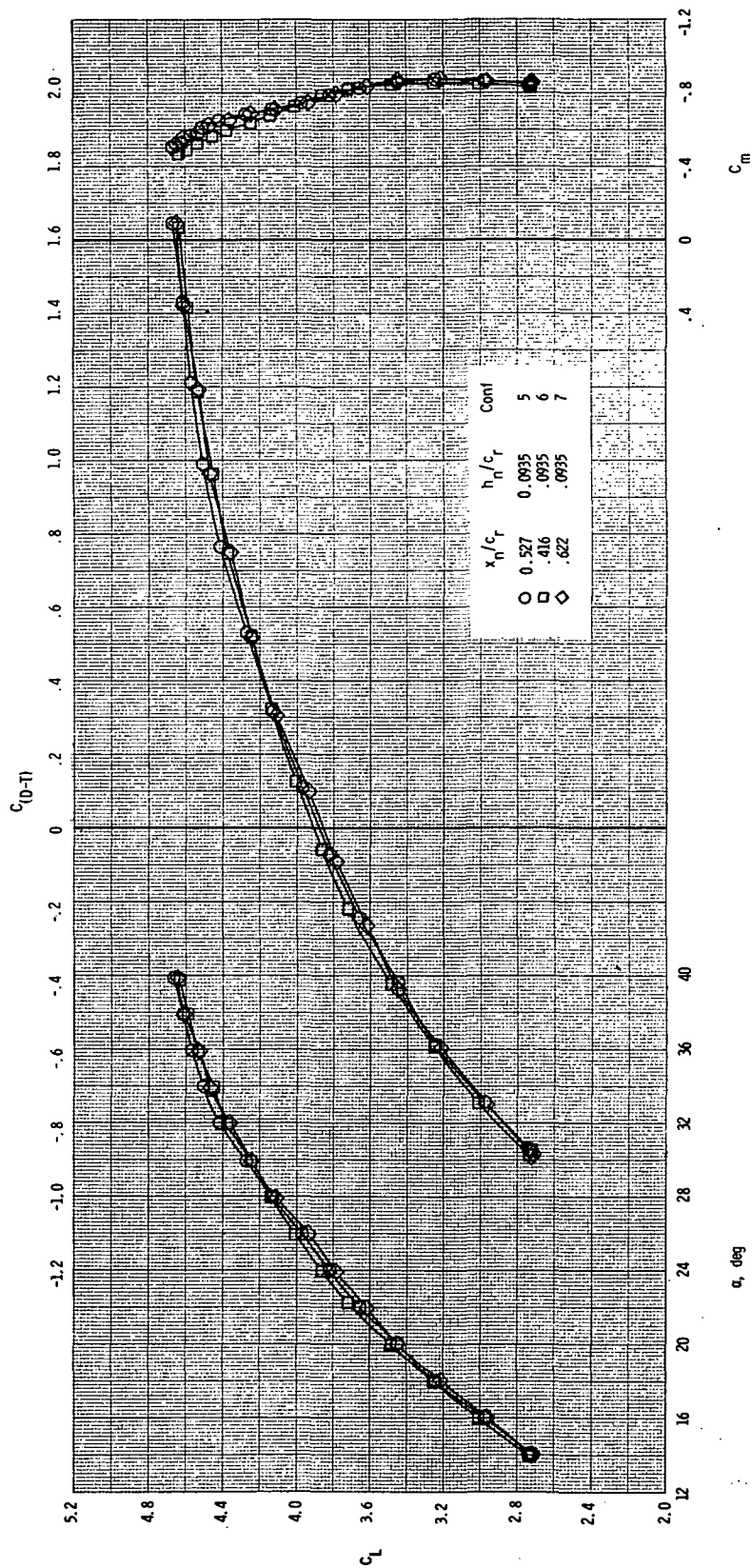
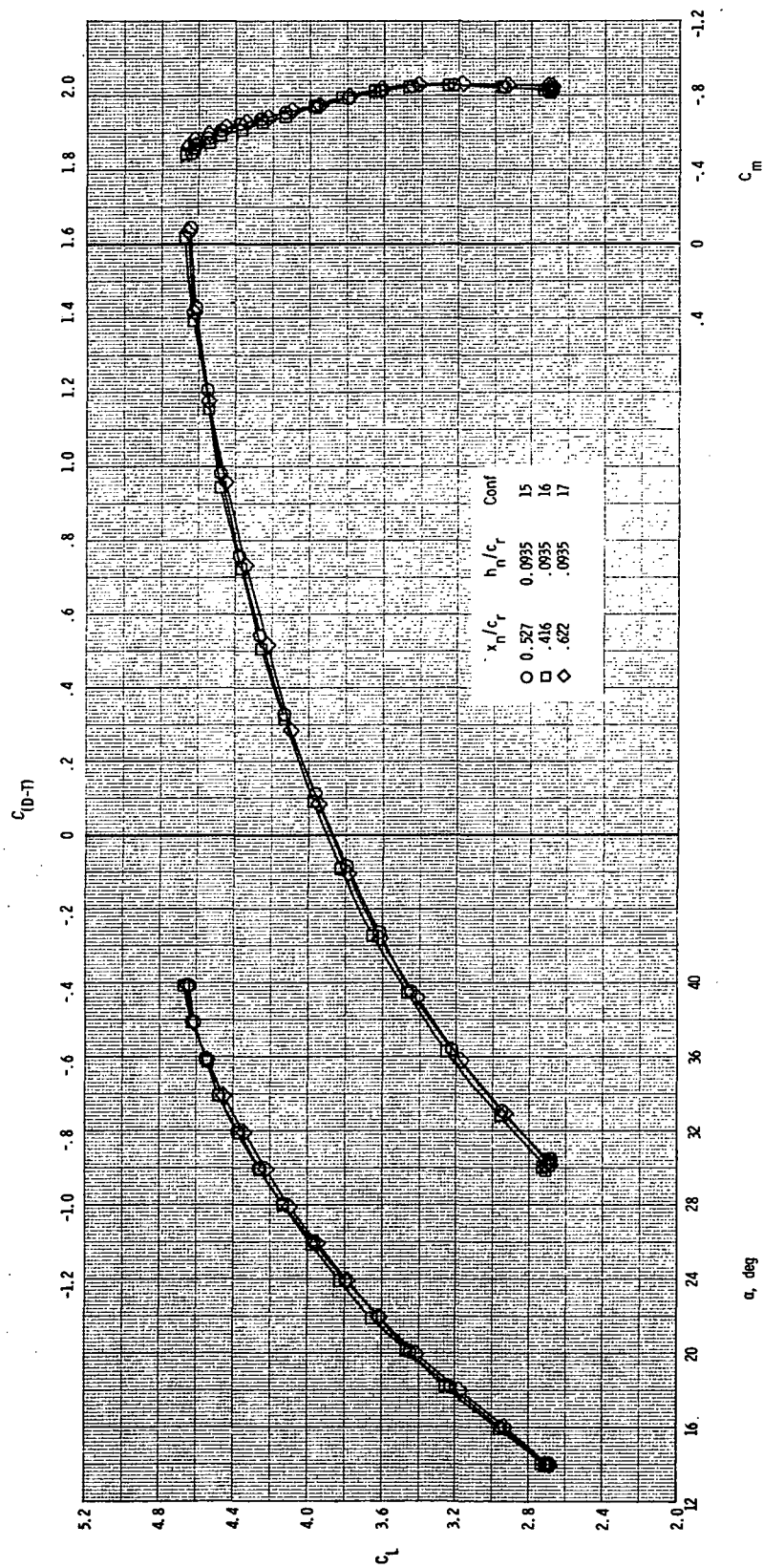


Figure 23.- Effect of spanwise nozzle internal shape on longitudinal aerodynamic characteristics at $M = 0.186$; $P_{t,j}/P_\infty = 3.25$, $\delta_{TE} = 15^\circ$, $\delta_{LE} = \delta_C = 0^\circ$, H_2 canard.



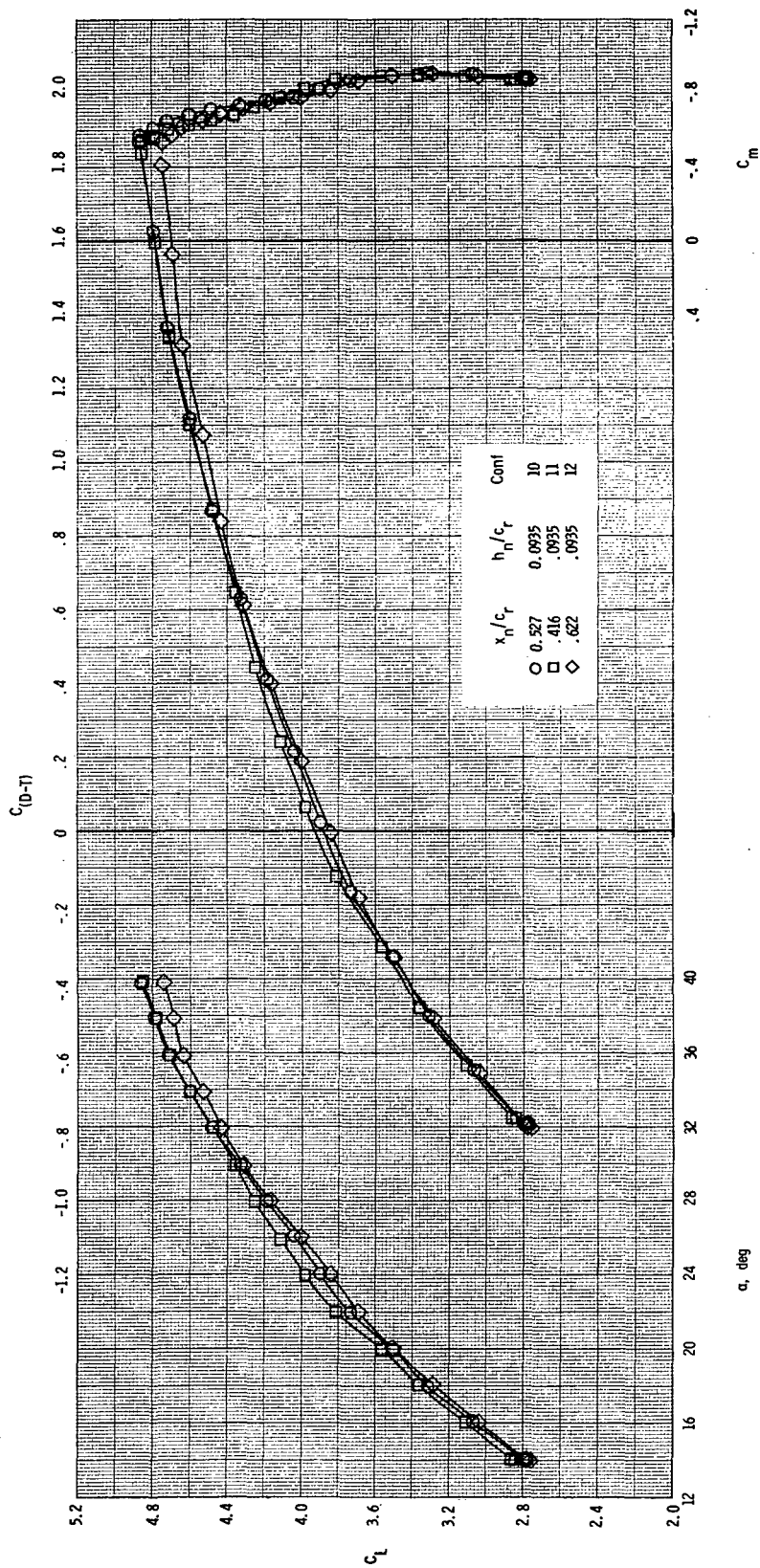
(a) 3.25 cm² round, convergent.

Figure 24.- Effect of spanwise nozzle axial location on longitudinal aerodynamic characteristics at $M = 0.186$, $p_{t,j}/p_{\infty} = 3.25$, $\delta_{TE} = 15^\circ$, $\delta_{LE} = \delta_C = 0^\circ$. H_2 canard.



(b) 3.22 cm² round, C-D.

Figure 24.- Continued.



(c) 6.49 cm² round, convergent.

Figure 24.- Concluded.

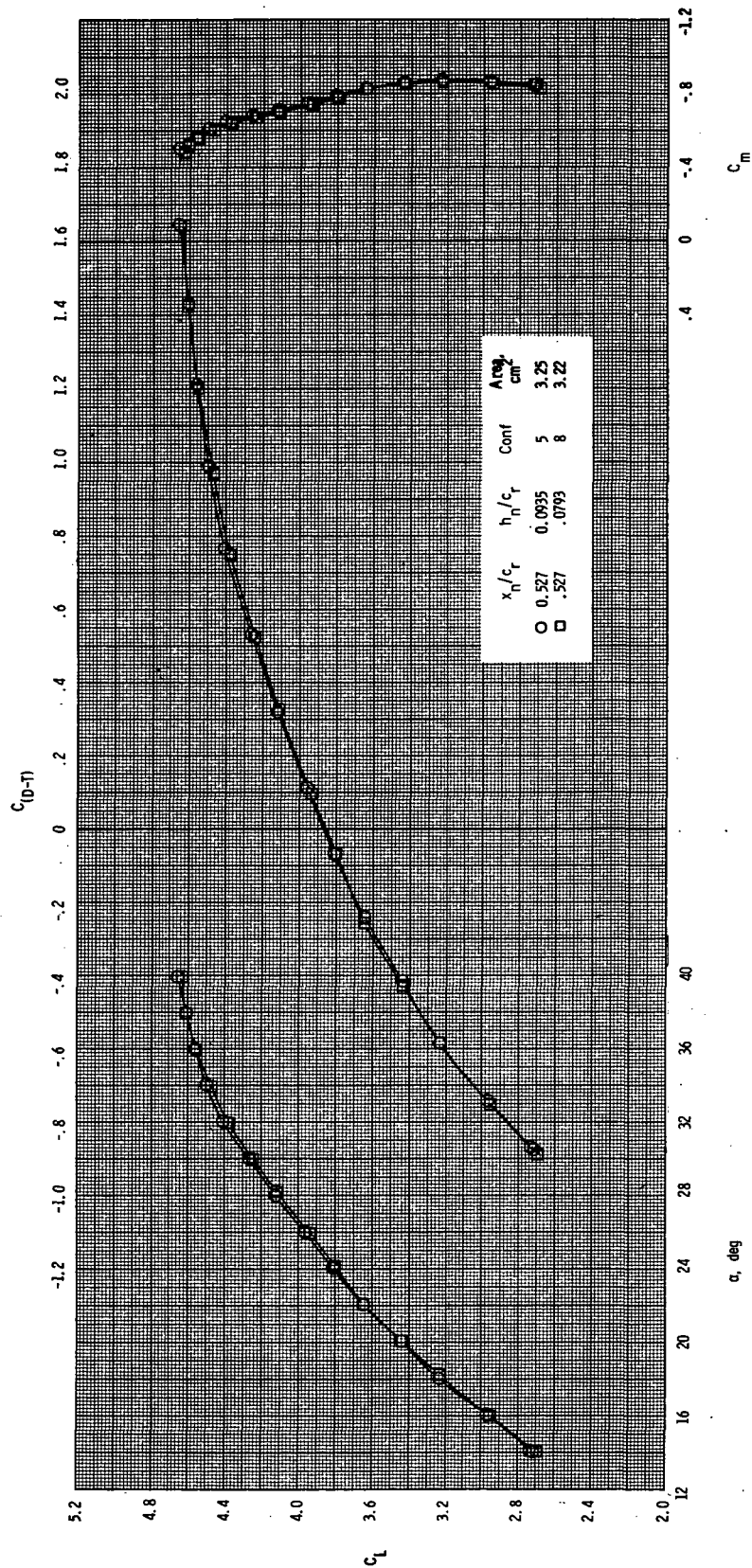


Figure 25.- Effect of spanwise nozzle vertical location on longitudinal aerodynamic characteristics at $M = 0.186$; $pt_t/j/p_\infty = 3.25$, round, convergent, $\delta_{TE} = 15^\circ$, $\delta_{LE} = \delta_C = 0^\circ$, H_2 canard.

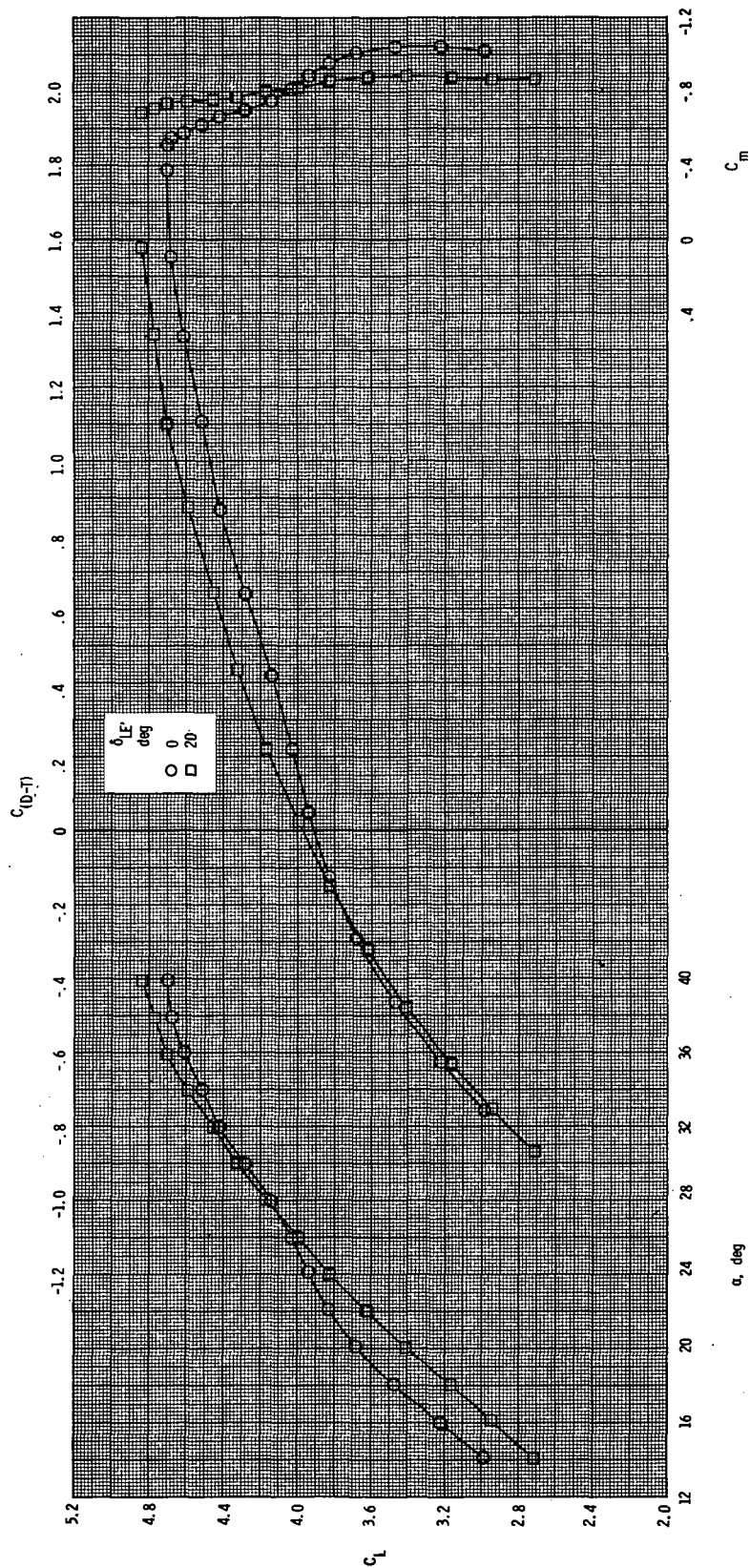


Figure 26.- Effect of leading-edge flap deflection on longitudinal aerodynamic characteristics at $M = 0.186$ in the presence of spanwise-blowing nozzle, Conf 14 (6.94 cm² rectangular flush, convergent, $x_n/c_r = 0.493$, $h_n/c_r = 0.068$); $p_{t,j}/p_\infty = 3.25$, $\delta_{TE} = 15^\circ$, $\delta_C = 0^\circ$, H_2 canard.

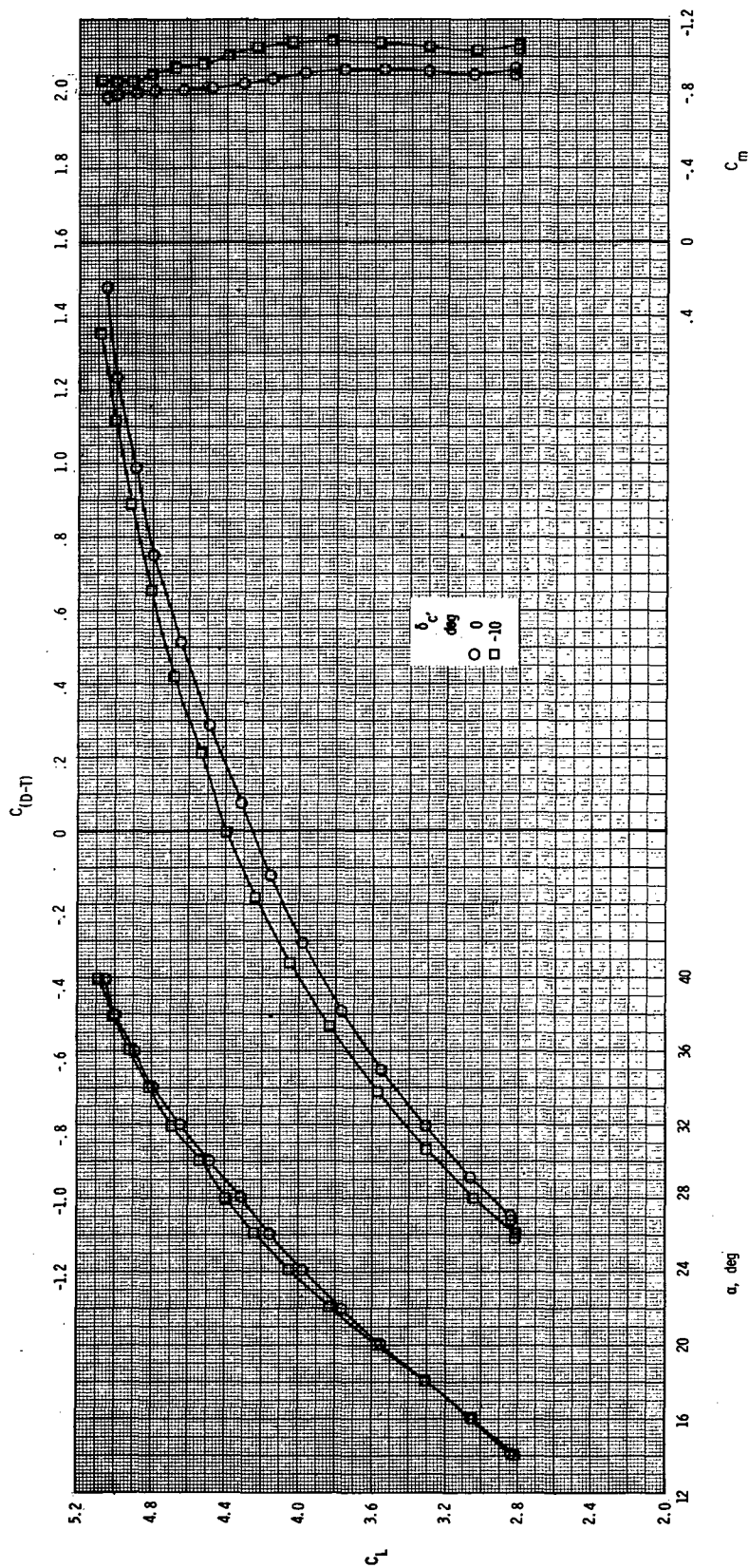
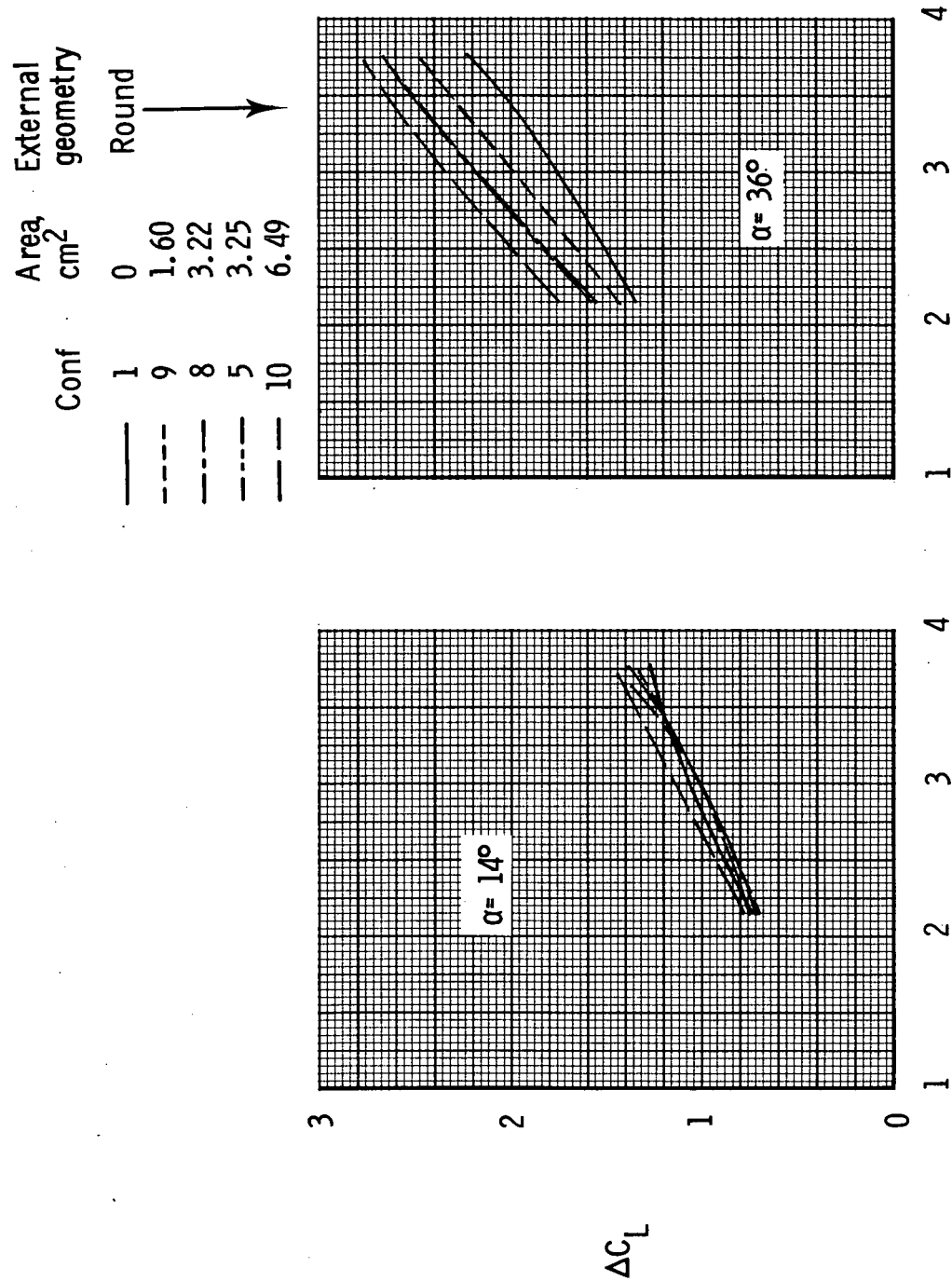


Figure 27.- Effect of canard incidence on longitudinal aerodynamic characteristics at $M = 0.186$ in the presence of spanwise-blowing nozzle, Conf 14 (6.94 cm² rectangular flush, convergent, $x_n/c_r = 0.493$, $h_n/c_r = 0.068$); $P_{t,j}/P_\infty = 3.62$, $\delta_{TE} = 15^\circ$, $\delta_{LE} = 20^\circ$, H₂ canard.



$$P_{t,j} / P_\infty$$

Figure 28.- Effect of spanwise nozzle throat area on incremental lift at $M = 0.186$; $\delta_{TE} = 15^\circ$, $\delta_{LE} = \delta_C = 0^\circ$, H_2 canard.

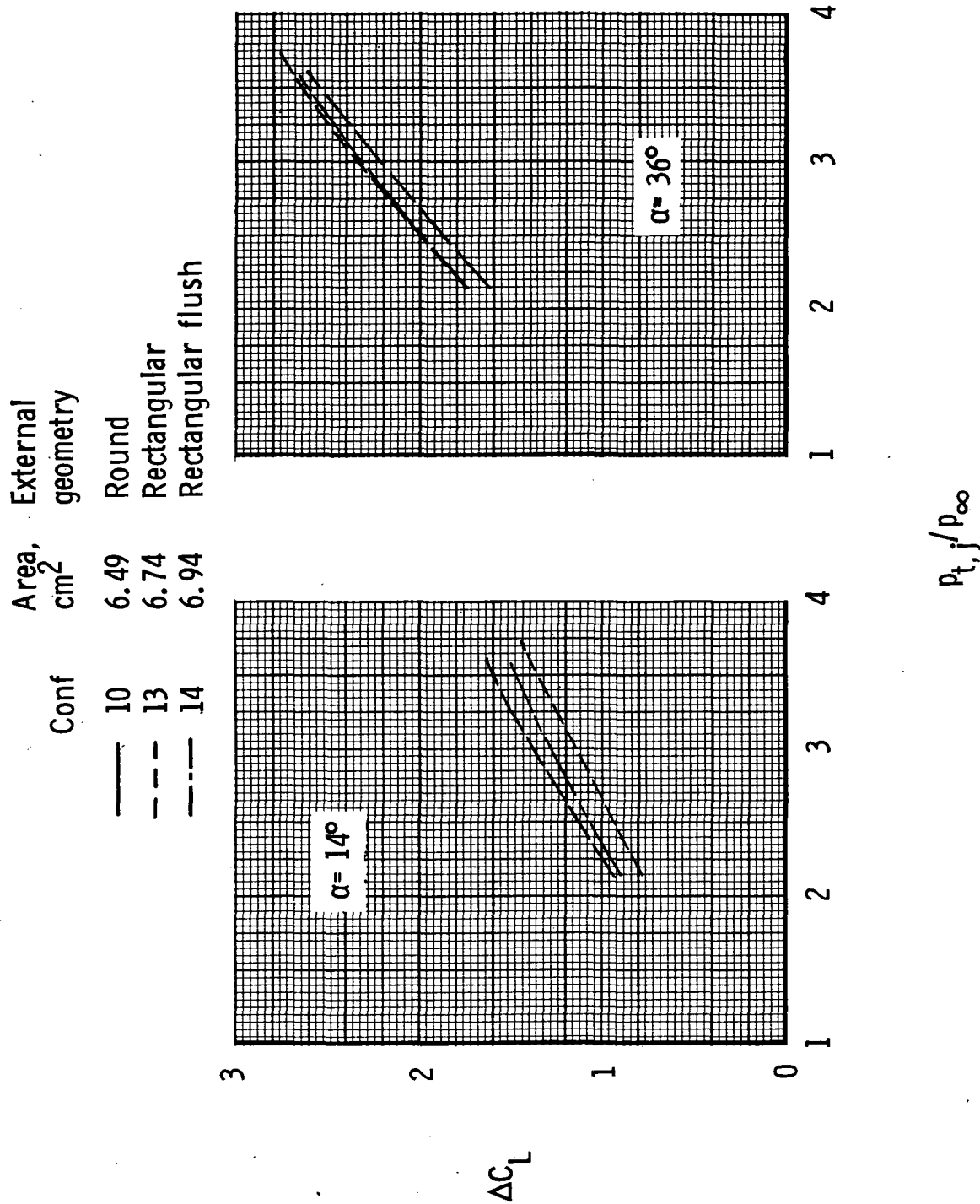


Figure 29.- Effect of spanwise nozzle geometry on incremental lift at $M = 0.186$; $\delta_{TE} = 15^\circ$, $\delta_{LE} = \delta_C = 0^\circ$, H_2 canard.

External
geometry

Round



h_n/c_r

0.0935

.0935

.0935

x_n/c_r

0.527

.416

.622

Conf

10

11

12

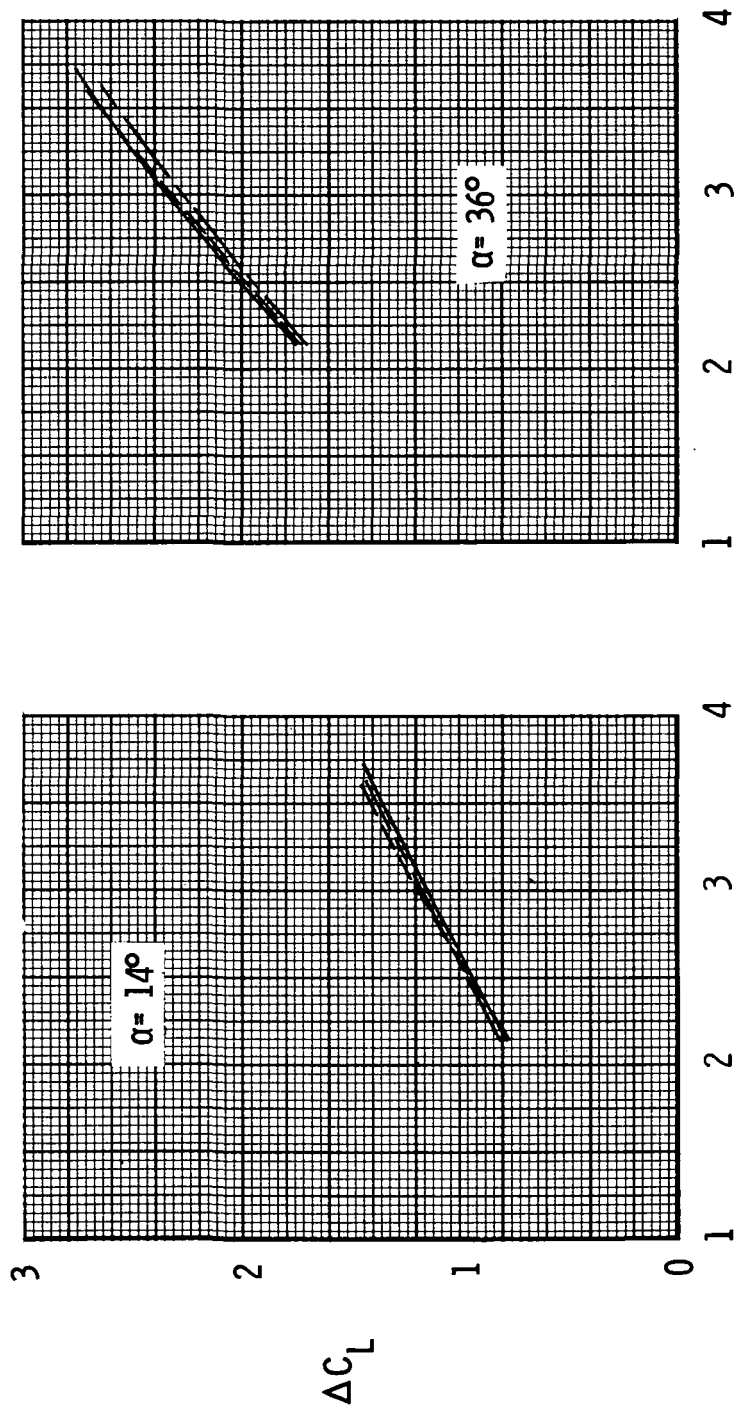


Figure 30.- Effect of spanwise nozzle axial location on incremental lift
at $M = 0.186$; $\delta_{TE} = 150^\circ$, $\delta_{LE} = \delta_C = 0^\circ$, H_2 canard.

1. Report No. NASA TP-1215		2. Government Accession No.		3. Recipient's Catalog No.	
4. Title and Subtitle EFFECTS OF SPANWISE NOZZLE GEOMETRY AND LOCATION ON THE LONGITUDINAL AERODYNAMIC CHARACTERISTICS OF A VECTORED-ENGINE-OVER-WING CONFIGURATION AT SUBSONIC SPEEDS				5. Report Date June 1978	
				6. Performing Organization Code	
7. Author(s) Laurence D. Leavitt and Long P. Yip				8. Performing Organization Report No. L-12015	
9. Performing Organization Name and Address NASA Langley Research Center Hampton, VA 23665				10. Work Unit No. 505-11-13-04	
				11. Contract or Grant No.	
12. Sponsoring Agency Name and Address National Aeronautics and Space Administration Washington, DC 20546				13. Type of Report and Period Covered Technical Paper	
				14. Sponsoring Agency Code	
15. Supplementary Notes					
16. Abstract <p>An investigation has been conducted in the Langley V/STOL tunnel to determine the effects of spanwise blowing on the longitudinal aerodynamic characteristics of a model using a vectored-engine-over-wing powered lift concept. The effects of spanwise nozzle throat area, internal and external nozzle geometry, and vertical and axial location were investigated. These effects were studied at a Mach number of 0.186 over an angle-of-attack range from 14° to 40°. A high-pressure air system was used to provide jet-exhaust simulation. Engine nozzle pressure ratio was varied from 1.0 (jet off) to approximately 3.75.</p>					
17. Key Words (Suggested by Author(s)) Spanwise blowing Subsonic speeds Longitudinal aerodynamic characteristics Vectored thrust			18. Distribution Statement Unclassified - Unlimited Subject Category 02		
19. Security Classif. (of this report) Unclassified	20. Security Classif. (of this page) Unclassified	21. No. of Pages 75	22. Price* \$5.25		

National Aeronautics and
Space Administration

Washington, D.C.
20546

Official Business

Penalty for Private Use, \$300

THIRD-CLASS BULK RATE

Postage and Fees Paid
National Aeronautics and
Space Administration
NASA-451



NASA

POSTMASTER: If Undeliverable (Section 158
Postal Manual) Do Not Return
